Theoretical Investigation of Subwavelength Gratings and Vertical Cavity Lasers Employing Grating Structures

Taghizadeh, Alireza

Publication date:
2016

Document Version
Publisher's PDF, also known as Version of record

Theoretical Investigation of Subwavelength Gratings and Vertical Cavity Lasers Employing Grating Structures

Alireza Taghizadeh

Ph.D. Thesis

A dissertation submitted in partial fulfillment of the requirements for the degree of *Doctor of Philosophy*

Department of Photonics Engineering (DTU Fotonik)

Technical University of Denmark

January 2016

Project period:	• February 2013 - January 2016
Main supervisor:	• Assoc. Prof. Il-Sug Chung
Co-supervisor:	• Prof. Jesper Mørk
Ph.D. defense committee:	• Assoc. Prof. Andrei Lavrinenko, Technical University of Denmark, Denmark • Prof. Geert Morthier, Ghent University, Belgium • Prof. Mattias Hammar, Royal Institute of Technology (KTH), Sweden

Abstract

This thesis deals with theoretical investigations of a newly proposed grating structure, referred to as hybrid grating (HG) as well as vertical cavity lasers based on the grating reflectors. The HG consists of a near-subwavelength grating layer and an unpatterned high-refractive-index cap layer. Though both sides of the grating layer are not surrounded by low refractive-index materials as in high-index-contrast gratings (HCGs), the HG can provide a near-unity reflectivity over a broader wavelength range than HCGs, or work as a resonator with a quality (Q) factor as high as 109. The physics behind these reflector and resonator properties are studied thoroughly. A HG structure comprising a III-V cap layer with a gain material and a Si grating layer enables the realization of a compact vertical cavity laser integrated on Si platform, which has a superior thermal property and fabrication feasibility than the HCG-based ones. Furthermore, the concept of cavity dispersion in vertical cavities is introduced and its importance in the modal properties is numerically investigated. The dispersion curvature of a cavity mode is interpreted as the effective photon mass of the cavity mode. In a vertical cavity based on a HCG or HG reflector, this effective photon mass can be engineered by changing the grating parameters, which is not the case in a vertical cavity based on distributed Bragg reflectors (DBRs). This engineering capability enables us to form various photonic heterostructures in lateral directions, which is analogous to electronic quantum wells in conduction or valence bands. Several interesting configurations of heterostructures have been investigated and their potential in fundamental physics study and applications are discussed.

For numerical and theoretical studies, a three-dimensional (3D) optical simulator has been implemented, based on the Fourier modal method (FMM). A method to simplify 3D simulations to lower dimensional simulations is suggested, which enables us to perform fast simulations before doing a thorough 3D simulation. Moreover, three different techniques for determining the resonance frequency and Q-factor of a cavity mode are compared. Based on that, the quasi-normal mode approach with real frequency has been chosen due to its numerical efficiency. In this comparison, the associated computational uncertainty for the resonance frequency and Q-factor is investigated, which shows that the uncertainty in the Q-factor can be several orders of magnitude larger than the uncertainty in the resonance frequency.

Next, the HG is shown to possess a near-unity reflectivity in a broad wavelength range, which can be broader than the HCG, since the cap layer introduces more

guided mode resonances (GMRs) in the reflectivity spectrum. The fabrication tolerance of the HG is investigated numerically, which shows that the broadband near-unity reflectivity characteristic is prone to common fabrication errors. An experimental demonstration of the HG reflector confirms its broadband reflection characteristics. Furthermore, the physics study of HG as high Q-factor resonator illustrates that the resonance mechanism is similar to the resonances appearing in HCG resonators, and it is quite different from the conventional GMR filters. The effect of fabrication errors and finite size of the structure is investigated to understand the feasibility of fabricating the proposed resonator.

Finally, the significance of the cavity dispersion in vertical cavity structure is illustrated. An analytic expression is derived for the dispersion, which shows that the cavity dispersion has contributions from both top and bottom mirrors through their reflectivity phase response as well as the nominal cavity through its thickness. For conventional DBRs, the mirror contribution in dispersion curvature is always positive and negligible, compared to the nominal cavity contribution. However, the HCG or HG contributions can be a specific positive or negative value in different transverse directions, significantly modifying the entire dispersion curvature. The influences of the photon effective mass on the mode confinement, mode spacing and transverse modes are investigated. Particularly, it is shown that the anisotropic dispersion curvature in in-plane heterostructure is responsible for the phenomenon of mode grouping, which is also confirmed by experimental results. Furthermore, in Si-integrated photonics, a laser source that can output light into a Si waveguide is essential, and it is shown that in HGG-based vertical cavity laser the light can be coupled to an in-plane output waveguide. The design rules for achieving a high out-coupling efficiency into the in-plane waveguide are discussed and the in-plane out-coupling efficiency as high as 68% is achieved in design. Based on this platform, a system of two laterally coupled cavities is proposed and investigated, which exhibits the breaking of parity-time (PT) symmetry in vertical cavity structures. Compared to other types of platform for studying this phenomenon such as ring/disk resonators and photonic crystal cavities, the HCG/HG-based vertical cavities appear to be more feasible for realizing an electrically pumped device, which may pave the way for finding device applications for PT-symmetry breaking phenomenon.

Preface

This thesis is submitted to the DTU Fotonik, the Department of Photonics Engineering at Technical University of Denmark (DTU) for the partial fulfillment of the degree of Doctor of Philosophy (Ph.D.). The work presented here is part of the Ph.D. project, which was carried out in the Nanophotonics Theory and Signal Processing group for three years from February 1^{st}, 2013 to January 31^{st} 2016. The project has been supervised by main supervisor, Assoc. Prof. Il-Sug Chung, and co-supervisor, Prof. Jesper Mørk both from DTU Fotonik. From August to October 2015, a research stay for three month at Department of Electrical Engineering and Computer Sciences, University of California, Berkeley, USA, in the group of Prof. Ming C. Wu, was undertaken, mainly on the simulation and modeling of the dynamic response of optical antenna-enhanced light-emitting diodes, which is not covered in this thesis.

The Ph.D. project was mainly financed by Danish Council for Independent Research (Grant No. 0602-01885B). It also has partly been supported by Villum Fonden via the NAnophotonics for TErabit Communications (NATEC) Centre of Excellence, as well as the Innovation Fund Denmark through the HOT project (Grant No. 5106-00013B).

Acknowledgements

Foremost, I should thank my main supervisor Prof. Il-Sug Chung, who gave me the chance and opportunity to work on this project and support me during the Ph.D. study. His availability and guidance with many fruitful discussions helped me to achieve my goals during this project. I express my gratitude towards my co-supervisor and also group leader, Prof. Jesper Mørk, who always deepened my physical understanding with his broad physical knowledge and intelligent comments. Furthermore, he was a constant source of motivation and encouragement for me during these years.

I thank all DTU Fotonik staffs, in particular, members of the Theory and Signal Processing group as well as Nanophotonics research section, for creating a fabulous working environment and an inspiring scientific atmosphere. A special thank goes to Gyeong Cheol Park, who shares his fabrication and characterization knowledge with me, and provide me the experimental results presented in this dissertation. Also, I should thank my colleague, Andreas Dyhl Østerkryger, for Danish translation of the abstract.

My sincere thanks also goes to Prof. Ming C. Wu from University of California, Berkeley, for giving me the research stay opportunity in his group and leading me to work on a diverse project. I should also thank the entire Prof. Wu group for welcoming me during my stay with them.

I wish to acknowledge Danish Council for Independent Research, Villum Fonden, and Innovation Fund Denmark for financing the Ph.D. project, and Otto Mønsteds Fond, Oticon Fonden, and Augustinusfonden for economical support towards conference participation, and my research stay.

I should thank my daily lunch team at DTU, my Persian friends, who I had fun with and got the energy for the rest of the day. I enjoyed my occasional coffee break with my office-mates and particularly my friend Mohammad, with whom I had many interesting and funny discussions about news, football, science, and even politics.

Last but not least, I would like to thank my whole family; my lovely mother, father, and two sisters, who all support me throughout my life.

At the end, I would like to express full appreciation to my beloved fabulous wife, Sara, without her encouragement, I would not have finished this thesis. She has been a constant source of love, concern, support and strength all these years, and I enjoyed every minutes of being with her.

Publications

The following journal publications, conference contributions and patents have been authored or co-authored during the course of Ph.D. project:

Journal Publications

- G. C. Park, **A. Taghizadeh**, and I.-S. Chung, "Hybrid grating reflectors: Origin of ultrabroad stopband," *Applied Physics Letter*, vol. 108, no. 14, 141108, 2016.
- **A. Taghizadeh**, J. Mørk, and I.-S. Chung, "Vertical-cavity in-plane heterostructures: Physics and applications," *Applied Physics Letter*, vol. 107, no. 18, 181107, 2015.
- **A. Taghizadeh**, J. Mørk, and I.-S. Chung, "Ultracompact resonator with high quality-factor based on a hybrid grating structure," *Optics Express*, vol. 23, no. 10, pp. 14913-14921, 2015.
- G. C. Park, W. Xue, **A. Taghizadeh**, E. Semenova, K. Yvind, J. Mørk, I.-S. Chung, "Hybrid vertical-cavity laser with lateral emission into a silicon waveguide," *Laser & Photonics Review*, vol. 9, no. 3, pp. L11-L15 2015.
- **A. Taghizadeh**, G. C. Park, J. Mørk, and I.-S. Chung, "Hybrid grating reflector with high reflectivity and broad bandwidth," *Optics Express*, vol. 22, no. 18, pp. 21175-21184, 2014.

Submitted or Prepared Manuscripts

- **A. Taghizadeh**, J. Mørk, and I.-S. Chung, "Numerical investigation of vertical cavity lasers with subwavelength gratings using the Fourier modal method," *submitted to Journal of Lightwave Technology*, 2016.

Conference Contributions

- I.-S. Chung, **A. Taghizadeh**, S. Learkthanakhachon, G. C. Park, "Hybrid III-V on Si grating as a broadband reflector and a high-Q resonator (Invited paper)," *Proc. SPIE* 9757, 9757-11 (2016).

- **A. Taghizadeh**, J. Mørk, and I.-S. Chung, "A new compact broadband reflector: The hybrid grating," *Conference on Lasers and Electro-Optics/Europe and the European Quantum Electronics Conference (CLEO/Europe-EQEC)*, 2015.
- **A. Taghizadeh**, J. Mørk, and I.-S. Chung, "Effect of in-plane mirror dispersion on vertical cavities based on high-contrast grating mirrors," *Conference on Lasers and Electro-Optics (CLEO)*, 2015.
- **A. Taghizadeh**, J. Mørk, and I.-S. Chung, "Comparison of different numerical methods for quality factor calculation of nano and micro photonic cavities," *Proc. of 8th International Congress on Advanced Electromagnetic Materials in Microwaves and Optics (META)*, 2014.

Patents

- I.-S. Chung and **A. Taghizadeh**, "High-Q resonator," *European patent*, EP 14163786.8, 2014.
- I.-S. Chung and **A. Taghizadeh**, "Hybrid grating reflector," *European patent*, EP 14163768.6, 2014.

Contents

List of Abbreviations

1D . . . . . One-dimensional, one dimension.

1.5D . . . . . One-half-dimensional, in this thesis refer to two-dimensional structures or simulations where one dimension is periodic.

2D . . . . . Two-dimensional, two dimension.

2.5D . . . . . Two-half dimensional, in this thesis refer to three-dimensional structures or simulations where one dimension is periodic.

3D . . . . . Thee-dimensional, three dimension.

DBR . . . . . Distributed Bragg reflector.

LED . . . . . Light emitting diode.

HCG . . . . . High-index-contrast grating.

HG . . . . . Hybrid grating.

FDFD . . . . . Finite-difference frequency-domain.

FDTD . . . . . Finite-difference time-domain.

FEM . . . . . Finite element method.

FMM . . . . . Fourier modal method.

PhC . . . . . Photonic crystal.

PML . . . . . Perfectly matched layer.

PT . . . . . Parity-time.

Q-factor . . . . Quality-factor.

QD . . . . . Quantum dot.

QED . . . . . Quantum electrodynamics.

QW . . . . . Quantum well.

QNM . . . . . Quasi-normal mode.

TE . . . . . Transverse electric.

TM . . . . . Transverse magnetic.

VCI . . . . . Vertical cavity in-plane.

VCSEL . . . . Vertical-cavity surface-emitting laser.

What is it that we human beings ultimately depend on? We depend on our words. We are suspended in language. Our task is to communicate experience and ideas to others.

— Niels Bohr

1 Introduction

Contents

The subject of this Ph.D. dissertation belongs to the field of nanophotonics, which is the science of employing photonics for nanometer-scale objects. What is photonics? Photonics is the science and technology of generating, detecting and manipulating light or more precisely photon. Photonics has come into use due to the analogy to electronics, which involves the control of electrons [1]. Due to the importance of this science for humans and their future developments, the United Nations proclaimed 2015 as the International Year of Light and Light-based Technologies (IYL 2015) [2]. This work is performed on the subject of laser, which is one of the most important photonic devices which revolutionized the 20th century after its invention, particularly the communications industry. After the development of optical fibers, the idea of optical interconnect, i.e. replacing electrical interconnects by their optical counterparts, changed this industry entirely. In this chapter, the main motivation of this Ph.D. thesis, which is about employing novel vertical cavity laser structures for optical interconnects in chip-level applications, is presented. The importance of modeling and numerical simulations for novel laser

structures is also explained. Finally, a short summary of the main thesis highlights and an overview of the dissertation are provided.

1.1 Chip-Level Optical Interconnects and Silicon Photonics

Vertical-cavity surface-emitting laser (VCSEL) was first proposed and fabricated by K. Iga and his colleagues at the Tokyo Institute of Technology, Japan in 1977 and 1979, respectively [3], [4]. A VCSEL consists of a thin semiconductor active region which is sandwiched between two highly-reflective mirrors. Conventionally, the mirrors were formed as distributed Bragg reflectors (DBRs). In the VCSEL, the light is propagating vertically between the mirrors and it is emitted in the normal-direction to the surface. Initially, VCSELs were working at low temperature and in pulsed-operation regime [4]. However, after several years of research, continuous-wave room-temperature GaAs VCSELs at 850 nm wavelength were demonstrated successfully [5]. Due to their various suitable characteristics such as narrow beam divergence, low power consumption and high modulation bandwidth, VCSELs are used widely for optical communications [6].

Over the last several decades, the daily amount of data being transferred globally is increasing by an exponential trend. Optical communications were the major reason which makes this huge growth possible, since large amount of data can be transmitted with high speed and low power consumption over long distance through the optical fibers. Initially, semiconductor diode lasers and optical fibers were used to make a global area network (GAN) between different continents, in which the transmission distance could be thousands of kilometers [7]. Later, optical interconnects were employed for shorter-distance networks of wide area network (WAN), metropolitan area network (MAN) and local area network (LAN) [7].

The idea of optical interconnect, seems naturally to be pushed toward the shorter-distance communications such as rack-to-rack, board-to-board, module-to-module, chip-to-chip and finally on-chip communications as shown in Fig. 1.1, particularly for internet data servers and high-performance computing (HPC) applications, where huge amount of data should be transmitted with high speed. However, for short-distance communications, low power consumption is as important as high modulation speed, since the density of the optical interconnect becomes larger for shorter-distance communications. Furthermore, there are other motivations for employing optical interconnects at chip-level; power consumption restrictions and cross-talk problem of electrical interconnects. It is well-known that more than half

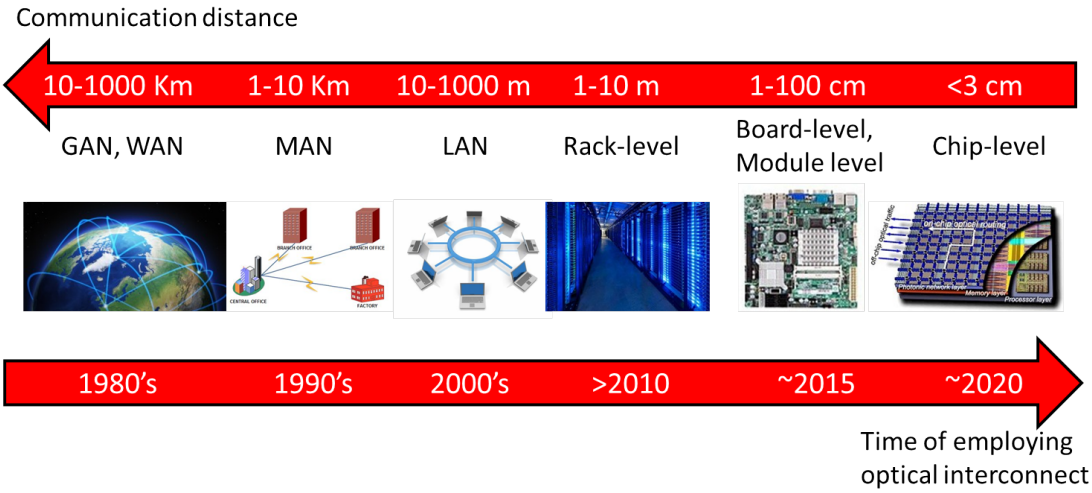

Figure 1.1: Time-evolution of optical interconnect employment in various network levels [7].

of the total power consumed inside a central processing unit (CPU), is lost in its electrical interconnects [8]. The power consumption of the electrical interconnects is mainly due to the capacitance and resistance of the electrical wires, and it is increasing for higher-speed devices. This makes a big challenge for developing high speed electronic devices for future computers [9]. Furthermore, for high signal-density and high speed applications, the cross-talk between nearby electrical interconnects through capacitive or inductive coupling is a major issue [9]. These problems may be efficiently eliminated by using optical interconnects at chip-level [9].

The main candidate for realizing chip-level optical interconnect is silicon photonics [9], [10]. Silicon has a number of important properties which makes it a suitable material and platform, such as fabrication possibility of silicon devices using CMOS technology which reduces the device cost, large refractive-index of silicon which makes the photonic devices compact, and good material properties such as low-defect wafer, and high thermal conductivity [11]. For realizing optical interconnects in silicon photonics, we may think of two general approaches [10]; using an integrated optical modulator with an off-chip light source, or a direct-modulation of an on-chip light source which is our chosen approach. On-chip light source provide better performance in terms of energy efficiency and can be a much cheaper solution [10], [12], [13]. Unfortunately, since silicon is an indirect band-gap material, it is very inefficient as a light source. Therefore, there are several approaches for making a light source in silicon platform, such as silicon Raman lasers, epitaxial lasers on silicon, and hybrid silicon lasers [11], [13]. Among them, hybrid silicon platform, which heterogeneously integrates III-V functionality on the silicon-on-insulator (SOI)

platform by using molecular wafer-bonding process, seems very attractive, since it has the best performance and the most potential for future on-chip light sources [13]. In the last decade, various types of hybrid silicon lasers are demonstrated [14]–[19]. For future chip-level and module-level optical interconnects, it is also required that energy consumption becomes less than 100 fJ/bit [9]. For this purpose, few power-efficient lasers are proposed and experimentally demonstrated such as a photonic crystal laser employing nano-size cavity with power consumption of a few fJ/bit and possibility of integration using wafer bonding process [20], [21]. VCSEL is also suggested as a potential candidate for future chip-level optical interconnects [9].

1.2 Novel Vertical Cavity Lasers

State-of-the-art VCSELs, can be made power-efficient (e.g. the energy consumption can be as low as 59 fJ/bit) [22], [23] and also integrated to silicon [17]. However, using the conventional VCSELs for chip-level optical interconnects is not feasible, since coupling output light from the VCSEL into an in-plane silicon waveguide is not straightforward, requiring extra efforts such as a grating coupler [19]. Recently, a hybrid laser structure was proposed using silicon high-index-contrast grating (HCG) as shown schematically in Fig. 1.2(a), which seems a promising candidate for silicon-integrated light source applications [24]. Introducing the HCG as bottom reflector can maintain the desirable properties of the VCSEL and increases the laser speed considerably, since it can reduce the modal volume (or equivalently increase the optical confinement factor) compared to the conventional VCSEL [18]. This laser structure, which is referred to as HCG-based vertical cavity laser structure, is also power-efficient and it shows low threshold current as low as state-of-the-art VCSELs [18]. Moreover, employing the HCG in vertical cavity laser results in novel properties such as exotic modal behavior [25], MEMS-based wavelength tunability [26], [27], and strong single-transverse-mode operation [28].

HCG is a special class of subwavelength grating, in which the grating period is close to the incident light wavelength and there is a large refractive-index contrast between the grating bars and materials surround it. Due to the large refractive-index contrast in the grating layer, HCG can provide extraordinary properties that have not been reported for conventional guided-mode resonance (GMR) filters with similar periodicity, including high reflectivity ($> 99\%$) over a broad bandwidth [29]–[31], or high quality factor resonances ($Q > 10^7$) [32], [33]. Compared to the diffraction gratings, only the 0-th diffraction order is propagating after being reflected or transmitted by HCG, since the grating is near-subwavelength. Even though, the

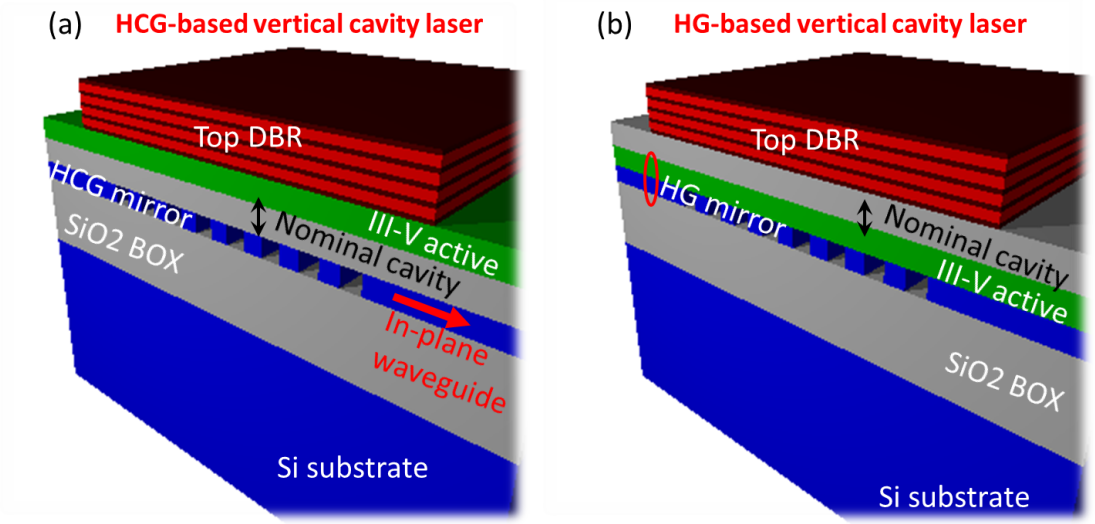

Figure 1.2: Schematic of a (a) HCG-based vertical cavity laser structure, (b) HG-based vertical cavity laser structure.

HCG structure is similar to a photonic crystal (PhC) structure, it operates above the light line compared to the PhC, which is employed below the light-line [34].

Based on the HCG, our group has suggested a new type of reflector, referred to as hybrid grating (HG), which consists of a grating layer covered by an un-patterned high refractive-index cap layer [35], [36]. This new reflector shows large reflectivity in a broad wavelength range, even broader than the HCG does [35]. An interesting possibility with the HG is that the cap layer may include an active material. Using this active HG, one may implement a new type of vertical cavity laser structure which is referred to as HG-based vertical cavity laser structure as illustrated in Fig. 1.2(b). This novel structure has more feasible fabrication process and more importantly, it possesses superior thermal properties compared to its HCG-based counterpart, since the active region is in the direct contact with the grating layer. Therefore, HCG/HG-based vertical cavity laser seem to be an interesting candidate for Si-integrated light source applications and they are investigated theoretically in this thesis.

1.3 Numerical Simulations

Laser diode physics are affected by a number of different physical processes which take place inside the laser, such as optical, electrical and thermal phenomena as shown in Fig. 1.3. The interaction between these phenomena is complex and in many cases non-linear effects are important [7]. Therefore, it is almost impossible to design accurately and predict the exact behavior of a laser without numerical simulations.

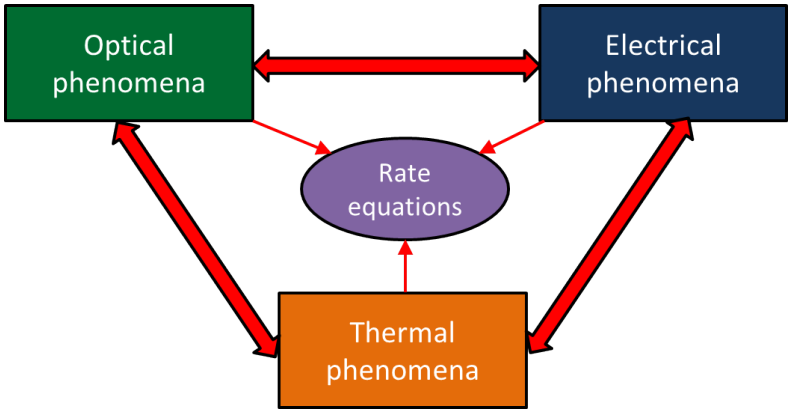

Figure 1.3: Physical phenomena and their interaction in a laser diode [7].

Extensive and accurate numerical simulations should be done to analyze the laser performance before its fabrication, since the fabrication and characterization of a novel laser structure is a difficult, time-consuming and expensive task.

Simulating a complete laser, including all the above mentioned physical phenomena and their complex interactions, is a difficult task. Even though, there are several commercial software tools available to perform multi-physics simulations [37]–[39], usually a complete simulation is not feasible, since extensive computing and memory resources are required. Furthermore, the complex nature of the system makes the interpretation of the simulation results very difficult. Therefore, since the beginning of laser history, there have been huge attempts to make the laser modeling as simple as possible and at the same time rigorous and accurate. Fortunately, by understanding the main physical mechanisms in a laser, it is possible to simplify the problem considerably. Particularly, it is possible to perform the optical, electrical and thermal simulations separately and then introduce a set of rate equations to connect these phenomena together [7], which is the approach used in this thesis. Particularly, modeling the optical phenomena in a HCG/HG-based vertical cavity laser is a challenging task, since, 1) there is high refractive-index contrast in the structure, 2) the smallest structural size is close to the working wavelength, and 3) there is no cylindrical symmetry in the structure which makes it impossible to simplify the modeling similar to conventional VCSELs. Therefore, Maxwell's equations should be solved in their vectorial form.

There are many different numerical techniques for rigorously solving Maxwell's equations such as finite-difference time-domain (FDTD) [40], finite-difference frequency-domain (FDFD) [41], finite element method (FEM) [42], method of lines (MoL) [43], Fourier modal method (FMM) [44], etc. Each method has its own advantages and drawbacks, or may be suitable for a particular sort of problem.

Among these methods, the FMM which is also referred to as rigorous coupled wave analysis (RCWA), is particularly efficient for solving the Maxwell's equations in periodic structures. The FMM was first introduced for rigorously solving grating problems in early 80s [45]. Due to its simplicity and robustness, it was used later for simulating other type of structures such as corrugated waveguides [46], [47], optical couplers [47], plasmonics structures [48], and PhC structures [49]–[53]. It is a special class of mode expansion techniques (or modal methods). In these methods, the structure is discretized into layers, the eigenmodes of each layer are determined, and the eigenmodes of the adjacent layers are connected using mode matching at the interface. Modal methods, provides valuable insight about the physics of the simulated structure by giving direct access to interesting physical parameters such as mode profiles, effective-indices and scattering coefficients in the structure [41]. Due to its simple implementation and robustness, the FMM is now considered as one of the most-employed type of modal methods.

The HCG/HG-based vertical cavity structure is a layered structure and also consists of a periodic grating layer as shown in Fig. 1.2, which makes it suitable for simulating with the FMM. Furthermore, the FMM is a fast and strong tool to study this structure, since several important parameters of interest such as reflectivity/transmissivity and cavity quality-factor (Q-factor) are obtained directly in this method, without requiring any post-processing of simulation data. Although, there are a few available software tools employing FMM, usually they do not provide full-access to all the intermediate calculations and parameters, which are required for understanding the detailed physics of a simulated structure. Therefore, we decided to develop an in-house three-dimensional FMM software tool to have the maximum flexibility. Different numerical tweaks are implemented to improve the performance of the method such as Li's factorization rule [54], [55], adaptive spatial resolution (ASR) technique [56], [57] and application of the structural mirror-reflection symmetries [58]. Absorbing boundary layers or perfectly matched layers (PMLs) are also implemented as non-linear stretched-coordinate technique to reduce the effect of finite computational domain [59].

1.4 Thesis Highlights

The focus of this work is on the theoretical investigation of subwavelength gratings and vertical cavity lasers employing them as the reflectors. The main novel results of this thesis can be summarized as:

- Several numerically-different techniques for computing the resonance wavelength and Q-factor of a cavity mode are introduced and compared quantitatively, which show good quantitative agreement with each others. The pros and cons of these methods are explained and the uncertainty of the calculation results is also discussed.

- The expressions for spatially-dependent rate equations employing a general expansion technique are derived. Particularly, they are solved numerically for a HCG-based vertical cavity laser using a set of Fourier basis, which can be more efficient numerically when it is combined with the FMM.

- Hybrid grating, which consists of a grating layer covered by a high refractive-index cap layer, is proposed. The physics behind its operation as a broadband reflector and high Q-factor resonator are discussed and confirmed with numerical simulations. Since, the cap layer may include active region, a new type of vertical cavity laser structure based on an active HG is proposed and investigated numerically, which displays superior thermal properties compared to the one based on the HCG.

- The cavity dispersion concept for vertical cavity structures is introduced and interpreted. An analytic expression for the dispersion is derived and its validity is confirmed by numerical simulations. In vertical cavity in-plane heterostructures, the significance of the cavity dispersion curvature and its influences on the modal properties are illustrated by extensive numerical simulations.

- The basic design rules for achieving high out-coupling efficiency into an in-plane silicon waveguide in a HCG-based vertical cavity laser, are discussed with an example which shows more than 68% out-coupling efficiency.

- A system of two laterally-coupled vertical cavities is proposed, which exhibits spontaneous breaking of the parity-time symmetry for the first time in vertical cavity platform.

1.5 Structure of the Dissertation

The thesis is organized as follows:

Chapter 1, Introduction: The main motivations of the work are reviewed.

Chapter 2, Laser Physics and Numerical Simulations: The fundamental of the laser physics is briefly explained. The details of implemented optical simulator, including all required mathematical expressions, are provided with several examples.

Chapter 3, Subwavelength Gratings: The physics behind the working mechanism of HCG and HG is explained by two different physical pictures and their applications as broadband reflectors or standalone resonators are discussed.

Chapter 4, Vertical Cavity Structures: Cavity dispersion is introduced as an important characteristic of the vertical cavity structures with novel reflectors such as HCG and HG. Several novel vertical cavity lasers are designed with interesting properties.

Chapter 5, Conclusion and Outlook: The major results of this dissertation are summarized and the possible future extension of the work are also discussed.

Appendix A, Homogeneous Layer Eigenmodes: The derivation of layer eigenmodes in a homogeneous layer with constant permittivity is presented.

Appendix B, Redheffer Star Product Variants: Tow other forms of Redheffer star product are provided in this Appendix.

Appendix C, Simulation Parameters: The structure dimensions and refractive-indices used for some of the numerical examples in dissertation are gathered in this Appendix.

References

[1] B. E. A. Saleh and M. C. Teich, *Fundamentals of Photonics*, 2nd Ed. John Wiley & Sons, Ltd, 2007 (cit. on p. 1).

[2] *International year of light: http://www.light2015.org/home.html* (cit. on p. 1).

[3] H. Soda, K.-I. Iga, C. Kitahara, and Y. Suematsu, "GaInAsP/InP surface emitting injection lasers", *Japanese Journal of Applied Physics*, vol. 18, no. 12, pp. 2329–2330, 1979 (cit. on p. 2).

[4] K. Iga, "Surface-emitting laser-its birth and generation of new optoelectronics field", *IEEE Journal of Selected Topics in Quantum Electronics*, vol. 6, no. 6, pp. 1201–1215, 2000 (cit. on p. 2).

[5] F. Koyama, S. Kinoshita, and K. Iga, "Room-temperature continuous wave lasing characteristics of a GaAs vertical cavity surface-emitting laser", *Applied Physics Letters*, vol. 55, no. 3, pp. 221–222, 1989 (cit. on p. 2).

[6] S. F. Yu, *Analysis and Design of Vertical Cavity Surface Emitting Lasers*. Hoboken, NJ, USA: John Wiley & Sons, Inc., 2003 (cit. on p. 2).

[7] A. Mutig, *High Speed VCSELs for Optical Interconnects*. Berlin, Heidelberg: Springer, 2011 (cit. on pp. 2, 3, 5, 6).

[8] N. Magen, A. Kolodny, U. Weiser, and N. Shamir, "Interconnect-power dissipation in a microprocessor", in *Proceedings of the 2004 international workshop on System level interconnect prediction - SLIP '04*, New York, New York, USA: ACM Press, 2004, pp. 7–13 (cit. on p. 3).

[9] D. A. B. Miller, "Optical interconnects to electronic chips", *Applied Optics*, vol. 49, no. 25, F59–F70, 2010 (cit. on pp. 3, 4).

[10] M. J. R. Heck and J. E. Bowers, "Energy efficient and energy proportional optical interconnects for multi-core processors: driving the need for on-chip sources", *IEEE Journal of Selected Topics in Quantum Electronics*, vol. 20, no. 4, pp. 332–343, 2014 (cit. on p. 3).

[11] D. Liang and J. E. Bowers, "Recent progress in lasers on silicon", *Nature Photonics*, vol. 4, no. 8, pp. 511–517, 2010 (cit. on p. 3).

[12] M. J. R. Heck, J. F. Bauters, M. L. Davenport, J. K. Doylend, S. Jain, G. Kurczveil, S. Srinivasan, Yongbo Tang, and J. E. Bowers, "Hybrid silicon photonic integrated circuit technology", *IEEE Journal of Selected Topics in Quantum Electronics*, vol. 19, no. 4, p. 6 100 117, 2013 (cit. on p. 3).

[13] Z. Zhou, B. Yin, and J. Michel, "On-chip light sources for silicon photonics", *Light: Science & Applications*, vol. 4, no. 11, e358, 2015 (cit. on pp. 3, 4).

[14] H. Park, A. W. Fang, S. Kodama, and J. E. Bowers, "Hybrid silicon evanescent laser fabricated with a silicon waveguide and III-V offset quantum wells", *Optics Express*, vol. 13, no. 23, pp. 9460–9464, 2005 (cit. on p. 4).

[15] A. W. Fang, H. Park, O. Cohen, R. Jones, M. J. Paniccia, and J. E. Bowers, "Electrically pumped hybrid AlGaInAs-silicon evanescent laser", *Optics Express*, vol. 14, no. 20, pp. 9203–9210, 2006 (cit. on p. 4).

[16] D. Liang, M. Fiorentino, T. Okumura, H.-H. Chang, D. T. Spencer, Y.-H. Kuo, A. W. Fang, D. Dai, R. G. Beausoleil, and J. E. Bowers, "Electrically-pumped compact hybrid silicon microring lasers for optical interconnects", *Optics Express*, vol. 17, no. 22, pp. 20 355–20 364, 2009 (cit. on p. 4).

[17] E. P. Haglund, S. Kumari, P. Westbergh, J. S. Gustavsson, G. Roelkens, R. Baets, and A. Larsson, "Silicon-integrated short-wavelength hybrid-cavity VCSEL", *Optics Express*, vol. 23, no. 26, pp. 33 634–33 640, Dec. 2015 (cit. on p. 4).

[18] G. C. Park, W. Xue, A. Taghizadeh, E. Semenova, K. Yvind, J. Mork, and I.-S. Chung, "Hybrid vertical-cavity laser with lateral emission into a silicon waveguide", *Laser & Photonics Reviews*, vol. 9, no. 3, pp. L11–L15, 2015 (cit. on p. 4).

[19] G. C. Park, W. Xue, E. Semenova, K. Yvind, J. Mork, and I. Chung, "III-V/SOI vertical cavity laser with in-plane output into a Si waveguide", in *Optical Fiber Communication Conference*, vol. 1, Washington, D.C.: OSA, 2015, W2A.17 (cit. on p. 4).

[20] S. Matsuo, A. Shinya, T. Kakitsuka, K. Nozaki, T. Segawa, T. Sato, Y. Kawaguchi, and M. Notomi, "High-speed ultracompact buried heterostructure photonic-crystal laser with 13 fj of energy consumed per bit transmitted", *Nature Photonics*, vol. 4, no. 9, pp. 648–654, 2010 (cit. on p. 4).

[21] K. Takeda, T. Sato, A. Shinya, K. Nozaki, W. Kobayashi, H. Taniyama, M. Notomi, K. Hasebe, T. Kakitsuka, and S. Matsuo, "Few-fJ/bit data transmissions using directly modulated lambda-scale embedded active region photonic-crystal lasers", *Nature Photonics*, vol. 7, no. 7, pp. 569–575, 2013 (cit. on p. 4).

[22] P. Moser, J. Lott, P. Wolf, G. Larisch, H. Li, N. Ledentsov, and D. Bimberg, "56 fJ dissipated energy per bit of oxide-confined 850 nm VCSELs operating at 25 Gbit/s", *Electronics Letters*, vol. 48, no. 20, pp. 1292–1293, 2012 (cit. on p. 4).

[23] W. H. Hofmann, P. Moser, and D. Bimberg, "Energy-efficient VCSELs for interconnects", *IEEE Photonics Journal*, vol. 4, no. 2, pp. 652–656, 2012 (cit. on p. 4).

[24] I.-S. Chung and J. Mork, "Silicon-photonics light source realized by III–V/Si-grating-mirror laser", *Applied Physics Letters*, vol. 97, no. 15, p. 151 113, 2010 (cit. on p. 4).

[25] A. Taghizadeh, J. Mork, and I.-S. Chung, "Vertical-cavity in-plane heterostructures: physics and applications", *Applied Physics Letters*, vol. 107, no. 18, p. 181 107, 2015 (cit. on p. 4).

[26] M. C. Y. Huang, Y. Zhou, and C. J. Chang-Hasnain, "A nanoelectromechanical tunable laser", *Nature Photonics*, vol. 2, no. 3, pp. 180–184, 2008 (cit. on p. 4).

[27] I.-S. Chung, V. Iakovlev, A. Sirbu, A. Mereuta, A. Caliman, E. Kapon, and J. Mork, "Broadband MEMS-tunable high-index-contrast subwavelength grating long-wavelength VCSEL", *IEEE Journal of Quantum Electronics*, vol. 46, no. 9, pp. 1245–1253, 2010 (cit. on p. 4).

[28] I.-S. Chung, J. Mork, P. Gilet, and A. Chelnokov, "Subwavelength grating-mirror VCSEL with a thin oxide gap", *IEEE Photonics Technology Letters*, vol. 20, no. 2, pp. 105–107, 2008 (cit. on p. 4).

[29] C. Mateus, M. Huang, Y. Deng, A. Neureuther, and C. Chang-Hasnain, "Ultrabroadband mirror using low-index cladded subwavelength grating", *IEEE Photonics Technology Letters*, vol. 16, no. 2, pp. 518–520, 2004 (cit. on p. 4).

[30] C. Mateus, M. Huang, L. Chen, C. Chang-Hasnain, and Y. Suzuki, "Broad-band mirror (1.12–1.62 um) using a subwavelength grating", *IEEE Photonics Technology Letters*, vol. 16, no. 7, pp. 1676–1678, 2004 (cit. on p. 4).

[31] R. Magnusson and M. Shokooh-Saremi, "Physical basis for wideband resonant reflectors", *Optics Express*, vol. 16, no. 5, pp. 3456–3462, 2008 (cit. on p. 4).

[32] Y. Zhou, M. Moewe, J. Kern, M. C. Huang, and C. J. Chang-Hasnain, "Surface-normal emission of a high-Q resonator using a subwavelength high-contrast grating", *Optics Express*, vol. 16, no. 22, pp. 17 282–17 287, 2008 (cit. on p. 4).

[33] T. T. Wu, S. H. Wu, T. C. Lu, and S. C. Wang, "GaN-based high contrast grating surface-emitting lasers", *Applied Physics Letters*, vol. 102, no. 8, p. 081 111, 2013 (cit. on p. 4).

[34] C. J. Chang-Hasnain and W. Yang, "High-contrast gratings for integrated optoelectronics", *Advances in Optics and Photonics*, vol. 4, no. 3, pp. 379–440, 2012 (cit. on p. 5).

[35] A. Taghizadeh, G. C. Park, J. Mork, and I.-S. Chung, "Hybrid grating reflector with high reflectivity and broad bandwidth", *Optics Express*, vol. 22, no. 18, pp. 21 175–21 184, 2014 (cit. on p. 5).

[36] A. Taghizadeh, J. Mork, and I.-S. Chung, "Ultracompact resonator with high quality-factor based on a hybrid grating structure", *Optics Express*, vol. 23, no. 11, pp. 14 913–14 921, 2015 (cit. on p. 5).

[37] *Comsol, comsol inc.: https://www.comsol.com/* (cit. on p. 6).

[38] *Silvaco, silvaco inc.: http://www.silvaco.com/* (cit. on p. 6).

[39] *Crosslight, crosslight software inc.: http://www.crosslight.com/* (cit. on p. 6).

[40] A. Taflove and S. C. Hagness, *Computational electrodynamics: the finite-difference time-domain method*, 3rd Ed. Artech House, 2005, vol. 58 (cit. on p. 6).

[41] A. Lavrinenko, N. Gregersen, J. Lagsgaard, and T. Sondergaard, *Numerical Methods in Photonics*. CRC Press, 2014 (cit. on pp. 6, 7).

[42] J. Jin, *The Finite Element Method in Electromagnetics*, 2nd Ed. 2002 (cit. on p. 6).

[43] R. Pregla, *Analysis of Electromagnetic Fields and Waves*. Chichester, UK: John Wiley & Sons, Ltd, 2008 (cit. on p. 6).

[44] H. Kim, J. Park, and B. Lee, *Fourier Modal Method and Its Applications in Computational Nanophotonics*. CRC Press, 2012 (cit. on p. 6).

[45] M. G. Moharam and T. K. Gaylord, "Rigorous coupled-wave analysis of planar-grating diffraction", *Journal of the Optical Society of America*, vol. 71, no. 7, pp. 811–818, 1981 (cit. on p. 7).

[46] P. Lalanne and E. Silberstein, "Fourier-modal methods applied to waveguide computational problems", *Optics Letters*, vol. 25, no. 15, pp. 1092–1094, 2000 (cit. on p. 7).

[47] E. Silberstein, P. Lalanne, J.-P. Hugonin, and Q. Cao, "Use of grating theories in integrated optics", *Journal of the Optical Society of America A*, vol. 18, no. 11, pp. 2865–2875, 2001 (cit. on p. 7).

[48] T. Weiss, N. a. Gippius, S. G. Tikhodeev, G. Granet, and H. Giessen, "Derivation of plasmonic resonances in the Fourier modal method with adaptive spatial resolution and matched coordinates", *Journal of the Optical Society of America A*, vol. 28, no. 2, pp. 238–244, 2011 (cit. on p. 7).

[49] L. Botten, N. Nicorovici, R. McPhedran, C. Sterke, and A. Asatryan, "Photonic band structure calculations using scattering matrices", *Physical Review E*, vol. 64, no. 4, p. 046 603, Sep. 2001 (cit. on p. 7).

[50] P. Lalanne and H. Benisty, "Out-of-plane losses of two-dimensional photonic crystals waveguides: electromagnetic analysis", *Journal of Applied Physics*, vol. 89, no. 2, pp. 1512–1514, 2001 (cit. on p. 7).

[51] P. Lalanne, "Electromagnetic analysis of photonic crystal waveguides operating above the light cone", *IEEE Journal of Quantum Electronics*, vol. 38, no. 7, pp. 800–804, 2002 (cit. on p. 7).

[52] G. Lecamp, J. P. Hugonin, and P. Lalanne, "Theoretical and computational concepts for periodic optical waveguides", *Optics Express*, vol. 15, no. 18, pp. 11 042–11 060, 2007 (cit. on p. 7).

[53] J. R. de Lasson, P. T. Kristensen, J. Mork, and N. Gregersen, "Roundtrip matrix method for calculating the leaky resonant modes of open nanophotonic structures", *Journal of the Optical Society of America A*, vol. 31, no. 10, pp. 2142–2151, 2014 (cit. on p. 7).

[54] L. Li, "Use of Fourier series in the analysis of discontinuous periodic structures", *Journal of the Optical Society of America A*, vol. 13, no. 9, pp. 1870–1876, 1996 (cit. on p. 7).

[55] L. Li, "New formulation of the Fourier modal method for crossed surface-relief gratings", *Journal of the Optical Society of America A*, vol. 14, no. 10, pp. 2758–2767, 1997 (cit. on p. 7).

[56] G. Granet, "Reformulation of the lamellar grating problem through the concept of adaptive spatial resolution", *Journal of the Optical Society of America A*, vol. 16, no. 10, pp. 2510–2516, 1999 (cit. on p. 7).

[57] G. Granet and J.-P. Plumey, "Parametric formulation of the Fourier modal method for crossed surface-relief gratings", *Journal of Optics A: Pure and Applied Optics*, vol. 4, no. 5, S145–S149, 2002 (cit. on p. 7).

[58] Z.-Y. Li and K.-M. Ho, "Application of structural symmetries in the plane-wave-based transfer-matrix method for three-dimensional photonic crystal waveguides", *Physical Review B*, vol. 68, no. 24, p. 245 117, 2003 (cit. on p. 7).

[59] J. P. Hugonin and P. Lalanne, "Perfectly matched layers as nonlinear coordinate transforms: a generalized formalization", *Journal of the Optical Society of America A*, vol. 22, no. 9, pp. 1844–1849, 2005 (cit. on p. 7).

One scientific epoch ended and another began with James Clerk Maxwell.

— Albert Einstein

2

Laser Physics and Numerical Simulations

Contents

In this chapter, the fundamental of laser physics and its numerical simulations are introduced. Firstly, the laser theory is discussed briefly by explaining the various electronic transitions in semiconductors. In section 2.2, the Fourier modal method (FMM), which is implemented for computing the optical properties of the laser structures in this work, is introduced and its numerical performance is improved by employing adaptive spatial resolution and absorbing boundary conditions. Scattering matrices are employed for modeling the interaction between fields in the neighboring layers. Several different numerical techniques for determining the resonance wavelength and quality-factor (Q-factor) of a cavity mode are implemented

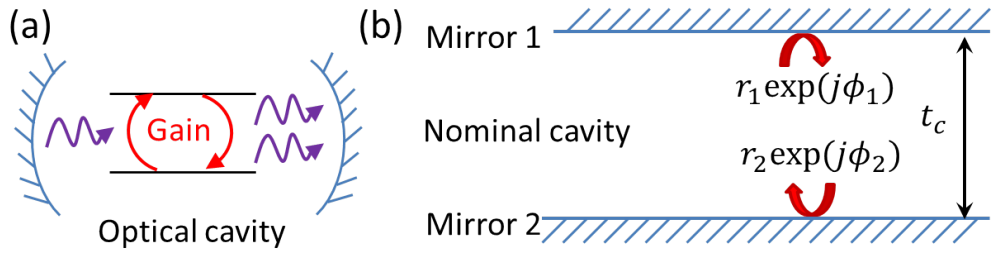

Figure 2.1: (a) A laser composed of a gain medium in a resonant optical cavity. (b) Schematic view of a Fabry-Perot cavity, consists of two mirrors and a nominal cavity between them with t_c thickness. r_i and ϕ_i are the reflectivity amplitudes and phases from the mirrors, respectively.

and compared in the FMM formalism. The convergence rate of resonance wavelength and Q-factor is also investigated. Furthermore, the expressions for threshold gain and optical confinement factor of a laser are shown with an example. Finally, the rate equations are introduced, which can simply connect various optical, electrical and thermal phenomena together in a complex laser structure. The last section deals with spatially-dependent rate equations by adding the carrier diffusion term to the standard rate equations. These rate equations are solved by the expansion techniques.

2.1 Introduction to Laser Theory

In the most general definition, a laser is a combination of a gain medium in a resonant optical cavity as shown schematically in Fig. 2.1(a). These two components are coupled together and form a system to convert the electrical energy to its optical counterpart. The first component of a laser is a resonant optical cavity. The cavity provides optical feedback, which is required to increase the photon density in the gain medium and consequently make a positive net gain [1]. There are various types of optical cavities for laser diodes such as Fabry-Perot cavities, photonic crystal cavities, ring and disk cavities, etc. A Fabry-Perot cavity consists of two mirrors separated by a distance t_c as shown schematically in Fig. 2.1(b). The lasing condition for a mode in the Fabry-Perot cavity is defined when the mode reproduce itself after a round-trip inside the cavity [1]:

$$r_1 \exp(j\phi_1) \exp(-j\bar{\beta}_c t_c) r_2 \exp(j\phi_2) \exp(-j\bar{\beta}_c t_c) = 1, \tag{2.1}$$

in which $\bar{\beta}_c$ is the complex propagation constant of the mode, r_1 and r_2 are modal reflectivity amplitude from the mirrors, and ϕ_1 and ϕ_2 are the reflectivity phases

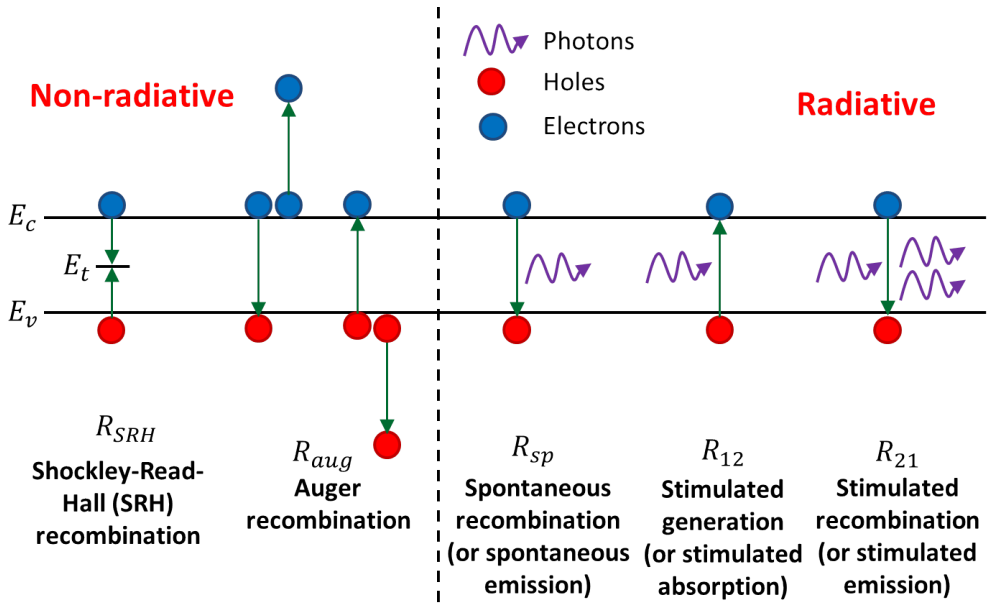

Figure 2.2: Various electronic transitions between conduction and valance bands in a semiconductor. Transitions are separated into non-radiative and radiative groups.

from the mirrors. Assuming a mode with frequency of ω_m, propagating with group refractive-index of $n_{c,g}$ and experiencing gain of $g_{c,t}$, results in $\bar{\beta}_c = n_{c,g}\omega_m/c + jg_{c,t}/2$.

By separating the real and imaginary parts of Eq. (2.2), the complete lasing condition becomes:

$$r_1 r_2 \exp\left(g_{c,t} t_c\right) = 1, \tag{2.2a}$$

$$\phi_1 + \phi_2 - 2\frac{n_{c,g} t_c}{c}\omega_m = 2m\pi, \tag{2.2b}$$

where m is the longitudinal mode order. The first equation defines the threshold condition for lasing of a mode, while the second one determines the resonance frequency of it. For a vertical-cavity surface-emitting laser (VCSEL), the value of t_c is relatively small and close to the laser working wavelength [1]. Therefore, a VCSEL requires highly-reflective mirrors (r_1 and r_2 should be very close to unity) to undergo a transition to lasing, i.e. satisfying Eq. (2.2a). Distributed Bragg reflectors (DBRs) are used in conventional VCSELs. However, VCSELs with novel mirror structures are the main topic of this dissertation.

Another ingredient of a laser is the gain medium. To obtain insight about the gain medium, the energy diagram of electrons should be known. In a bulk semiconductor, the energy levels make two isolated bands referred to as conduction and valance bands which are separated by the bandgap energy E_g. There are various types of mechanisms responsible for electron transitions between the conduction

and valance bands as shown in Fig. 2.2. These mechanisms are divided into two major groups, non-radiative and radiative processes, depending on whether they generate useful photons in the process. Generating light in semiconductors mainly occurs due to the radiative recombination processes, i.e. spontaneous recombination (or spontaneous emission) as in LEDs or stimulated recombination (or stimulated emission) as in laser diodes. The two processes of stimulated emission and stimulated absorption compete with each other, one consumes the photons, which makes the optical loss, and the other one generates photons, which makes the optical gain. The net optical gain in semiconductor is achieved when the stimulated emission rate is larger than the stimulated absorption term, a criteria called population inversion in laser physics [1]. Carriers are injected electrically to compensate the depleted ones in the conduction band.

2.2 Optical Simulations

Optical phenomena in a laser are modeled by solving vectorial Maxwell's equations in a three-dimensional (3D) space with appropriate boundary conditions for a given refractive-index profile. Among various methods for solving Maxwell's equations, we chose the FMM due to the reasons discussed in chapter 1. In this approach, assuming a distinct propagation direction such as the z-direction, the structure is discretized into layers. For each layer, the eigenmodes (guided and radiated modes) are calculated by solving an eigenvalue problem which is obtained by expanding the eigenmodes on a basis set of exponential functions. Due to the linearity of Maxwell's equations, the total field in the layer is a summation over all of these eigenmodes. Continuity of transverse electric and magnetic field components at the layer interfaces, results in a linear relationship between the mode coefficients in adjacent layers. Solving these equations for the mode coefficients, the field is determined for the whole structure. In this thesis, since we are mostly interested the vertical cavity structures employing a high-index-contrast grating (HCG) as shown schematically in Fig. 2.3, and hereafter referred to as HCG-based vertical cavities, most of the numerical simulations in this chapter are conducted on this structure. The calculations are performed on either a complete 3D structure [shown in Fig. 2.3(a)] or its two-dimensional (2D) cross-section [shown in Fig. 2.3(b)].

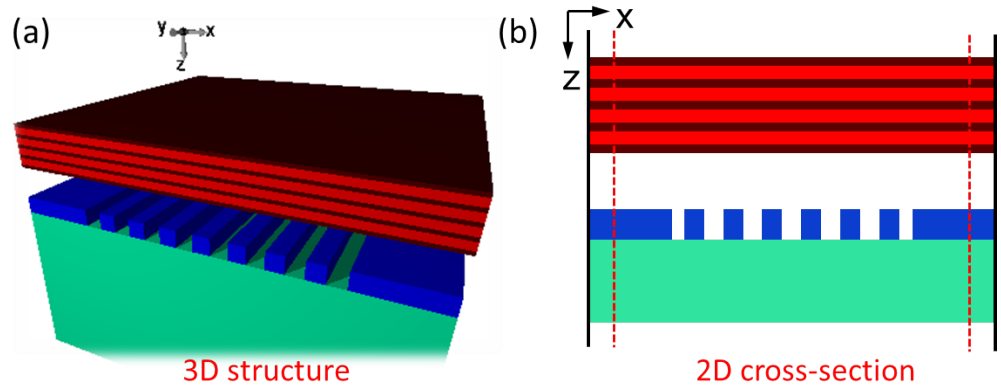

Figure 2.3: (a) Schematic view of a HCG-based vertical cavity structure used in 3D simulations. (b) The 2D cross-sectional view of the structure in (a).

2.2.1 Definitions and Conventions

Here, the main physical and mathematical conventions employed in this work are reviewed. If not stated otherwise, international system of units (SI units) with the Cartesian coordinate system is used. The main propagation direction is denoted by the z-direction and is referred to as the longitudinal direction, while the x-, y-directions are referred to as the transverse (or in-plane) directions. For transverse electric (TE) or transverse magnetic (TM) polarization, the electric field is assumed to be parallel or perpendicular to the grating bars, respectively. All vectors and matrices are indicated by bold letters. Table 2.1 shows a list of main conventions employed in this thesis.

2.2.2 Eigenmodes of a Layer

The first step in the FMM is to determine the eigenmodes and their propagation constants for each layer. Our starting point is Maxwell's equations for a source-free medium in frequency domain, assuming $\exp(+j\omega t)$ as the time harmonic dependency. Only linear materials are considered here, i.e. $\vec{\mathbf{D}} = \epsilon_0\epsilon_r\vec{\mathbf{E}}$ and $\vec{\mathbf{B}} = \mu_0\mu_r\vec{\mathbf{H}}$. It is easier to work with normalized magnetic field, i.e. $\vec{\tilde{\mathbf{H}}} = -j\sqrt{\mu_0/\epsilon_0}\vec{\mathbf{H}}$ and normalized coordinate system, i.e. $\vec{\tilde{\mathbf{r}}} = k_0\vec{\mathbf{r}}$ (or equivalently $\tilde{\nabla}\times = k_0^{-1}\nabla\times$), since two similar equations are then obtained for the electric and magnetic fields as:

$$\tilde{\nabla} \times \vec{\mathbf{E}} = \mu_r\vec{\tilde{\mathbf{H}}}, \tag{2.3a}$$

$$\tilde{\nabla} \times \vec{\tilde{\mathbf{H}}} = \epsilon_r\vec{\mathbf{E}}. \tag{2.3b}$$

From now on, the ' ˜ ' notation is omitted from the equations, and normalized variables are used. However, we should keep in mind that to obtain the real value,

Symbol	Name	Value
x, y, z	Cartesian coordinate system	
$\vec{\mathbf{x}}, \vec{\mathbf{y}}, \vec{\mathbf{z}}$	Cartesian unit vectors	
$\vec{\mathbf{r}}$	Position vector	$x\vec{\mathbf{x}} + y\vec{\mathbf{y}} + z\vec{\mathbf{z}}$
∂_α	Derivative operator	$\dfrac{\partial}{\partial\alpha}$
∇	Del (or nabla) operator	$\partial_x\vec{\mathbf{x}} + \partial_y\vec{\mathbf{y}} + \partial_z\vec{\mathbf{z}}$
∇^2	Laplace operator	$\partial_x^2 + \partial_y^2 + \partial_z^2$
$\mathbf{I}$	Identity matrix	
$\mathbf{O}$	Zero matrix	
ϵ_0	Vacuum permittivity	8.8542e-12 F/m
μ_0	Vacuum permeability	1.2566e-6 A.m
c	Speed of light in vacuum	$\dfrac{1}{\sqrt{\epsilon_0\mu_0}} \approx$ 3e8 m/s
ω	Frequency	
$\tilde{\omega}$	Complex frequency	
λ_0	Wavelength in vacuum	
λ	Wavelength in medium	
k_0	Wavenumber in vacuum	$\dfrac{\omega}{c} = \dfrac{2\pi}{\lambda_0}$
n_g	Group refractive-index	
v_g	Group velocity	$\dfrac{c}{n_g}$
ϵ_r	Relative permittivity	
μ_r	Relative permeability	
$\vec{\mathbf{E}}$	Electric field vector	
$\vec{\mathbf{H}}$	Magnetic field vector	
Γ	Optical confinement factor	
g_{th}	Threshold gain	
λ_r	Resonance wavelength	
Q	Quality factor	

Table 2.1: The list of main conventions employed in this work with their corresponding meaning.

all normalized length scales should be divided by k_0, all normalized wavevectors should be multiplied by k_0, and all normalized magnetic fields should be multiplied by $j\sqrt{\epsilon_0/\mu_0}$. By eliminating the z-component of the $\vec{\mathbf{E}}$ and $\vec{\mathbf{H}}$ fields, the following equations are obtained for the transverse electric and magnetic field components:

$$\partial_z \begin{pmatrix} E_x \\ E_y \end{pmatrix} = \pounds_{EH} \begin{pmatrix} H_x \\ H_y \end{pmatrix} = \begin{pmatrix} -\partial_x \epsilon_r^{-1} \partial_y & \mu_r + \partial_x \epsilon_r^{-1} \partial_x \\ -\mu_r - \partial_y \epsilon_r^{-1} \partial_y & \partial_y \epsilon_r^{-1} \partial_x \end{pmatrix} \begin{pmatrix} H_x \\ H_y \end{pmatrix}, \tag{2.4a}$$

$$\partial_z \begin{pmatrix} H_x \\ H_y \end{pmatrix} = \pounds_{HE} \begin{pmatrix} E_x \\ E_y \end{pmatrix} = \begin{pmatrix} -\partial_x \mu_r^{-1} \partial_y & \epsilon_r + \partial_x \mu_r^{-1} \partial_x \\ -\epsilon_r - \partial_y \mu_r^{-1} \partial_y & \partial_y \mu_r^{-1} \partial_x \end{pmatrix} \begin{pmatrix} E_x \\ E_y \end{pmatrix}. \tag{2.4b}$$

Here $\pounds_{HE}$ and $\pounds_{EH}$ are the differential field operators.

In the optical frequency range and for most practical materials, μ_r is unity [2]. For each layer, the permittivity function is invariant in the z-direction, i.e. $\epsilon_r(x, y, z) = \epsilon_r(x, y)$. In the FMM, it is assumed that the permittivity function is periodic in the both x- and y-directions with periodicities of Λ_x and Λ_y, respectively, i.e. $\epsilon_r(x + m\Lambda_x, y + n\Lambda_y) = \epsilon_r(x, y)$ for any integer m and n. Therefore, the permittivity function ϵ_r can be expanded into a 2D Fourier series where each term corresponds to a spatial harmonic:

$$\epsilon_r(x, y) = \sum_{m,n} \epsilon_{mn} \exp\left[j(g_{xm}x + g_{yn}y)\right], \tag{2.5a}$$

$$\epsilon_{mn} = \frac{1}{\Lambda_x \Lambda_y} \iint_{\Lambda_x, \Lambda_y} \epsilon_r(x, y) \exp\left[-j(g_{xm}x + g_{yn}y)\right] \mathrm{dxdy}, \tag{2.5b}$$

in which $g_{xm} = 2m\pi/\Lambda_x$ and $g_{yn} = 2n\pi/\Lambda_y$ are the reciprocal lattice vectors of the rectangular unit cell. For an infinite Fourier series, m and n are the Fourier series indices, vary from $-\infty$ to $+\infty$. However, for a truncated case in numerical calculations, $m = -m_x, ..., -1, 0, 1, ...m_x$ and $n = -n_y, ..., -1, 0, 1, ...n_y$, and the total number of Fourier terms are $M_x = 2m_x + 1$, $N_y = 2n_y + 1$ and $N_t = M_x N_y$ in the x-direction, y-direction and both directions, respectively. By increasing the number of Fourier terms, the computational accuracy can be increased. Due to Bloch's theorem [3], a pseudo-periodic Fourier series can be used for expanding $\vec{\mathbf{E}}$ and $\vec{\mathbf{H}}$ fields:

$$\vec{\mathbf{E}}(x, y, z) = \sum_{m,n} [S_{x,mn}(z)\vec{\mathbf{x}} + S_{y,mn}(z)\vec{\mathbf{y}} + S_{z,mn}(z)\vec{\mathbf{z}}] \exp\left[j(k_{xm}x + k_{yn}y)\right], \tag{2.6a}$$

$$\vec{\mathbf{H}}(x, y, z) = \sum_{m,n} [U_{x,mn}(z)\vec{\mathbf{x}} + U_{y,mn}(z)\vec{\mathbf{y}} + U_{z,mn}(z)\vec{\mathbf{z}}] \exp\left[j(k_{xm}x + k_{yn}y)\right], \tag{2.6b}$$

where $k_{xm} = k_{x0} + g_{xm}$ and $k_{yn} = k_{y0} + g_{yn}$ are the spatial wavevector components in the transverse directions, and k_{x0} and k_{y0} are incident wavevector components

in the x- and y-directions, respectively. The sets $\{S_{x,mn}(z), S_{y,mn}(z), S_{z,mn}(z)\}$ and $\{U_{x,mn}(z), U_{y,mn}(z), U_{z,mn}(z)\}$ are z-dependent coefficients for the electric and magnetic fields, respectively.

These Fourier series expansions transform Maxwell's differential equations to their matrix representations [4]:

$$\partial_z \begin{pmatrix} \mathbf{S}_x \\ \mathbf{S}_y \end{pmatrix} = \mathbf{P} \begin{pmatrix} \mathbf{U}_x \\ \mathbf{U}_y \end{pmatrix} = \begin{pmatrix} \mathbf{K}_x \mathcal{E}^{-1} \mathbf{K}_y & \mathbf{I} - \mathbf{K}_x \mathcal{E}^{-1} \mathbf{K}_x \\ \mathbf{K}_y \mathcal{E}^{-1} \mathbf{K}_y - \mathbf{I} & -\mathbf{K}_y \mathcal{E}^{-1} \mathbf{K}_x \end{pmatrix} \begin{pmatrix} \mathbf{U}_x \\ \mathbf{U}_y \end{pmatrix}, \tag{2.7a}$$

$$\partial_z \begin{pmatrix} \mathbf{U}_x \\ \mathbf{U}_y \end{pmatrix} = \mathbf{Q} \begin{pmatrix} \mathbf{S}_x \\ \mathbf{S}_y \end{pmatrix} = \begin{pmatrix} \mathbf{K}_x \mathbf{K}_y & \mathcal{E} - \mathbf{K}_x^2 \\ \mathbf{K}_y^2 - \mathcal{E} & -\mathbf{K}_y \mathbf{K}_x \end{pmatrix} \begin{pmatrix} \mathbf{S}_x \\ \mathbf{S}_y \end{pmatrix}, \tag{2.7b}$$

where $\mathbf{K}_x$ and $\mathbf{K}_y$ are diagonal matrices containing the spatial wavevector components k_{xm} and k_{yn}, respectively, and matrix $\mathcal{E}$ is a Toeplitz matrix made from the Fourier coefficients ϵ_{mn}. A Toeplitz matrix $\mathbf{A}$ with A_{ij} element is obtained from a vector $\mathbf{a}$ with elements a_i as $A_{ij} = a_{i-j}$. Vector sets $\{\mathbf{S}_x, \mathbf{S}_y\}$ and $\{\mathbf{U}_x, \mathbf{U}_y\}$ consist of Fourier series coefficients of the transverse components of $\vec{\mathbf{E}}$ and $\vec{\mathbf{H}}$ fields, respectively. By combining these two equations, an expression is obtained in terms of $\{\mathbf{S}_x, \mathbf{S}_y\}$ variables, and matrix $\mathbf{\Omega}$ is defined as $\mathbf{\Omega} = \mathbf{PQ}$. Assuming a z-dependency in the form of $\exp(\gamma z)$ for field components, the differential equation sets are transformed to an eigenvalue problem for matrix $\mathbf{\Omega}$, which is solved easily by a standard eigenvalue software package (MATLAB in the present case):

$$\partial_z^2 \begin{pmatrix} \mathbf{S}_x \\ \mathbf{S}_y \end{pmatrix} = \mathbf{\Omega} \begin{pmatrix} \mathbf{S}_x \\ \mathbf{S}_y \end{pmatrix} \quad \Rightarrow \quad \gamma^2 \begin{pmatrix} \mathbf{S}_x \\ \mathbf{S}_y \end{pmatrix} = \mathbf{\Omega} \begin{pmatrix} \mathbf{S}_x \\ \mathbf{S}_y \end{pmatrix}. \tag{2.8}$$

After solving the eigenvalue problem, eigenvalues b_i, $i = 1, 2, ..., 2N_t$ are found, where $b_i = \gamma_i^2$. There are two possibilities to choose either sign of $\pm\sqrt{b}$ for γ_i, i.e. there are two eigenvalues which share a single eigenvector, and the appropriate sign is chosen as it is discussed in Refs. [5], [6]. Each γ_i is referred to as an eigenmode propagation constant and its corresponding eigenvector $(\mathbf{w}_{x,i}, \mathbf{w}_{y,i})$ as a electric field eigenmode. All the eigenvectors together make a matrix $\mathbf{W}$, where eigenvector $(\mathbf{w}_{x,i}, \mathbf{w}_{y,i})$ is its ith column. A diagonal matrix $\mathbf{\Gamma}$ is also defined based on γ_i, and consequently $\mathbf{\Omega W} = \mathbf{W\Gamma}^2$. Furthermore, using Eqs. (2.7), the magnetic field eigenmode $(\mathbf{v}_{x,i}, \mathbf{v}_{y,i})$ is the ith column of the matrix $\mathbf{V} = \mathbf{QW\Gamma}^{-1}$.

After determining the layer eigenmodes, the total field in the layer will be a summation of all eigenmodes with their corresponding propagation constants, being

accompanied with a set of appropriate coefficients:

$$\begin{pmatrix}\mathbf{S}_x\\ \mathbf{S}_y\end{pmatrix} = \mathbf{W}\exp\left[-\mathbf{\Gamma}(z-z_1)\right]\mathbf{c}_p + \mathbf{W}\exp\left[\mathbf{\Gamma}(z-z_2)\right]\mathbf{c}_n, \tag{2.9a}$$

$$\begin{pmatrix}\mathbf{U}_x\\ \mathbf{U}_y\end{pmatrix} = -\mathbf{V}\exp\left[-\mathbf{\Gamma}(z-z_1)\right]\mathbf{c}_p + \mathbf{V}\exp\left[\mathbf{\Gamma}(z-z_2)\right]\mathbf{c}_n. \tag{2.9b}$$

where $\mathbf{c}_p$ and $\mathbf{c}_n$ are the coefficient vectors of the propagating waves in positive and negative directions, respectively, and the layer starts at $z = z_1$ and ends at $z = z_2$. The phase factors, $\exp\left[-\mathbf{\Gamma}z_1\right]$ and $\exp\left[-\mathbf{\Gamma}z_2\right]$, are introduced to prevent numerical overflow [5]. For a given excitation field, $\mathbf{c}_p$ and $\mathbf{c}_n$ can be found using appropriate boundary conditions as it will be discussed in section 2.2.3.

Li's Factorization Rule

It is known from Fourier theory that if a function is expressed as a multiplication of two other functions, e.g. $f(x) = g(x)h(x)$, in Fourier space, its Fourier coefficients will be obtained as the convolution of the Fourier coefficients:

$$f_n = \sum_{m=-\infty}^{\infty} g_{n-m}h_m, \tag{2.10}$$

where f_i, g_i and h_i are the corresponding Fourier coefficients. In matrix notation, $[\mathbf{f}] = [[\mathbf{g}]][\mathbf{h}]$, where $[[\mathbf{g}]]$ is the Toelptiz matrix composed of the Fourier coefficients of the g function. If g and h are discontinuous functions at a jump point with concurrent jumps, i.e. f is continuous, then the Fourier coefficients of the f function obtained from Eq. (2.10) will not converge smoothly at the jump point [7]. In this case, Li [7] showed that for fast convergence the inverse rule should be applied, which is expressed as:

$$[\mathbf{f}] = [[\mathbf{g}^{-1}]]^{-1}[\mathbf{h}]. \tag{2.11}$$

Applying this rule solved the well-known convergence problem of the FMM in the TM polarization [5], [8]. For a 2D Fourier series, this rule can be applied using fast Fourier-factorization rule [9], [10] or Normal-vector technique in the most general case [11], [12]. However, if the permittivity function has only surfaces parallel to the coordinate planes, the Li's factorization rule can be applied with simple modification of the eigenmode equations [13]. Firstly, several new matrices

are defined for a 2D periodic function $a(x,y)$ with Λ_x and Λ_y periodicity as [13]:

$$a_{mn} = \frac{1}{\Lambda_x \Lambda_y} \iint_{\Lambda_x,\Lambda_y} a(x,y) \exp\left[-jmk_x x - jnk_y y\right] \mathrm{dxdy}, \tag{2.12a}$$

$$\lceil a \rceil_{mn} = \frac{1}{\Lambda_x} \int_{\Lambda_x} a(x,y) \exp\left[-j(m-n)k_x x\right] \mathrm{dx}, \tag{2.12b}$$

$$\lfloor a \rfloor_{mn} = \frac{1}{\Lambda_y} \int_{\Lambda_y} a(x,y) \exp\left[-j(m-n)k_y y\right] \mathrm{dy}, \tag{2.12c}$$

$$\mathbf{A}_x : \lfloor \lceil a \rceil \rfloor_{mn,pq} = \lfloor \{ \lceil a \rceil \}_{mp} \rfloor_{nq}, \tag{2.12d}$$

$$\mathbf{A}_y : \lceil \lfloor a \rfloor \rceil_{mn,pq} = \lceil \{ \lfloor a \rfloor \}_{nq} \rceil_{mp}, \tag{2.12e}$$

$$\mathbf{A}_z : [[a]]_{mn,pq} = a_{m-p,n-q}, \tag{2.12f}$$

where $k_i = 2\pi/\Lambda_i$ for $i = x, y$.

Using Li's factorization rule in Maxwell's matrix equations, (2.7), results in a modification of matrices $\mathbf{P}$ and $\mathbf{Q}$ as:

$$\mathbf{P} = \begin{pmatrix} \mathbf{K}_x \mathcal{E}_z^{-1} \mathbf{K}_y & \mathbf{I} - \mathbf{K}_x \mathcal{E}_z^{-1} \mathbf{K}_x \\ \mathbf{K}_y \mathcal{E}_z^{-1} \mathbf{K}_y - \mathbf{I} & -\mathbf{K}_y \mathcal{E}_z^{-1} \mathbf{K}_x \end{pmatrix}, \tag{2.13a}$$

$$\mathbf{Q} = \begin{pmatrix} \mathbf{K}_x \mathbf{K}_y & \mathcal{E}_y - \mathbf{K}_x^2 \\ \mathbf{K}_y^2 - \mathcal{E}_x & -\mathbf{K}_y \mathbf{K}_x \end{pmatrix}, \tag{2.13b}$$

where $\mathcal{E}_\alpha$, $\alpha = x, y, z$ are found from the permittivity function using Eqs. (2.12), $\mathcal{E}_x = \lfloor \lceil \epsilon_r \rceil \rfloor$, $\mathcal{E}_y = \lceil \lfloor \epsilon_r \rfloor \rceil$ and $\mathcal{E}_z = [[\epsilon_r]]$. It should be mentioned that if the permittivity function has interfaces, which are not parallel to the coordinate planes such as circular holes, we may discretize the permittivity function into several slices and make a staircase approximation of it [14], [15]. With a sufficient number of slices, this approximation results in the correct evaluation for most problems [14]. However, it may provide slow convergence for some problems [10].

Adaptive Spatial Resolution

If there is a large refractive-index contrast in a layer cross-section permittivity, it will make the Fourier series expansion less effective due to the well-known Gibbs phenomena [16]. However, the efficiency of Fourier series expansion was shown to be improved dramatically by introducing the concept of adaptive spatial resolution (ASR). This method was first introduced for 1D single grating layer problem [17], later it was expanded to multilayer structures [18] and 2D structures [19]. In this technique, a new coordinate system is introduced, which increases the spatial resolution around the discontinuities of the permittivity function [16], [17]. The

coordinate transformation function is an analytic smooth function such as the one defined in Ref. [16]–[18].

Starting from Maxwell's equations for the electric field components (E_x, E_y, E_z) and the magnetic field components (H_x, H_y, H_z) in the original coordinate system (x, y, z), they will be rewritten for a transformed coordinate system $(\bar{x}, \bar{y}, \bar{z})$, where $x = f_x(\bar{x})$, $y = f_y(\bar{y})$ and $z = \bar{z}$. The functions g_x and g_y are defined as $g_x = \partial f_x/\partial \bar{x}$ and $g_y = \partial f_y/\partial \bar{y}$, respectively. Maxwell's equations for the transformed transverse field components ($E_{\bar{i}} = E_i g_i$, $H_{\bar{i}} = H_i g_i$; $i = x, y$) then become:

$$\partial_{\bar{z}} \begin{pmatrix} E_{\bar{x}} \\ E_{\bar{y}} \end{pmatrix} = \pounds_{EH} \begin{pmatrix} H_{\bar{x}} \\ H_{\bar{y}} \end{pmatrix} = \begin{pmatrix} -\partial_{\bar{x}} \epsilon_{\bar{z}}^{-1} \partial_{\bar{y}} & \mu_{\bar{y}} + \partial_{\bar{x}} \epsilon_{\bar{z}}^{-1} \partial_{\bar{x}} \\ -\mu_{\bar{x}} - \partial_{\bar{y}} \epsilon_{\bar{z}}^{-1} \partial_{\bar{y}} & \partial_{\bar{y}} \epsilon_{\bar{z}}^{-1} \partial_{\bar{x}} \end{pmatrix} \begin{pmatrix} H_{\bar{x}} \\ H_{\bar{y}} \end{pmatrix}, \tag{2.14a}$$

$$\partial_{\bar{z}} \begin{pmatrix} H_{\bar{x}} \\ H_{\bar{y}} \end{pmatrix} = \pounds_{HE} \begin{pmatrix} E_{\bar{x}} \\ E_{\bar{y}} \end{pmatrix} = \begin{pmatrix} -\partial_{\bar{x}} \mu_{\bar{z}}^{-1} \partial_{\bar{y}} & \epsilon_{\bar{y}} + \partial_{\bar{x}} \mu_{\bar{z}}^{-1} \partial_{\bar{x}} \\ -\epsilon_{\bar{x}} - \partial_{\bar{y}} \mu_{\bar{z}}^{-1} \partial_{\bar{y}} & \partial_{\bar{y}} \mu_{\bar{z}}^{-1} \partial_{\bar{x}} \end{pmatrix} \begin{pmatrix} E_{\bar{x}} \\ E_{\bar{y}} \end{pmatrix}, \tag{2.14b}$$

where $\alpha_{\bar{x}} = \alpha_r g_y/g_x$, $\alpha_{\bar{y}} = \alpha_r g_x/g_y$ and $\alpha_{\bar{z}} = \alpha_r g_x g_y$, $\alpha = \mu, \epsilon$. Using Fourier series expansions for all the quantities in these equations, similar to the previous section, and employing Li's factorization rule as explained in Ref. [19], the following equations are derived for the layer eigenmodes in the transformed coordinate system:

$$\partial_{\bar{z}} \begin{pmatrix} \mathbf{S}_{\bar{x}} \\ \mathbf{S}_{\bar{y}} \end{pmatrix} = \mathbf{P} \begin{pmatrix} \mathbf{U}_{\bar{x}} \\ \mathbf{U}_{\bar{y}} \end{pmatrix} = \begin{pmatrix} \mathbf{K}_{\bar{x}} \mathcal{E}_{\bar{z}}^{-1} \mathbf{K}_{\bar{y}} & \mathcal{M}_{\bar{y}} - \mathbf{K}_{\bar{x}} \mathcal{E}_{\bar{z}}^{-1} \mathbf{K}_{\bar{x}} \\ \mathbf{K}_{\bar{y}} \mathcal{E}_{\bar{z}}^{-1} \mathbf{K}_{\bar{y}} - \mathcal{M}_{\bar{x}} & -\mathbf{K}_{\bar{y}} \mathcal{E}_{\bar{z}}^{-1} \mathbf{K}_{\bar{x}} \end{pmatrix} \begin{pmatrix} \mathbf{U}_{\bar{x}} \\ \mathbf{U}_{\bar{y}} \end{pmatrix}, \tag{2.15a}$$

$$\partial_{\bar{z}} \begin{pmatrix} \mathbf{U}_{\bar{x}} \\ \mathbf{U}_{\bar{y}} \end{pmatrix} = \mathbf{Q} \begin{pmatrix} \mathbf{S}_{\bar{x}} \\ \mathbf{S}_{\bar{y}} \end{pmatrix} = \begin{pmatrix} \mathbf{K}_{\bar{x}} \mathcal{M}_{\bar{z}}^{-1} \mathbf{K}_{\bar{y}} & \mathcal{E}_{\bar{y}} - \mathbf{K}_{\bar{x}} \mathcal{M}_{\bar{z}}^{-1} \mathbf{K}_{\bar{x}} \\ \mathbf{K}_{\bar{y}} \mathcal{M}_{\bar{z}}^{-1} \mathbf{K}_{\bar{y}} - \mathcal{E}_{\bar{x}} & -\mathbf{K}_{\bar{y}} \mathcal{M}_{\bar{z}}^{-1} \mathbf{K}_{\bar{x}} \end{pmatrix} \begin{pmatrix} \mathbf{S}_{\bar{x}} \\ \mathbf{S}_{\bar{y}} \end{pmatrix}, \tag{2.15b}$$

where $\mathbf{K}_i$, $i = \bar{x}, \bar{y}$ are diagonal matrices made of spatial wavevectors in the transformed coordinate system. $\mathcal{E}_i$ and $\mathcal{M}_i$, $i = \bar{x}, \bar{y}, \bar{z}$ are the matrices defined based on the definitions in the previous sections for ϵ_r and μ_r but in the transformed coordinate system.

If the number of Fourier terms tends to infinity, the eigenvalues obtained from the transformed coordinate system will be the same as the original system. However, since only limited number of Fourier terms are used in numerical simulations, in general the eigenvalues will be different in the two coordinate systems [20]. By increasing the number of harmonics, the eigenmodes in the original and transformed coordinate systems will converge toward the same solution, but their convergence path in complex eigenvalue plane can be different [20]. Figure 2.4 illustrates the largest eigenmode propagation constant for TE polarization ($\gamma_{1,TE}$) or TM polarization ($\gamma_{1,TM}$) as a function of M_x (N_y=1 and $N_t = M_x$), for three cases; using the simple eigenvalue, Eqs. (2.7), using Li's factorization, Eqs. (2.13), and using ASR technique, Eqs. (2.15). For the TE polarization, both the simple case

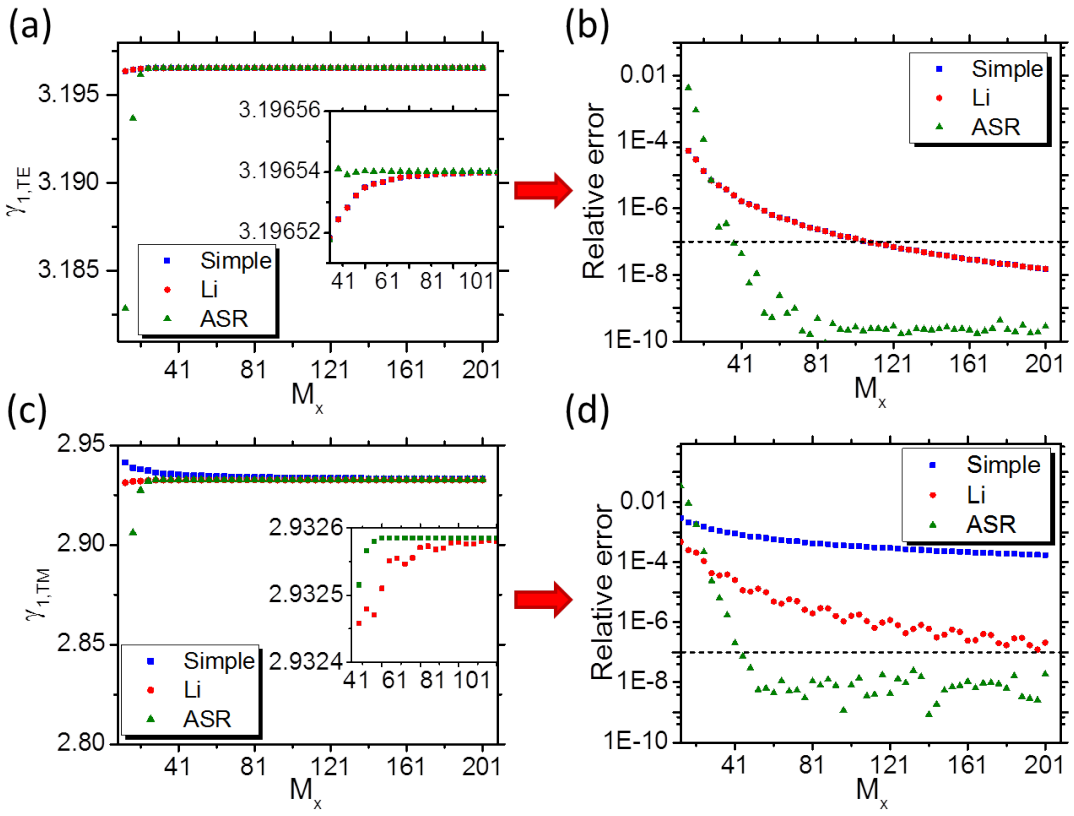

Figure 2.4: The largest eigenmode propagation constant of a grating layer for the (a) TE polarization $n_{1,TE}$, and (c) TM polarization $n_{1,TM}$, as a function of number of Fourier terms M_x. The insets show a zoomed-view of the graph. The relative errors for the (b) TE polarization, and (d) TM polarization are also illustrated. They are calculated with respect to the exact values, which are found for a very large number of Fourier terms, e.g. 301, and calculated as, $\gamma_{1,TE} = 2.93258522122416$ and $n\gamma_{1,TM} = 2.93258522122416$ for the TE and TM polarization, respectively. The dashed-lines specify a relative error of 10^{-7}. Refractive-indices in the grating layer are 3.48 and 1.48, and grating periodicity and duty cycle are 640 nm, 62%, respectively.

and the Li's case provide the same results, since Li's factorization rule is only employed in the TM polarization. The relative errors are calculated with respect to the exact values, which are found for a very large number of Fourier terms. The convergence rate is dramatically increased by employing the ASR technique in the both polarization (and particularly in the TM polarization) as shown in Fig. 2.4. For instance, for a relative error less than 10^{-7}, the number of Fourier terms M_x, should be at least 37 and 109 with or without employing the ASR technique in TE polarization, respectively. Similarly for the TM polarization, M_x should be larger than 45 or 220 with or without employing the ASR technique.

For a multilayer structure, there are two approaches to apply a coordinate transformation [21]. In the first method, for each layer a separate coordinate

transformation is used to find the eigenmodes of that layer. To match the boundary conditions between layer interfaces, a universal coordinate system should be used as the basis and all the eigenvectors should be projected to that basis [21]. This method can provide a good convergence for the eigenvalues of each layer, since each layer has its own transformation. Unfortunately, it was shown that this method is not efficient numerically and also the matrices involved are ill-conditioned when the back transformation is done [21]. In the second method, a common coordinate system is used for all the layers, and the jump points are composed of all jump points in all layers. As long as the number of distinct jump points is not large, this method can be used with sufficient accuracy and without any numerical problem [21], [22].

For a homogeneous layer in the structure, as it will be shown later, an exact analytic solution can be obtained for eigenvalues and eigenvectors in the original coordinate system. However, the eigenvalues in the transformed coordinate system will be different and represent an approximation of the exact analytic solutions. Therefore, in problems containing homogeneous layers, introducing the ASR may bring about less accurate results, since the improved accuracy obtained by the ASR for non-homogeneous layers, may be lost by the loss of accuracy in homogeneous ones [20].

In summary, the ASR technique provide a huge numerical advantage, in the cases where either a very accurate calculations are required or a layer permittivity possesses a large refractive-index contrast, e.g. contains both metal and dielectric materials [23], [24]. However, since we are interested in simulating vertical cavity structures with no metal in this thesis and accuracy on the order of 1%, the ASR does not bring any advantages for our computational problems. Although, the ASR technique is implemented, if not stated otherwise, it is not employed for the numerical calculations in this dissertation.

Absorbing Boundary Conditions

Similar to other numerical techniques for solving Maxwell's equations, such as finite-difference time-domain (FDTD) or finite element method (FEM), in order to prevent numerical artifacts coming from finite simulation domain, some sort of absorbing boundary conditions are required for the FMM. In the FMM, the first and last media are infinitely long and the field is incident to the structure. Thus, outgoing boundary condition is automatically satisfied in the z-direction. In the x- and y-directions, periodic boundary conditions are implemented naturally, since a periodic basis set is utilized in Fourier series. Therefore, if a structure is simulated in the FMM, in reality it corresponds to a simulation of an array of structures as

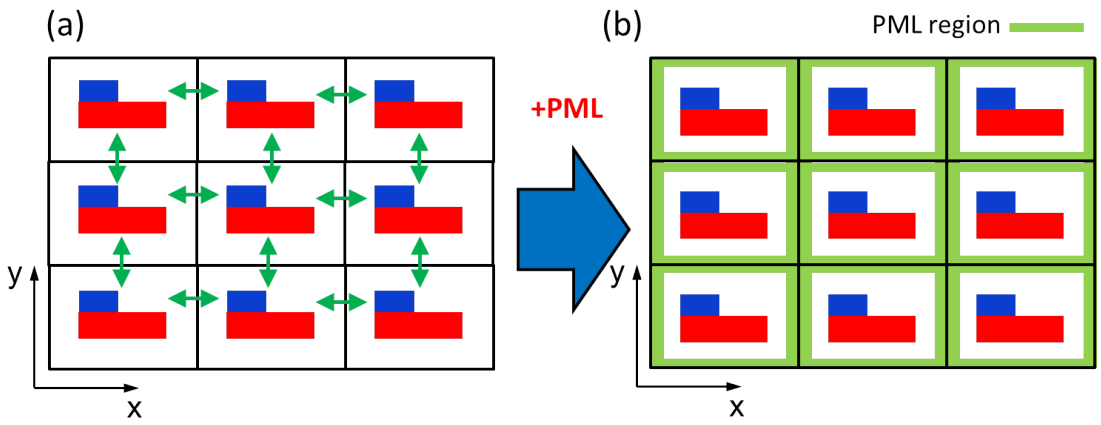

Figure 2.5: (a) Example of layer cross-section permittivity with artificial periodicity, due to the use of periodic boundary conditions in the FMM. The interactions between the neighboring unit cells are indicated by the green arrows. (b) The PML reduces the interactions between the neighboring unit cells.

shown schematically in Fig. 2.5(a) [25]. In order to reduce the neighboring cell effect, we may use a very large unit cell, which is referred to as the super-cell technique [26]. However, it results in increasing the required number of Fourier terms and reducing the numerical efficiency of the FMM [26]. A more effective approach is possible by utilizing absorbing boundary condition, which is implemented as a region surrounding the structure as illustrated in Fig. 2.5(b). Initially, a simple gradient-index absorber was used for this region [27]. Later, more sophisticated absorbers called perfectly matched layer (PML) composed of magnetic and isotropic materials were used, which could absorb the outgoing waves more efficiently [28]. The concept of PML also may also be implemented as a complex coordinate stretching (which is a kind of coordinate transformation) similar to the implementation in the FDTD technique [29]. A complex coordinate stretching was implemented in the FMM, which demonstrates promising results [30], and it is also employed in this section.

Using coordinate stretching functions g_x and g_y for the x- and y-directions, respectively, modifies the differential field operators of Eqs. (2.4) [25], [26]:

$$\pounds_{EH} = \begin{pmatrix} -f_x\partial_x\epsilon_r^{-1}f_y\partial_y & \mu_r + f_x\partial_x\epsilon_r^{-1}f_x\partial_x \\ -\mu_r - f_y\partial_y\epsilon_r^{-1}f_y\partial_y & f_y\partial_y\epsilon_r^{-1}f_x\partial_x \end{pmatrix}, \tag{2.16a}$$

$$\pounds_{HE} = \begin{pmatrix} -f_x\partial_x\mu_r^{-1}f_y\partial_y & \epsilon_r + f_x\partial_x\mu_r^{-1}f_x\partial_x \\ -\epsilon_r - f_y\partial_y\mu_r^{-1}f_y\partial_y & f_y\partial_y\mu_r^{-1}f_x\partial_x \end{pmatrix}, \tag{2.16b}$$

where $f_x = (\partial g_x/\partial x)^{-1}$ and $f_y = (\partial g_y/\partial y)^{-1}$. The coordinate stretching functions should possess several properties. They are unity transformations outside the PMLs, i.e. $g_x = x$ and $g_y = y$, respectively. Inside the PMLs, the coordinate

stretching functions are complex-value functions, since the imaginary part of the transformation damps the propagating waves inside the PMLs. In the FMM, the following coordinate stretching function is suggested [30]:

$$g_x(x) = \begin{cases} x & \text{if } |x| < d_x \\ \dfrac{x}{|x|}\left(d_x + \dfrac{t_{a,x}}{\pi(1-\gamma)}\left[b_x - \dfrac{\gamma}{\sqrt{1-\gamma}}\arctan\left(\sqrt{1-\gamma}b_x\right)\right]\right) & \text{if } |x| > d_x, \end{cases} \tag{2.17}$$

where $t_{a,x}$ is the PML thickness, $b_x = \tan(\alpha_x)$, $\alpha_x = \pi(|x|-d_x)/t_{a,x}$, $d_x = \Lambda_x/2 - t_{a,x}$ and γ is a complex constant, and equals to $(1+j)/2$ [30]. A similar expression is used for the coordinate stretching function g_y. If not stated otherwise, $t_{a,x} = t_{a,y}$ are chosen to be 0.5 μm.

The differential equations (2.16) can be represented in matrix form by using the Fourier expansion techniques. This will result in similar expressions as Eqs. (2.13), except replacing $\mathbf{K}_x$ and $\mathbf{K}_y$ with $\mathbf{F}_x\mathbf{K}_x$ and $\mathbf{F}_y\mathbf{K}_y$, respectively, where $\mathbf{F}_x$ and $\mathbf{F}_y$ are the Toeplitz matrices defined from the Fourier series coefficient of the functions f_x and f_y, respectively [25]. As an example, to illustrate the importance of the PML implementation, a slab waveguide which is simply terminated with air is considered and the modal reflectivity of the fundamental TE mode ($R_{TE,0}$) is calculated with or without PML implementation. Figure 2.6(a) illustrates the value of the modal reflectivity versus the total number of Fourier terms for two different computational domain width Λ_x, with or without the PML implementation. Without the PML implementation, the value of the modal reflectivity is totally different for the two Λ_x. The value of the modal reflectivity as a function of Λ_x is shown in Fig. 2.6(b), with or without the PML implementation for a sufficiently large number of Fourier terms. Without the PML implementation, the value of $R_{TE,0}$ oscillates around the correct value, while with the PML implementation, there is no oscillation. This oscillation behavior is a sign of interference between nearby cells and can be observed clearly in the field profile of Fig. 2.6(c). Figure 2.6(d) demonstrates clearly that the PML effectively eliminates unwanted interference from the neighboring cells.

It is possible to combine the coordinate transformation of the ASR technique and the complex coordinate stretching of the PML technique. Considering both of these techniques, the expressions for matrices $\mathbf{P}$ and $\mathbf{Q}$ become:

$$\mathbf{P} = \begin{pmatrix} \mathbf{F}_{\bar{x}}\mathbf{K}_{\bar{x}}\mathcal{E}_{\bar{z}}^{-1}\mathbf{F}_{\bar{y}}\mathbf{K}_{\bar{y}} & \mathcal{M}_{\bar{y}} - \mathbf{F}_{\bar{x}}\mathbf{K}_{\bar{x}}\mathcal{E}_{\bar{z}}^{-1}\mathbf{F}_{\bar{x}}\mathbf{K}_{\bar{x}} \\ \mathbf{F}_{\bar{y}}\mathbf{K}_{\bar{y}}\mathcal{E}_{\bar{z}}^{-1}\mathbf{F}_{\bar{y}}\mathbf{K}_{\bar{y}} - \mathcal{M}_{\bar{x}} & -\mathbf{F}_{\bar{y}}\mathbf{K}_{\bar{y}}\mathcal{E}_{\bar{z}}^{-1}\mathbf{F}_{\bar{x}}\mathbf{K}_{\bar{x}} \end{pmatrix}, \tag{2.18a}$$

$$\mathbf{Q} = \begin{pmatrix} \mathbf{F}_{\bar{x}}\mathbf{K}_{\bar{x}}\mathcal{M}_{\bar{z}}^{-1}\mathbf{F}_{\bar{y}}\mathbf{K}_{\bar{y}} & \mathcal{E}_{\bar{y}} - \mathbf{F}_{\bar{x}}\mathbf{K}_{\bar{x}}\mathcal{M}_{\bar{z}}^{-1}\mathbf{F}_{\bar{x}}\mathbf{K}_{\bar{x}} \\ \mathbf{F}_{\bar{y}}\mathbf{K}_{\bar{y}}\mathcal{M}_{\bar{z}}^{-1}\mathbf{F}_{\bar{y}}\mathbf{K}_{\bar{y}} - \mathcal{E}_{\bar{x}} & -\mathbf{F}_{\bar{y}}\mathbf{K}_{\bar{y}}\mathcal{M}_{\bar{z}}^{-1}\mathbf{F}_{\bar{x}}\mathbf{K}_{\bar{x}} \end{pmatrix}. \tag{2.18b}$$

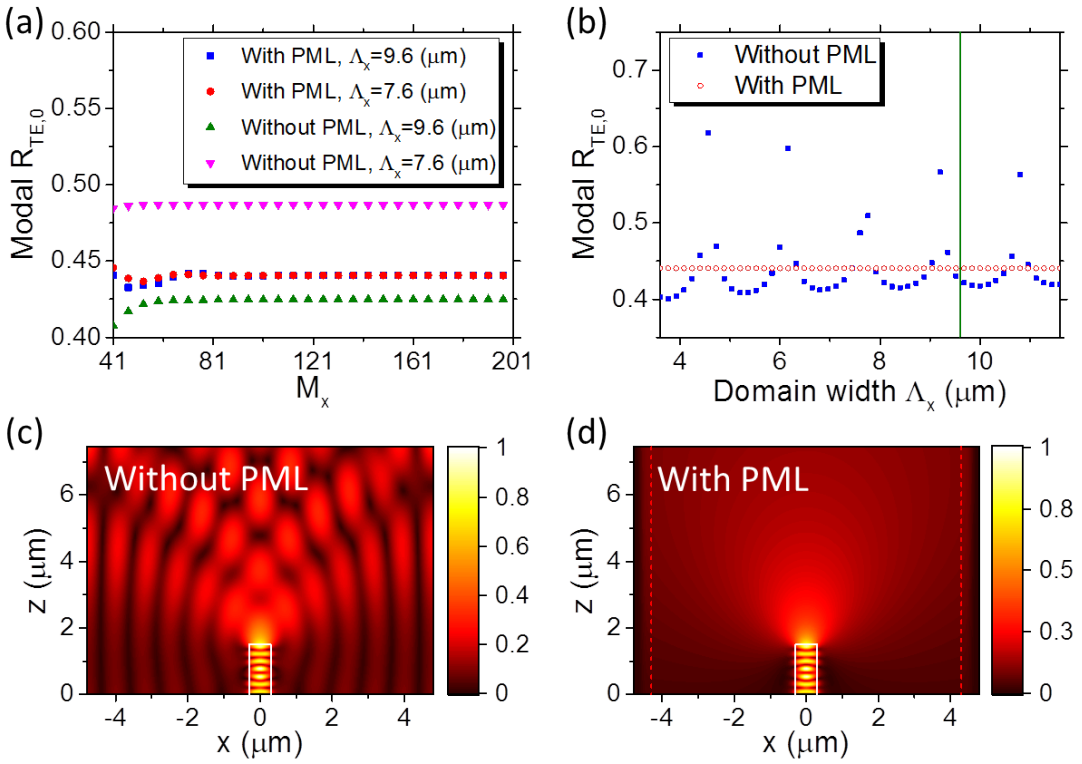

Figure 2.6: The modal reflectivity of the fundamental TE mode $R_{TE,0}$ of a 0.6μm-width silicon slab waveguide at 1550 nm wavelength, terminated with air as a function of (a) total number of Fourier terms M_x, or (b) domain width Λ_x. The value of $R_{TE,0}$ varies by changing the Λ_x when there is no PML. (c), (d) Normalized field profile E_y of the slab waveguide at 9.6 μm domain width [which is shown in (a) with green line] and for M_x=301, (c) without the PML, or (d) with the PML. The boundaries of the waveguide layer and PMLs are shown in white solid-lines and red dashed-lines, respectively. The PML effectively eliminates unwanted interference from the neighboring cells in (d).

Structural Symmetries

Similar to other numerical techniques, solving Maxwell's equations for a 3D structure is numerically cumbersome and a time-consuming problem. Therefore, any attempt to reduce the computational effort is important and well-appreciated such as considering the symmetries of the problem. In Maxwell's equations, if the permittivity function is an even function of the coordinate system, the solution will be either even or odd [2]. Considering only the mirror symmetries for the permittivity function in the transverse directions, four cases are possible; no symmetry, x-axis mirror-reflection symmetry, y-axis mirror-reflection symmetry and simultaneous x- and y-axis mirror-reflection symmetries. In the FMM, the mirror symmetries in the real space can be transferred to the Fourier space [31]. If the total number of Fourier terms are M_x and N_y in the x- and y-directions, respectively, the size of eigenvalue problem will be $2M_xN_y$ and the total number of elements for each matrix

(such as $\mathbf{S}_{ij}$, $\mathbf{P}$ and $\mathbf{Q}$) will be $(2M_xN_y)^2$. If the structure has a mirror-reflection symmetry in the both transverse directions, the matrix size will be reduced to one-fourth. Since, the eigenvalue calculation time is roughly proportional to the third power of the matrix size, using two mirror structural symmetries results in a factor of $4^3 = 64$ reduction of the calculation time. Moreover, the total number of matrix elements will be reduced by a factor of $4^2 = 16$. The method, which is explained thoroughly in Refs. [31], [32], is implemented here to take advantage of the mirror-reflection symmetries.

Two-Dimensional Limit

If the structure is invariant in one direction, for instance in the y-direction and the incident wavevector is in the coordinate plane, i.e. $k_{y0} = 0$, the 3D problem can be simplified to two individual 2D problems for the TE and TM polarizations. For the TE polarization, the non-zero field components are (E_y, H_x, H_z), while for the TM polarization only (E_x, E_z, H_y) are the non-zero terms. The matrix size for a 2D problem is reduced to half, which results in an eight-times and four-times reduction of computational time and required memory, respectively. The expressions for the $\mathbf{P}$ and $\mathbf{Q}$ matrices for the two polarizations can be obtained simply by letting $\mathbf{K}_{\bar{y}} = \mathbf{O}$ and $\mathcal{M}_{\bar{y}} = \mathbf{I}$:

$$\mathbf{\Omega} = \mathbf{PQ} = \begin{pmatrix} \mathbf{\Omega_{11}} & \mathbf{O} \\ \mathbf{O} & \mathbf{\Omega_{22}} \end{pmatrix}, \tag{2.19a}$$

$$TM : \mathbf{\Omega_{11}} = (\mathbf{F}_{\bar{x}}\mathbf{K}_{\bar{x}}\mathcal{E}_{\bar{z}}^{-1}\mathbf{F}_{\bar{x}}\mathbf{K}_{\bar{x}} - \mathbf{I})\mathcal{E}_{\bar{x}}, \tag{2.19b}$$

$$TE : \mathbf{\Omega_{22}} = \mathcal{M}_{\bar{x}}(\mathbf{F}_{\bar{x}}\mathbf{K}_{\bar{x}}\mathcal{M}_{\bar{z}}^{-1}\mathbf{F}_{\bar{x}}\mathbf{K}_{\bar{x}} - \mathcal{E}_{\bar{y}}). \tag{2.19c}$$

Since $\mathbf{\Omega}$ is a block diagonal matrix, its eigenvalues are a combination of the eigenvalues of its block matrices $\mathbf{\Omega}_{11}$ and $\mathbf{\Omega}_{22}$, which correspond to the TM and TE polarization problems, respectively. Without the PML implementation and any coordinate transformation for the ASR technique, these expressions will be similar to the expressions derived in Refs. [8], [33]. However, the eigenvalue problem for the TM polarization is found based on the electric field E_x here (instead of the magnetic field H_y).

Homogeneous Layer Eigenmodes

For a homogeneous layer, i.e. a layer with no spatial variation of the relative permittivity function, the eigenmodes of the layer may be obtained analytically. Without the PML implementation and ASR technique, the eigenmodes correspond

to the Rayleigh expansions for diffraction orders [13]. For a homogeneous layer with a permittivity value of ϵ_r, it is easy to show that $\mathcal{E}_x = \mathcal{E}_y = \mathcal{E}_z = \epsilon_r \mathbf{I}$ and as a result $\mathbf{P} = 1/\epsilon_r \mathbf{Q}$ using Eqs. 2.13, the eigenvalue problem will be for matrix $\mathbf{\Omega}$

$$\mathbf{\Omega} = \begin{pmatrix} \mathbf{K}_x^2 + \mathbf{K}_y^2 - \epsilon_r \mathbf{I} & \mathbf{O} \\ \mathbf{O} & \mathbf{K}_x^2 + \mathbf{K}_y^2 - \epsilon_r \mathbf{I} \end{pmatrix} = \begin{pmatrix} -\mathbf{K}_z^2 & \mathbf{O} \\ \mathbf{O} & -\mathbf{K}_z^2 \end{pmatrix}. \tag{2.20}$$

where $\mathbf{K}_z$ is a matrix with elements $k_{z,mn} = \left(\sqrt{\epsilon_r - k_{xm}^2 - k_{yn}^2}\right)^*$. Since it is a diagonal matrix, its eigenvalues are equal to the diagonal elements $\gamma_{mn} = jk_{z,mn}$ and its eigenvectors form an identity matrix $\mathbf{W} = \mathbf{I}$.

If the PML is implemented or the ASR technique is used (or both of them), the eigenmodes can not be found analytically anymore. However, if there are several homogeneous layers, a simple relationship can be found between their eigenmodes [34]. Assume the eigenvalue problem is solved for free-space and its matrices for the eigenmode electric field and propagation constant are $\mathbf{W}_0$ and $\mathbf{\Gamma}_0$, respectively. As it is derived in Appendix A, the eigenvalue problem for determining the eigenmodes of layer with permittivity of ϵ_r has a solution of ($\mathbf{W}$, $\mathbf{\Gamma}$), where:

$$\mathbf{W} = \mathbf{W_0}, \tag{2.21a}$$

$$\mathbf{\Gamma}^2 = \mathbf{\Gamma}_0^2 + (1 - \epsilon_r)\mathbf{I}. \tag{2.21b}$$

2.2.3 Scattering Matrices

In order to connect the field in the neighboring layers, the continuity of traverse field components, i.e. E_x, E_y, H_x and E_y, at the layer interfaces should be applied. It results in a linear relationship between the field coefficients, $\mathbf{c}_p$ and $\mathbf{c}_n$ in two neighboring layers. In a multilayer structure, various algorithms can be used to connect the coefficients, such as transfer matrices [35], hybrid matrices [36], admittance matrices [37], and scattering matrices [4], [7], [38]. Among them, the scattering matrices (S-matrices) method is a powerful tool which is used widely in the literature, due to various advantages such as elegant physical interpretations, unconditional stability and memory efficiency [4].

There are several variants of S-matrix implementation for the FMM [4], [7]. In the variant implemented in this thesis, all the layers are separated by a gap composed of free-space [4], [38]. As long as the free-space gap thickness is zero, it has no influence on the performance of the structure. The advantage of using the artificial free-space regions, is that the S-matrices of each layer only depends on the layer itself, not on its adjacent layers [4], [38]. It reduces the numerical effort for the cases where only one layer is changing, since only the S-matrices of that layer should be updated instead of all adjacent layers. Here, the expressions used for each layer S-matrices and also a mulitilayer structure in this variant of S-matrices are reviewed.

Scattering Matrices of a Single Layer

As it was explained in the previous section, the field in layer q is:

$$\begin{pmatrix}\mathbf{S}_x^{(q)}\\ \mathbf{S}_y^{(q)}\end{pmatrix} = +\mathbf{W}_q \exp\left[-\mathbf{\Gamma}_q(z-z_1^{(q)})\right]\mathbf{c}_p^{(q)} + \mathbf{W}_q \exp\left[+\mathbf{\Gamma}_q(z-z_2^{(q)})\right]\mathbf{c}_n^{(q)}, \tag{2.22a}$$

$$\begin{pmatrix}\mathbf{U}_x^{(q)}\\ \mathbf{U}_y^{(q)}\end{pmatrix} = -\mathbf{V}_q \exp\left[-\mathbf{\Gamma}_q(z-z_1^{(q)})\right]\mathbf{c}_p^{(q)} + \mathbf{V}_q \exp\left[+\mathbf{\Gamma}_q(z-z_2^{(q)})\right]\mathbf{c}_n^{(q)}, \tag{2.22b}$$

where $\mathbf{c}_p^{(q)}$ and $\mathbf{c}_n^{(q)}$ are defined at the left and right interfaces of layer q, respectively. If the layer q is sandwiched between two layers, denoted by layer 1 and 2, the continuity of the transverse field components at the interfaces will be written as:

$$\begin{pmatrix}\hat{\mathbf{W}}_1 & \hat{\mathbf{W}}_1\\ -\hat{\mathbf{V}}_1 & \hat{\mathbf{V}}_1\end{pmatrix}\begin{pmatrix}\hat{\mathbf{c}}_p^{(1)}\\ \hat{\mathbf{c}}_n^{(1)}\end{pmatrix} = \begin{pmatrix}\mathbf{W}_q & \mathbf{W}_q\\ -\mathbf{V}_q & \mathbf{V}_q\end{pmatrix}\begin{pmatrix}\mathbf{I} & \mathbf{O}\\ \mathbf{O} & \mathbf{X}_q\end{pmatrix}\begin{pmatrix}\mathbf{c}_p^{(q)}\\ \mathbf{c}_n^{(q)}\end{pmatrix}, \tag{2.23a}$$

$$\begin{pmatrix}\mathbf{W}_q & \mathbf{W}_q\\ -\mathbf{V}_q & \mathbf{V}_q\end{pmatrix}\begin{pmatrix}\mathbf{X}_q & \mathbf{O}\\ \mathbf{O} & \mathbf{I}\end{pmatrix}\begin{pmatrix}\mathbf{c}_p^{(q)}\\ \mathbf{c}_n^{(q)}\end{pmatrix} = \begin{pmatrix}\hat{\mathbf{W}}_2 & \hat{\mathbf{W}}_2\\ -\hat{\mathbf{V}}_2 & \hat{\mathbf{V}}_2\end{pmatrix}\begin{pmatrix}\hat{\mathbf{c}}_p^{(2)}\\ \hat{\mathbf{c}}_n^{(2)}\end{pmatrix}, \tag{2.23b}$$

where $\hat{\mathbf{c}}_p^{(1)}$, $\hat{\mathbf{c}}_n^{(1)}$, $\hat{\mathbf{c}}_p^{(2)}$, $\hat{\mathbf{c}}_n^{(2)}$ are free-space eigemode coefficients in the layer 1 and 2. $\mathbf{X}_q = \exp[-\mathbf{\Gamma}_q d_q]$ is the propagation matrix, and $\mathbf{W}$ and $\mathbf{V}$ are the eigenmodes matrices for the electric and magnetic fields, respectively, in the corresponding media. As mentioned earlier, each layer is sandwiched between two free-space regions of zero thickness, i.e. $\hat{\mathbf{W}}_1 = \hat{\mathbf{W}}_2 = \mathbf{W}_0$ and $\hat{\mathbf{V}}_1 = \hat{\mathbf{V}}_2 = \mathbf{V}_0$.

The S-matrices of layer q, $\mathbf{S}_{ij}^{(q)}$, are determined by connecting the coefficients in the left and right media as:

$$\begin{pmatrix}\hat{\mathbf{c}}_n^{(1)}\\ \hat{\mathbf{c}}_p^{(2)}\end{pmatrix} = \begin{pmatrix}\mathbf{S}_{11}^{(q)} & \mathbf{S}_{12}^{(q)}\\ \mathbf{S}_{21}^{(q)} & \mathbf{S}_{22}^{(q)}\end{pmatrix}\begin{pmatrix}\hat{\mathbf{c}}_p^{(1)}\\ \hat{\mathbf{c}}_n^{(2)}\end{pmatrix}. \tag{2.24}$$

In this form of definition, $\mathbf{S}_{11}^{(q)}$ and $\mathbf{S}_{22}^{(q)}$ represent the reflection from the left and right sides, respectively and $\mathbf{S}_{12}^{(q)}$ and $\mathbf{S}_{21}^{(q)}$ correspond to the transmission from left-to-right and right-to-left, respectively. After some algebra, the following expressions can be derived for the S-matrices [4]:

$$\mathbf{S}_{11}^{(q)} = \mathbf{S}_{22}^{(q)} = (\mathbf{A}_q - \mathbf{T}\mathbf{B}_q)^{-1}(\mathbf{T}\mathbf{A}_q - \mathbf{B}_q), \tag{2.25a}$$

$$\mathbf{S}_{12}^{(q)} = \mathbf{S}_{21}^{(q)} = (\mathbf{A}_q - \mathbf{T}\mathbf{B}_q)^{-1}\mathbf{X}_q(\mathbf{A}_q - \mathbf{B}_q\mathbf{A}_q^{-1}\mathbf{B}_q), \tag{2.25b}$$

where $\mathbf{A}_q = \mathbf{W}_q^{-1}\mathbf{W}_0 + \mathbf{V}_q^{-1}\mathbf{V}_0$, $\mathbf{B}_q = \mathbf{W}_q^{-1}\mathbf{W}_0 - \mathbf{V}_q^{-1}\mathbf{V}_0$ and $\mathbf{T} = \mathbf{X}_q\mathbf{B}_q\mathbf{A}_q^{-1}\mathbf{X}_q$ are auxiliary matrices. Since the layer is sandwiched between two similar free-space regions and the permittivity function does not vary in the z-direction, it has a mirror-reflection symmetry in the z-direction and its S-matrices are also symmetric.

There are two special layers in the FMM formulation, the first and the last layer which are infinitely long layers. For these layers, the S-matrices can be obtained by assuming a zero-thickness layer q. For the first layer (reflection region), the following expressions are obtained for the S-matrices [4]:

$$\mathbf{S}_{11}^{(ref)} = -\mathbf{A}_{ref}^{-1}\mathbf{B}_{ref}, \tag{2.26a}$$
$$\mathbf{S}_{12}^{(ref)} = 2\mathbf{A}_{ref}^{-1}, \tag{2.26b}$$
$$\mathbf{S}_{21}^{(ref)} = 0.5(\mathbf{A}_{ref} - \mathbf{B}_{ref}\mathbf{A}_{ref}^{-1}\mathbf{B}_{ref}), \tag{2.26c}$$
$$\mathbf{S}_{22}^{(ref)} = \mathbf{B}_{ref}\mathbf{A}_{ref}^{-1}, \tag{2.26d}$$

where $\mathbf{A}_{ref} = \mathbf{W}_0^{-1}\mathbf{W}_{ref} + \mathbf{V}_0^{-1}\mathbf{V}_{ref}$ and $\mathbf{B}_{ref} = \mathbf{W}_0^{-1}\mathbf{W}_{ref} - \mathbf{V}_0^{-1}\mathbf{V}_{ref}$ are auxiliary matrices. Similarly, for the last layer (transmission region), the S-matrices can be obtained by replacing $(ref) \rightarrow (trn)$, $1 \rightarrow 2$ and $2 \rightarrow 1$ in Eqs. (2.26).

Scattering Matrices of a Multilayer Structure

For a multilayer structure, the S-matrices of all layers should be combined using the well-known Redheffer star product [7]. Assuming two sets of S-matrices denoted by $\mathbf{S}^A$ and $\mathbf{S}^B$, their Redheffer star product, denoted by $\mathbf{S}^{AB} = \mathbf{S}^A \otimes \mathbf{S}^B$, becomes:

$$\mathbf{S}_{11}^{(AB)} = \mathbf{S}_{11}^{(A)} + \mathbf{S}_{12}^{(A)}\left[\mathbf{I} - \mathbf{S}_{11}^{(B)}\mathbf{S}_{22}^{(A)}\right]^{-1}\mathbf{S}_{11}^{(B)}\mathbf{S}_{21}^{(A)}, \tag{2.27a}$$
$$\mathbf{S}_{12}^{(AB)} = \mathbf{S}_{12}^{(A)}\left[\mathbf{I} - \mathbf{S}_{11}^{(B)}\mathbf{S}_{22}^{(A)}\right]^{-1}\mathbf{S}_{12}^{(B)}, \tag{2.27b}$$
$$\mathbf{S}_{21}^{(AB)} = \mathbf{S}_{21}^{(B)}\left[\mathbf{I} - \mathbf{S}_{22}^{(A)}\mathbf{S}_{11}^{(B)}\right]^{-1}\mathbf{S}_{21}^{(A)}, \tag{2.27c}$$
$$\mathbf{S}_{22}^{(AB)} = \mathbf{S}_{22}^{(B)} + \mathbf{S}_{21}^{(B)}\left[\mathbf{I} - \mathbf{S}_{22}^{(A)}\mathbf{S}_{11}^{(B)}\right]^{-1}\mathbf{S}_{22}^{(A)}\mathbf{S}_{12}^{(B)}. \tag{2.27d}$$

There are other variants of these expressions which may be more efficient in the cases where only some of the S-matrices are required as provided in Appendix B.

To determine the S-matrices of a multilayer structure, beginning from the last layer, the S-matrices will be updated by adding layers one by one to the first layer [7]. The S-matrices of the structure seen from free-space region between layers toward the last layer is denoted as $\mathbf{S}_t^{(q)}$, as shown in Fig. 2.7. Using a recursive algorithm toward the first layer, all S-matrices seen from free-space regions are determined as:

$$\mathbf{S}_t^{(0)} = \mathbf{S}^{(trn)}, \tag{2.28a}$$
$$\mathbf{S}_t^{(q)} = \mathbf{S}^{(N-q+1)} \otimes \mathbf{S}_t^{(q-1)}, \tag{2.28b}$$
$$\mathbf{S}_t^{(N+1)} = \mathbf{S}^{(ref)} \otimes \mathbf{S}_t^{(N)}, \tag{2.28c}$$

where the index q changes from 1 to N. For periodic structures in the z-direction, there is a fast algorithm for computing S-matrices, which is referred to as the doubling algorithm [4], [39].

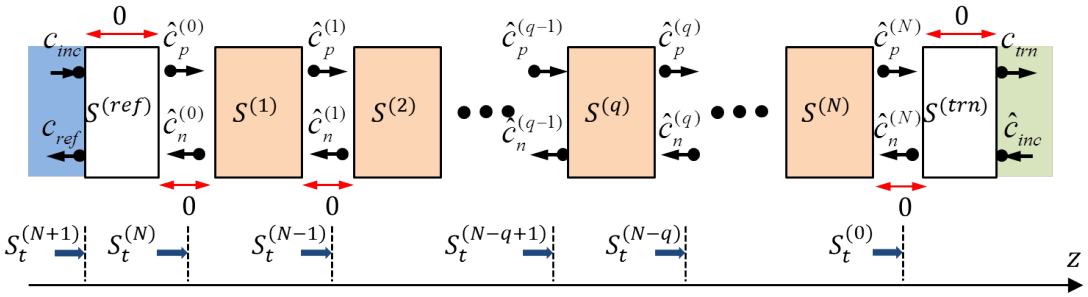

Figure 2.7: Schematic of a multilayer structure and the S-matrix definitions.

2.2.4 Dispersion Calculation

For a periodic structure, the dispersion graph, which is the relation between the mode frequency ω and wavevector $\tilde{\mathbf{k}}$, provides valuable information about the electromagnetic properties of the structure. In the FMM, for the longitudinal direction z, it is possible to compute the dispersion using the S-matrices [4], [40], [41]. The S-matrices of a unit cell of the periodic structure is denoted by $\mathbf{S}^{(uc)}$:

$$\begin{pmatrix} \hat{\mathbf{c}}_n^{(1)} \\ \hat{\mathbf{c}}_p^{(2)} \end{pmatrix} = \begin{pmatrix} \mathbf{S}_{11}^{(uc)} & \mathbf{S}_{12}^{(uc)} \\ \mathbf{S}_{21}^{(uc)} & \mathbf{S}_{22}^{(uc)} \end{pmatrix} \begin{pmatrix} \hat{\mathbf{c}}_p^{(1)} \\ \hat{\mathbf{c}}_n^{(2)} \end{pmatrix}, \tag{2.29}$$

where the $\hat{\mathbf{c}}_p^{(i)}$ and $\hat{\mathbf{c}}_n^{(i)}$ i =1,2 are the eigenmodes coefficients in the neighboring free-space regions. By rearranging this equation in the form of transfer matrix, and using Bloch's theory for a mode propagating through a unit cell, the following equation is obtained [4]:

$$\begin{pmatrix} \mathbf{O} & -\mathbf{S}_{12}^{(uc)} \\ \mathbf{I} & -\mathbf{S}_{22}^{(uc)} \end{pmatrix} \begin{pmatrix} \hat{\mathbf{c}}_p^{(1)} \\ \hat{\mathbf{c}}_n^{(1)} \end{pmatrix} = \exp\left(j\beta\Lambda_z\right) \begin{pmatrix} \mathbf{S}_{11}^{(uc)} & -\mathbf{I} \\ \mathbf{S}_{21}^{(uc)} & \mathbf{O} \end{pmatrix} \begin{pmatrix} \hat{\mathbf{c}}_p^{(1)} \\ \hat{\mathbf{c}}_n^{(1)} \end{pmatrix}, \tag{2.30}$$

where β is the Bloch's mode propagation constant and the structure is periodic in the z-direction with periodicity of Λ_z.

Equation 2.30 is a generalized eigenvalue problem in the form of $\mathbf{Ax} = \lambda\mathbf{Bx}$, where the eigenvalues λ are the Bloch's mode propagation constants. Due to the two possible propagation directions for the Bloch's modes, λ can be divided into two groups of λ_+ and λ_- with the relationship of $\lambda_- = 1/\lambda_+$ [42]. In the numerical implementation, when the number of Fourier terms is increased, this equation is not satisfied for some of the non-propagating Bloch's modes due to the numerical overflow [42]. To handle this problem, the equivalent eigenvalue problem of $\mathbf{Bx} = (\lambda + 1)^{-1}(\mathbf{A} + \mathbf{B})\mathbf{x}$ is solved [42].

2.2.5 Field Calculation

The eigenmode coefficients in all layers, i.e. $\mathbf{c}_p^{(q)}$ and $\mathbf{c}_n^{(q)}$, are required for computing the field profile. It is assumed that $\mathbf{c}_{inc}$ and $\hat{\mathbf{c}}_{inc}$ are given, all the layer S-matrices $\mathbf{S}^{(q)}$ and the total S-matrices $\mathbf{S}_t^{(q)}$ are available. Determining $\mathbf{c}_p^{(q)}$ and $\mathbf{c}_n^{(q)}$ consists of two steps. Firstly, the eigenmode coefficients in free-space regions surrounding the layers, i.e. $\hat{\mathbf{c}}_p^{(q)}$ and $\hat{\mathbf{c}}_n^{(q)}$, are determined by a recursive algorithm. Secondly, using the free-space region coefficients, the eignemode coefficients in each layer will be obtained.

For the first free-space region, the following expressions are obtained for $\hat{\mathbf{c}}_p^{(0)}$ and $\hat{\mathbf{c}}_n^{(0)}$:

$$\hat{\mathbf{c}}_p^{(0)} = \left[\mathbf{I} - \mathbf{S}_{22}^{(ref)}\mathbf{S}_{t,11}^{(N)}\right]^{-1}\left[\mathbf{S}_{21}^{(ref)}\mathbf{c}_{inc} + \mathbf{S}_{22}^{(ref)}\mathbf{S}_{t,12}^{(N)}\hat{\mathbf{c}}_{inc}\right], \tag{2.31a}$$

$$\hat{\mathbf{c}}_n^{(0)} = \mathbf{S}_{t,11}^{(N)}\hat{\mathbf{c}}_p^{(0)} + \mathbf{S}_{t,12}^{(N)}\hat{\mathbf{c}}_{inc}. \tag{2.31b}$$

Similarly, if the eigenmode coefficients are known for free-space region $q-1$, the coefficients for the next free-space region q, become:

$$\hat{\mathbf{c}}_p^{(q)} = \left[\mathbf{I} - \mathbf{S}_{22}^{(q)}\mathbf{S}_{t,11}^{(N-q)}\right]^{-1}\left[\mathbf{S}_{21}^{(q)}\hat{\mathbf{c}}_p^{(q-1)} + \mathbf{S}_{22}^{(q)}\mathbf{S}_{t,12}^{(N-q)}\hat{\mathbf{c}}_{inc}\right] \tag{2.32a}$$

$$\hat{\mathbf{c}}_n^{(q)} = \mathbf{S}_{t,11}^{(N-q)}\hat{\mathbf{c}}_p^{(q)} + \mathbf{S}_{t,12}^{(N-q)}\hat{\mathbf{c}}_{inc} \tag{2.32b}$$

Therefore, by applying a recursive algorithm and starting from $q = 1$, the eigenmode coefficients are determined for all free-space regions. It should be mentioned that usually, the excitation is performed from one direction (e.g. from the left side in Fig. 2.7), i.e. $\hat{\mathbf{c}}_{inc} = \mathbf{O}$ and these expression are simplified.

If the eigenmode coefficients for free-space regions surrounding the layer q are known, the eigemode coefficients in the layer q are determined easily using Eqs. (2.23) as:

$$\mathbf{c}_p^{(q)} = \frac{1}{2}\mathbf{A}_q\hat{\mathbf{c}}_p^{(q-1)} + \frac{1}{2}\mathbf{B}_q\hat{\mathbf{c}}_n^{(q-1)}, \tag{2.33a}$$

$$\mathbf{c}_n^{(q)} = \frac{1}{2}\mathbf{A}_q\hat{\mathbf{c}}_p^{(q)} + \frac{1}{2}\mathbf{B}_q\hat{\mathbf{c}}_n^{(q)}, \tag{2.33b}$$

in which $\mathbf{A}_q$ and $\mathbf{B}_q$ matrices are defined previously. After determining the mode coefficients, the electric and magnetic fields in the layer will be computed by using Eqs. (2.6).

2.2.6 Resonance Wavelength and Quality-Factor

The most important characteristics of a resonant optical cavity, are the resonance wavelengths λ_r of the modes and their quality-factor (Q-factor) Q. In this section, several methods, used for finding the resonance wavelengths and Q-factor of a resonant optical cavity in the FMM, are explained and compared. The advantages and disadvantages of these methods are also discussed briefly. A 2D HCG-based vertical cavity [illustrated in Fig. 2.3(b)] is used as a test structure to compare the numerical results obtained from these methods. However, these approaches are also applicable to the other types of resonant optical cavity.

Method I: Quasi-Normal Mode with Complex Frequency

Since optical cavities are open systems, which means they are leaky, the Maxwell's equation eigenmodes have complex frequencies [43]. These eigenmodes are referred to as quasi-normal modes (QNMs). Using the concept of QNM provides a convenient framework for working with optical cavities, since the complex QNM eigenvalues correspond to the position and Q-factor of the resonances in the spectral transmissivity [44]. In the QNM picture, the optical cavity is viewed as a passive open system with only emission out of the cavity and no waves incident to the cavity. Therefore, outgoing boundary conditions should be satisfied for the QNM. In the FMM, the outgoing boundary condition is satisfied in the z-direction as already discussed in the previous sections. Using the scattering matrices concept, a QNM can be found as the non-trivial solution of the following equation by letting $\mathbf{c}_{in}$ go to zero [45]:

$$\mathbf{c}_{out} = \mathbf{S}_t \mathbf{c}_{in} \quad \rightarrow \quad \mathbf{S}_t^{-1} \mathbf{c}_{out} = 0, \tag{2.34}$$

which corresponds to the poles of $\mathbf{S}_t$ matrix. In other word, the QNM complex frequencies are those which make the determinant of the $\mathbf{S}_t$ matrix zero. There is an equivalent method, referred to as the round-trip matrix method, which is easier and more efficient to implement in the FMM compared to the first method [46]. In this approach, the QNMs are eigenmodes of a round-trip matrix $\mathbf{U}$ inside the cavity with an eigenvalue of 1. They are found for a complex frequency $\tilde{\omega}$, and the QNM frequency will be the real part of $\tilde{\omega}$, and its Q-factor is obtained by $Q = \Re(\tilde{\omega})/[2\Im(\tilde{\omega})]$ [46], [47]. The round-trip matrix $\mathbf{U}$ is obtained at an arbitrary plane inside the cavity by determining the S-matrices seen to the left $\mathbf{S}_{t,11}^{(left)}$ and right $\mathbf{S}_{t,11}^{(right)}$ as shown in Fig. 2.8:

$$\mathbf{U} = \mathbf{S}_{t,11}^{(right)} \mathbf{S}_{t,11}^{(left)}. \tag{2.35}$$

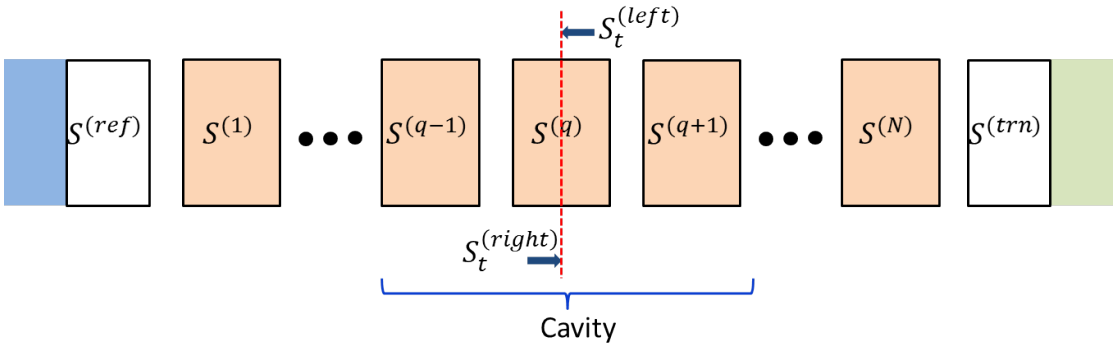

Figure 2.8: Definitions of the left and right S-matrices used for the cavity round-trip matrix **U**.

Therefore, the QNM in this method is found by iterating the frequency in the complex plane until the eigenvalue of matrix **U** becomes unity. Although, it usually finds the resonance wavelength in less than 10 iterations, depending on the initial guess for resonance wavelength and the cavity structure, it may require much more iterations. From our experience, the main advantage of this method is that it can be successful for finding the QNM in most cases, even with inaccurate initial guess for the resonance wavelength. However, it can only find single QNM for each function call.

Method II: Quasi-Normal Mode with Real Frequency

In this approach, the QNM with round-trip method is employed in real frequency domain instead of complex frequency plane of 'Method I', but the phase of **U** eigenvalue is considered [48]. If R_r is the eigenvalue of matrix **U**, the resonance wavelength λ_r is found as the wavelength, which makes the phase of R_r zero, i.e. $arg(R_r)$=0. This is equivalent to a constructive interference condition for a round-trip inside the cavity. The Q-factor is then obtained by [48]:

$$Q = \frac{-\lambda_r}{2(1-R_r)} \frac{\partial}{\partial \lambda} arg(R_r) \tag{2.36}$$

where the derivative is evaluated at λ_r and $arg(R_r)$=0. For the implementation of this method, the eigenvalues R_r are computed for several wavelengths close to the guessed resonance wavelength. The resonance wavelength can be found by interpolation or extrapolation of the eigenvalue phase, where $arg(R_r)$ becomes zero. If there are several close resonances, this method is very efficient numerically, since it can find all the resonance wavelengths and their Q-factor in one function call. For instance, Fig. 2.9 shows the amplitude and phase of several eigenvalues of matrix **U** in an exemplary HG-based vertical cavity structure. Each graph corresponds to a transverse mode.

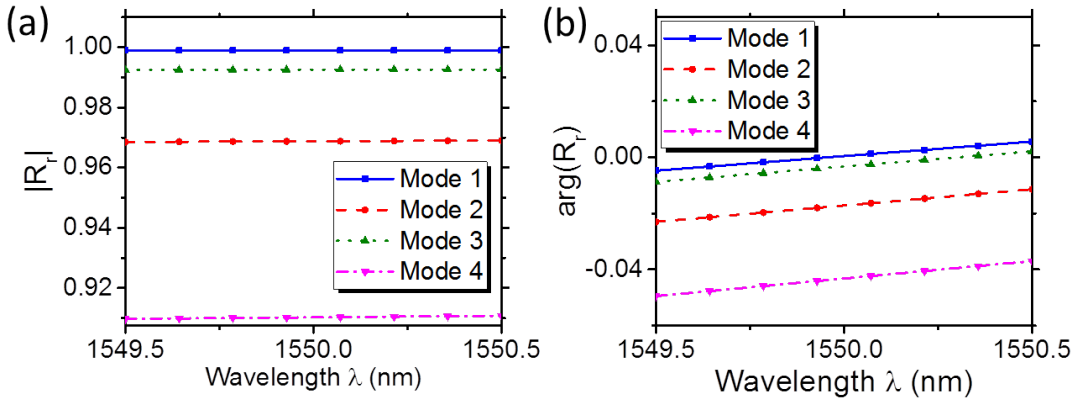

Figure 2.9: Evolution of eigenvalue (a) amplitude, and (b) phase of the round-trip matrix **U** as a function of wavelength close to a resonance wavelength for a test 2D HCG-based cavity. Each graph corresponds to a transverse mode. The Structure dimensions and refractive-indices can be found in Appendix C, section C.1.1.

Method III: Reflectivity Dip or Transmissivity Peak

The most straightforward method for determining the cavity resonances is to consider reflectivity (or transmissivity) spectrum of an optical cavity, i.e. consider the response to an incident wave. In this method, a notch in the reflectivity spectrum (or a peak in transmissivity spectrum) corresponds to a resonance wavelength. The Q-factor is estimated as the ratio of the resonance wavelength λ_r and the full-width half-maximum (FWHM) bandwidth of the notch (or peak), $Q = \lambda_r/\Delta\lambda$. Regarding the incident wave, we should be sure that the incident wave can excite the cavity mode, e.g. the incident wave is required to have the same parity as the cavity mode profile. Here, the fundamental mode of the test HCG-based cavity is excited by a Gaussian wave from the superstrate. The reflectivity and transmissivity spectra are shown in Fig. 2.10(a) and the field profile at the resonance wavelength is shown in Fig. 2.10(b).

Table 2.2 compares the simulation results from the three methods, obtained for the fundamental mode resonance wavelength and Q-factor of the test HCG-based vertical cavity of Figs. 2.9 and 2.10. The two methods in the QNM picture, result

Case	Method I	Method II	Method III
λ_r (nm)	1549.9549	1549.9548	1549.955
Q	7812	7815	7750

Table 2.2: Comparison between simulation results of different methods for resonance wavelength λ_r and Q-factor Q of the fundamental mode in a test HCG-based cavity. The simulated structure is the one used for Fig. 2.9.

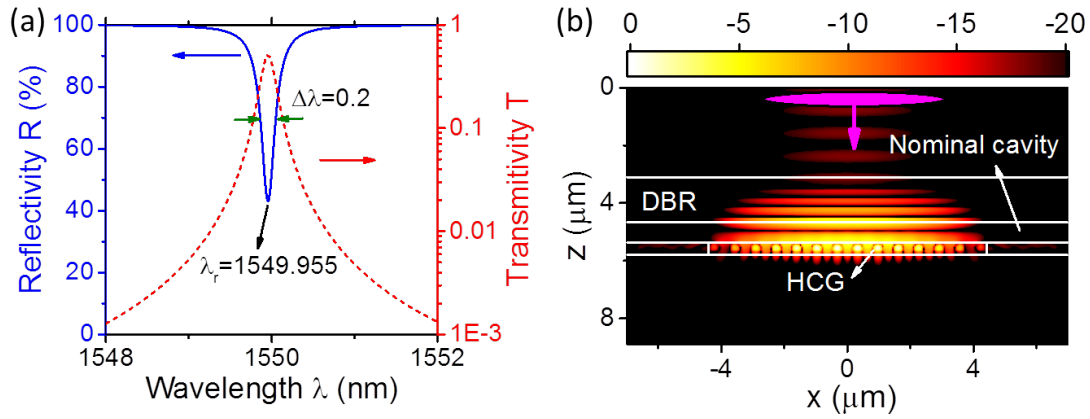

Figure 2.10: (a) Reflectivity spectrum in linear scale (blue solid-line) and transmissivity spectrum in log scale (red dashed-line) of a 2D HCG-based cavity as shown in Fig. 2.3(b) to an incident Gaussian beam with 6 μm beam waist width. The resonance wavelength and FWHM are also specified. (b) Normalized field profile $|H_y|$ of the structure (in dB scale) at the resonance wavelength of λ_r=1549.955. The simulated structure is the one used for Fig. 2.9.

in almost similar values for both the resonance wavelength and Q-factor (their relative difference is less than 10^{-7} for the resonance wavelength and 10^{-3} for the Q-factor). These negligible differences can be attributed to the round-off errors in the calculations and is less than the accuracy of the computations. 'Method III' results is a little bit different values compare to other methods, especially for the Q-factor, since the exact value of FWHM bandwidth is difficult to be defined for a large Q-factor mode. It should be mentioned that from the numerical point of view, the calculation time can be very different for these methods. The 'Method II' is the fastest method because there is no need to calculate reflectivity spectrum and several resonances can be found in a simple function call. The 'Method III' is the most time-consuming method, since it requires fine wavelength resolution scan, particularly for large Q-factor modes.

2.2.7 Threshold Gain and Confinement Factor

For each mode of a laser, there are two important parameters which can be calculated with optical simulation of the laser cavity; optical confinement factor of the mode Γ_m, which shows the overlap between the active region and the optical mode profile, and the threshold gain $g_{th,m}$, which shows the required gain in the active region to compensate the total loss of the optical mode. The product of these two quantities is referred to as modal threshold gain $\bar{g}_{th,m}$, and should be equal to the total loss of the optical mode at the threshold [1]:

$$\bar{g}_{th,m} = \Gamma_m g_{th,m} = \alpha_{t,m} \tag{2.37}$$

where $\alpha_{t,m}$ is the total loss of the optical mode m including the absorption material loss, the scattering loss and the mirror loss. If the absorption loss is negligible, $\alpha_{t,m}$ is related to the Q-factor of optical mode Q_m; $v_g\alpha_{t,m} = 1/\tau_m = \omega_m/Q_m$, where τ_m is the optical mode photon life-time and ω_m is the optical mode resonance frequency. Using Eq. (2.37), results in $\bar{g}_{th,m} = \Gamma_m g_{th,m} = 2\pi n_{a,g}/(\lambda_m Q_m)$, in which $n_{a,g}$ is the group refractive-index (group velocity) in the active region. In the optical simulation of the cavity, all of these three quantities can be calculated separately and the modal threshold gain $\bar{g}_{th,m}$ calculated from the two expressions, agrees relatively well as shown below.

The optical confinement factor is calculated for each mode using the field profile of the mode. The mode is calculated as a QNM, which is obtained by employing one of the methods explained in section 2.2.6. There are several different expressions for calculating the optical confinement factor [49]. Here, the expression derived rigorously for the confinement factor in Ref. [49] is used:

$$\Gamma_m = \frac{\iiint_{active} \frac{n_{a,g}}{n_a} \epsilon_0 \epsilon_r |\vec{\mathbf{E}}_m|^2 \mathrm{dV}}{\frac{1}{2} \iiint (\epsilon_0 \epsilon_r |\vec{\mathbf{E}}_m|^2 + \mu_0 \mu_r |\vec{\mathbf{H}}_m|^2) \mathrm{dV}} \tag{2.38}$$

where $\vec{\mathbf{E}}_m$ and $\vec{\mathbf{H}}_m$ are the electric and magnetic fields of the optical mode m, respectively, and $n_{a,g}$ is the group velocity inside the active region. The integral in the nominator is calculated over the active region and the one in the denominator is calculated all over the simulation domain.

In the QNM picture, the threshold gain can be calculated in a straightforward manner as it is explained in Ref. [50]. The gain g is introduced in the structure by an imaginary refractive-index value n_i in the active region, $n_i = g\lambda_0/4\pi$. By increasing the gain value, the absolute value of eigenvalue of the round-trip matrix $|R_r|$ is increased [50]. Threshold material gain is defined as the gain value which

Mode No.	$\lambda_{r,m}$ (nm)	Q_m	$g_{th,m}$	Γ_m (%)	$\bar{g}_{th,m}(1)$	$\bar{g}_{th,m}(2)$
1	1549.5155	6177.7	1024.7	2.03	20.801	20.781
2	1548.3202	1622.5	3967.3	1.97	78.156	79.185
3	1546.7190	628.4	10576.7	1.87	197.784	204.665

Table 2.3: Calculated modal properties of several transverse modes of a 2D HCG-based vertical cavity. All gain values are in cm^{-1} unit. $\bar{g}_{th,m}(1)$=$\Gamma_m g_{th,m}$ and $\bar{g}_{th,m}(2)$=$2\pi n_{a,g}/(\lambda_m Q_m)$ which shows a relatively good agreement between two methods of threshold modal gain calculation, particularly for the higher Q-factor modes. The Structure dimensions and refractive-indices can be found in Appendix C, section C.1.2.

results in an exact eigenvalue of one, i.e. $|R_r|$=1, for the round-trip matrix $\mathbf{U}$. By incorporating the gain, the resonance wavelength will also shift and the eigenvalue should be made one, by searching in a two-dimensional space of wavelength and gain. However, in practice the resonance wavelength and threshold gain can be determined in a two-step calculations [50]. First, the resonance wavelength of the passive structure (with zero gain) is calculated, in which $arg(R_r)$ becomes zero and $|R_r|$ is smaller than one. Then, at the resonance wavelength, the gain is increased from zero to make $|R_r|$ one (even though the $arg(R_r)$ will not be zero anymore but it will be relatively small), which defines the threshold gain. If the Q-factor of the optical mode is large enough, e.g. above several hundreds, at the end of step two, $arg(R_r)$ will be very small (e.g. less than 10^{-5}) and R_r will be approximately one. For instance, the optical confinement factors, resonance wavelengths and threshold gains of the three highest order modes of a 2D HCG-based cavity are shown in Table 2.3. The modal threshold gain values, obtained from either $\Gamma_m g_{th,m}$ or $2\pi n_{a,g}/\lambda_m Q_m$, are approximately the same, particularly for the optical modes with higher Q-factor. The small difference can be attributed to the round-off error in the results and is less than the calculation tolerance. The modal stability of the laser can easily be determined by the threshold gains as [51]:

$$\text{Modal stability} = \frac{g_{th,1} - g_{th,0}}{g_{th,0}} \tag{2.39}$$

where $g_{th,0}$ and $g_{th,1}$ are the threshold gain values for the fundamental and first order mode, respectively.

2.2.8 Convergence of Simulation Results

Similar to other numerical techniques, we should study the convergence behavior of the computations to confirm their validity. In the FMM, it is done by plotting the desired parameter as a function of number of Fourier terms $N_t = M_x N_y$. Numerically, if the relative error of the desired parameter is within the acceptable error for large N_t, we say that the simulation is converged. In this work, the relative error of a desired parameter is defined with respect to, either its final value, which is determined for a large N_t, or its previous value, which is obtained for the nearest and smaller N_t. Simulations in chapter 3, are mostly performed on a grating structure to obtain its reflectivity amplitude and phase. In chapter 4, vertical cavity structures consist of gratings are investigated, and parameters of interest are the resonance wavelengths and Q-factors of cavity modes. Therefore, here the value of these parameters for a 2D test structure are computed as a function of

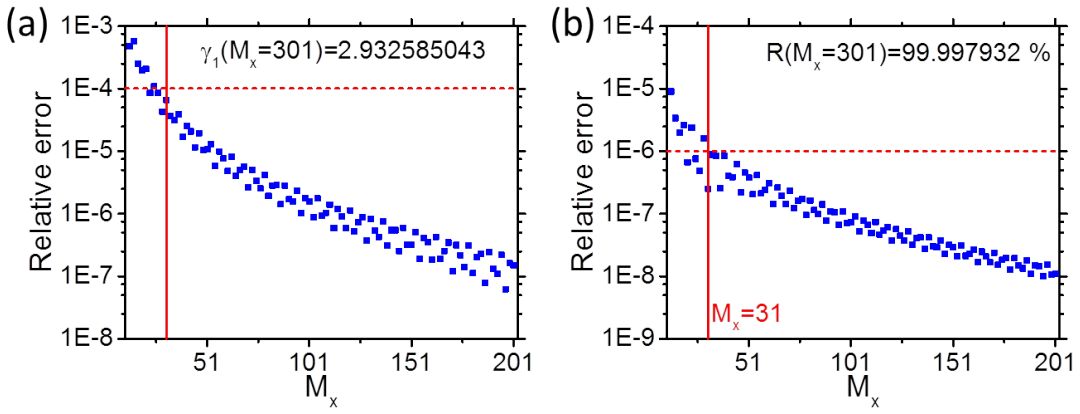

Figure 2.11: Relative error of (a) the largest eigenmode propagation constant γ_1, and (b) reflectivity amplitude R to a normally-incident plane-wave of a HCG for TM polarization, versus the number of Fourier terms M_x. The relative error is obtained with respect to the final value, which is determined for a large M_x, e.g. 301. The solid-lines correspond to M_x=31 and dashed-lines specify a relative error of 10^{-4} and 10^{-6} in (a) and (b), respectively. The simulated HCG is the one used for Fig. 2.9.

number of Fourier terms in the x-direction M_x, and the minimum required M_x for a specific relative error is determined.

For a periodic structure, whether it is a simple grating or a cavity consists of the grating, the PML and ASR techniques are not employed. Figures 2.11(a) and 2.11(b) illustrate the relative error in the largest eigenmode propagation constant γ_1 and reflectivity amplitude R, respectively, of an exemplary HCG versus M_x. Even though the value of R is a little bit more accurate compared to β, but this is a coincidence and it can occur oppositely by changing the grating parameters or light wavelength. Therefore, both β and R show relatively similar convergence rate, and from our experience, other desired parameters behave analogously. In this dissertation, M_x is chosen to be 31 for simulation of grating structures, and the computation uncertainty is less than 0.01% for the reflectivity amplitude or phase.

If the grating is used as a reflector in a vertical cavity, the parameters of interest are the resonance wavelength and Q-factor of cavity modes. Figures 2.12(a) and 2.12(b) show the resonance wavelength λ_r and Q-factor, respectively, of the fundamental cavity mode as a function M_x for infinitely periodic grating (just one period of the structure in Fig. 2.3). λ_r shows a convergence rate similar to Fig. 2.11, since it depends linearly on the reflectivity phase from mirrors [c.f. Eq. (2.2)]. However, the convergence rate for Q-factor is reduced by approximately three to four orders of magnitude, which has been also reported for other numerical techniques such as FDFD [52]. This can be explained by using the analytic expression of

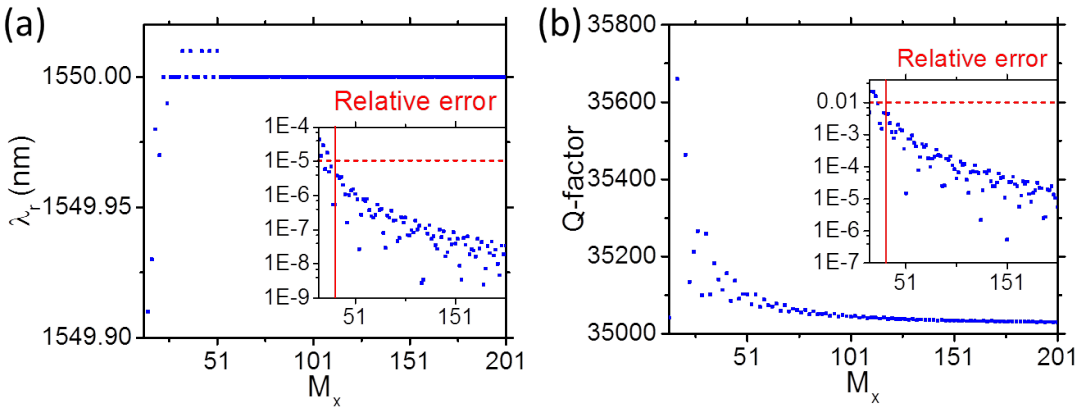

Figure 2.12: (a) Resonance frequency, and (b) Q-factor of the fundamental mode in a HCG-based vertical cavity versus the number of Fourier terms M_x, assuming infinitely periodic grating. The insets show the relative error of calculations, which is obtained for each point with respect to the previous point, i.e. it is calculated as $RE(n) = [a(n) - a(n-1)]/a(n)$. The solid-lines correspond to M_x=31 and dashed-lines shows relative error of 10^{-4} and 10^{-2} in (a) and (b), respectively. The simulated structure is the one used for Fig. 2.9.

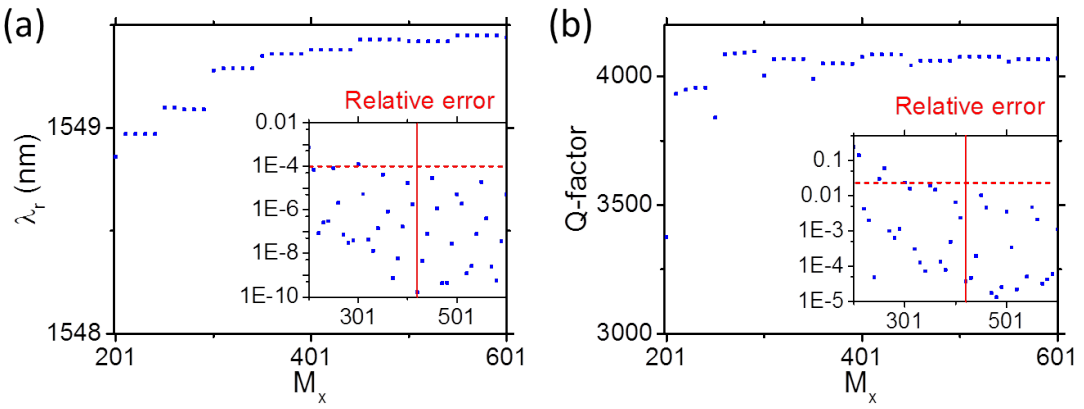

Figure 2.13: (a) Resonance wavelength, and (b) Q-factor of the fundamental mode in a 2D HCG-based vertical cavity structure versus M_x. The insets show the relative error of calculations, which is obtained with respect to the value. The solid-lines correspond to M_x=31*14=434 and dashed-lines show a relative error of 10^{-4} and 10^{-2} in (a) and (b), respectively. Simulation parameters are the same as Fig. 2.10.

the mode Q-factor in Fabry-Perot cavities [1]:

$$Q = \frac{4\pi n_{c,g} t_{eff}}{\lambda_r} \frac{1}{\ln(R_1 R_2)} \tag{2.40}$$

where t_{eff} is the effective cavity length considering the mirror penetration depths, $n_{c,g}$ is the group refractive-index of the cavity, and R_1 and R_2 are the power reflectivity amplitude from the two cavity mirrors. If the only uncertainties are in

the value of R_1 and R_2, the uncertainty in mode Q-factor will be:

$$\frac{\Delta Q}{Q} = -Q\Big(\frac{\Delta R_1}{R_1} + \frac{\Delta R_2}{R_2}\Big) \tag{2.41}$$

Therefore, the relative error in the Q-factor is approximately Q-times more than that of the corresponding value for the reflectivity amplitude, which is also confirmed here, in Fig. 2.12(b).

For a 2D HCG-based cavity structure consists of finite number of grating periods as shown in Fig. 1.2(b), the PML technique is employed in the x-direction. If $M_{x,1period}$ is the number of Fourier terms for simulating one grating period, in order to obtain a specific relative error in calculations, we can guess at least $N_g M_{x,1period}$ Fourier terms are required for the same level of accuracy, where N_g is the number of grating periods. Figure 2.13 illustrates the convergence test of the resonance wavelength and Q-factor of cavity mode in the exemplary HCG-based cavity with N_g=14 grating periods. The relative error may be a little bit larger than what is obtained from the infinite case of Fig. 2.12, which can be attributed to the larger simulation domain due to an extra space employed beside the grating region area. Therefore, for vertical cavity simulations in chapter 4, the number of Fourier terms is chosen depending on the number of grating periods as $M_x = N_g * 31$, and the calculation errors should be less than 1% and 0.01% for the Q-factor and resonance wavelength of cavity mode, respectively.

2.3 Rate Equations

As mentioned in chapter 1, laser is a complex multi-physics system. However, a simple phenomenological approach based on the rate equations is explained in this section, which can predict the major properties of the laser diode behavior. It is assumed that the active region is where the carriers recombine, contribute to the gain and make the output photons [1]. The dynamics of the carriers and photons in the active region can be investigated by modeling them as two coupled reservoir as shown schematically in Fig. 2.14. The rate equations for the carrier density N and photon density N_p (both in cm^{-3} unit), respectively in the active volume V and modal volume V_p (in cm^3 unit), are written as [1]:

$$\frac{dN}{dt} = \frac{\eta_i I}{qV} - (R_{nrl} + R_{sp}) - v_g g N_p, \tag{2.42a}$$

$$\frac{dN_p}{dt} = -\frac{N_p}{\tau_p} + \Gamma\beta_{sp} R_{sp} + \Gamma v_g g N_p \tag{2.42b}$$

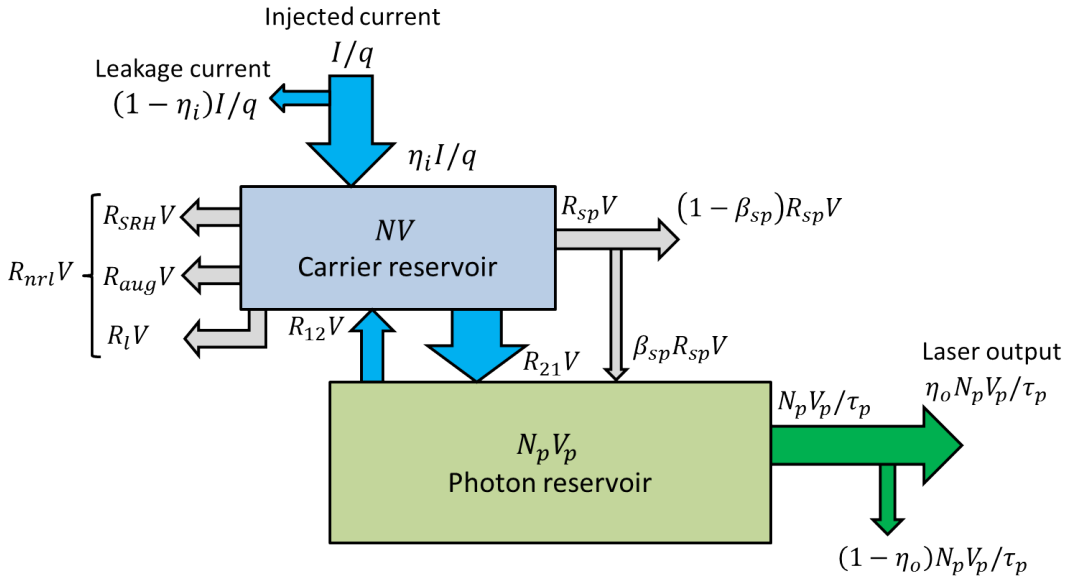

Figure 2.14: Reservoir model used for phenomenological dynamic analysis of the laser diode [1].

where $\Gamma = V/V_p$ is the optical confinement factor, η_i is injection current efficiency, v_g is the group velocity in the active region, R_{sp} and β_{sp} are the spontaneous recombination term and spontaneous emission factor, respectively. All the non-radiative recombination rates with carrier leakage are summed together and denoted by $R_{nrl} = R_l + R_{SRH} + R_{aug}$. Furthermore, the laser output power will be $P_o = \eta_o h\nu N_p V_p/\tau_p$, where τ_p and η_o are photon lifetime and output efficiency, respectively. These two rate equations can be used to predict steady-state performance and also dynamics response of a laser diode [1].

These equations can be expanded for a laser with several optical modes, where each mode m has its own photon density, denoted by S_m, and its own confinement factor Γ_m, gain g_m, lifetime τ_{sm} and spontaneous emission factor β_m [1]:

$$\frac{dN}{dt} = \frac{\eta_i I}{qV} - (R_{sp} + R_{nrl}) - \sum_m v_g g_m S_m, \tag{2.43a}$$

$$\frac{dS_m}{dt} = -\frac{S_m}{\tau_{sm}} + \beta_m \Gamma_m R_{sp} + \Gamma_m g_m S_m. \tag{2.43b}$$

2.3.1 Spatially-Dependent Rate Equations

Usually rate equations are written for the total carrier and photon densities as Eqs. (2.43), and are solved assuming N and S_m are spatially-independent variables. However, it is well-known that the carrier density varies across the active region, since the field amplitude, gain value and injection current change across the active

region. Therefore, a diffusion current term should be added to the rate equations due to carrier density variation, which results in the spatially-dependent rate equations [53], [54]. Various phenomena in the VCSELs such as transverse mode competition, spatial hole burning [55]–[57] or turn-off transient effect can be understood by the spatially-dependent carrier density [55], [58].

Since in a typical VCSEL, the active region is usually a thin layer, the carrier variation in the z-direction can be neglected and the spatially-dependent terms are considered only in the plane (x_1, x_2), where x_1 and x_2 can be any coordinate variable in the plane such as (x, y) or (r, θ). Furthermore, it is assumed that the photon density at each position is proportional to the electric field intensity $|\vec{\mathbf{E}}_m(x_1, x_2)|^2 = \hat{\psi}_m(x_1, x_2)$ at that position and the field profile does not change with time, i.e. $S_m(x_1, x_2, t) = S_m(t)\psi_m(x_1, x_2)$ [56], [59]. In other words, the photon spatial distribution will not change for each mode but the the number of the photons in the mode may change with time. If the carrier leakage and the non-radiative recombinations are negligible, i.e. $R_{nrl} = 0$ and the spontaneous recombination at each position is proportional to the carrier density at that position with a constant carrier lifetime τ_N, after integrating the second equation over the active region, the following equations are derived [56]:

$$\begin{aligned}\frac{\partial N(x_1,x_2,t)}{\partial t} &= \frac{\eta_i I(x_1,x_2,t)}{qV} - \frac{N(x_1,x_2,t)}{\tau_N} + D_N\nabla^2 N(x_1,x_2,t) \\ &\quad - v_g \sum_m G_m(x_1,x_2,t)S_m(t), \qquad (2.44a)\\ \frac{\partial S_m(t)}{\partial t} &= -\frac{S_m(t)}{\tau_{sm}} + \frac{\beta_m \Gamma_m}{\tau_N A_m}\iint N(x_1,x_2,t)\mathrm{d}A \\ &\quad + v_g \frac{\Gamma_m}{A_m} S_m(t)\iint G_m(x_1,x_2,t)\mathrm{d}A \qquad (2.44b)\end{aligned}$$

where D_N is carrier diffusion coefficient (in cm^2/s unit), $\nabla^2 = \partial^2/\partial x^2 + \partial^2/\partial y^2$ is transverse Laplacian operator, $G_m(x_1, x_2, t) = g_m(x_1, x_2, t)\psi_m(x_1, x_2)$ is the gain feels by mode m, and $A_m = \iint \psi_m(x_1, x_2)\mathrm{d}A$ is the mode cross-section (in cm unit).

For the quantum well active region, the gain is proportional to the logarithmic of the carrier density [1]. However, in this thesis, in order to use the expansion techniques, a linear relationship between the gain and carrier density is assumed [56], [59], [60]. The gain dependency on the photon density is through the gain compression coefficients ϵ_m for each mode. Therefore, the gain *felt* by the optical mode m becomes:

$$G_m(x_1, x_2, t) = g_0 \frac{N(x_1, x_2, t) - N_{tr}}{1 + \epsilon_m S_m(t)}\psi_m(x_1, x_2) \qquad (2.45)$$

where g_0 and N_{tr} are the small signal gain coefficient and transparency carrier density, respectively. If the current density j is used instead of current I and its time and spatial variation becomes separated [56]:

$$\frac{I(x_1, x_2, t)}{V} = \frac{j(t) j_s(x_1, x_2)}{d_w}, \tag{2.46}$$

where d_w is the active layer thickness, $j(t)$ is the current density function in time (in A/cm^2 unit) and $j_s(x_1, x_2)$ is the current density spatial profile (with no dimension). If there are several closely packed active region, e.g. several thin quantum wells, it will be replaced by $n_w d_w$.

Even though, the spatially-dependent rate equations in Eqs. (2.44) may be solved by finite-difference techniques [55], [60], [61], it is numerically cumbersome to solve them using these methods and expansion techniques can be applied [56], [62]. The carrier density $N(x_1, x_2, t)$ can be expanded on a set of orthogonal basis functions $f_{kl}(x_1, x_2)$ with time-dependent coefficients $N_{kl}(t)$:

$$N(x_1, x_2, t) = \sum_{k,l} N_{kl}(t) f_{kl}(x_1, x_2), \tag{2.47a}$$

$$\iint f_{kl}(x_1, x_2) f_{pq}(x_1, x_2) dA = \alpha_{kl} \delta_{kp}, \delta_{lq} \tag{2.47b}$$

where δ_{kp} and δ_{lq} are delta Kronecker, and α_{kl} is normalization constants. The basis set of functions $\{f_{kl}(x_1, x_2)\}$ can be any set of orthogonal functions such as Fourier basis or Bessel functions, and the number of terms in the expansion is N_t.

Using these equations in Eqs. (2.44), after some algebra, the following equations are derived for $N_{kl}(t)$ and $S_m(t)$:

$$\begin{aligned} \frac{\partial N_{pq}(t)}{\partial t} &= \frac{\eta_i j(t)}{d_w q} \zeta_{pq} - \frac{N_{kl}(t)}{\tau_N} + D_N \sum_{k,l} \beta_{kl,pq} N_{kl}(t) \\ &\quad - v_g g_0 \sum_m \frac{S_m(t)}{1 + \epsilon_m S_m(t)} \Big[\sum_{k,l} \Psi_{kl,m,pq} N_{kl}(t) - \gamma_{m,pq} N_{tr} \Big] \end{aligned} \tag{2.48a}$$

$$\begin{aligned} \frac{\partial S_m(t)}{\partial t} &= -\frac{S_m(t)}{\tau_{sm}} + \frac{\beta_m}{A_m \tau_N} \sum_{k,l} b_{m,kl} N_{kl}(t) \\ &\quad + \frac{v_g g_0 S_m(t)}{A_m (1 + \epsilon_m S_m(t))} \Big[\sum_{k,l} \lambda_{m,kl} N_{kl}(t) - N_{tr} c_m \Big] \end{aligned} \tag{2.48b}$$

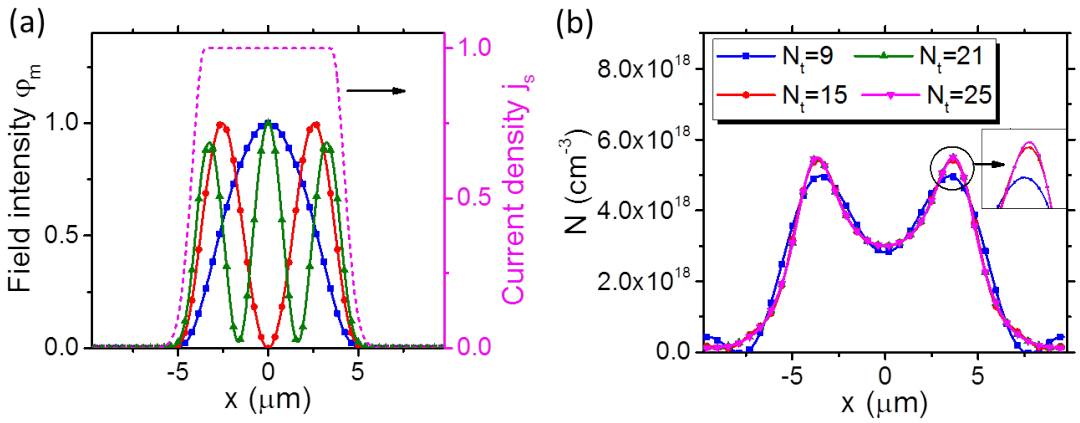

Figure 2.15: (a) The current density profile and three highest-order transverse modes of the HCG-based cavity of table 2.3 are shown in dashed-line and solid-lines, respectively. (b) The carrier spatial profile at I=2.5 mA current with a 7-μm square current aperture, for different number of Fourier terms in the expansion N_t. We chose N_t=15, since it results in relatively accurate result (less than 1 % change by increasing N_t to 35). Rate equation parameters are: η_i=0.8, D_N=5 cm^{-2}/s, τ_N=2.63 ps, N_{tr}=1e18 cm^{-3}, ϵ_m=1e-17 cm^3, v_g=3e10/4.2 cm/s, g_0=5.1e-16 cm^2 (obtained from Ref. [1]).

where the coefficients are defined as:

$$\zeta_{pq} = \frac{1}{\alpha_{pq}} \iint j_s(x_1, x_2) f^*_{pq}(x_1, x_2) \mathrm{d}A, \tag{2.49a}$$

$$\beta_{kl,pq} = \frac{1}{\alpha_{pq}} \iint \nabla^2 \big[f_{kl}(x_1, x_2) \big] f^*_{pq}(x_1, x_2) \mathrm{d}A, \tag{2.49b}$$

$$\Psi_{kl,m,pq} = \frac{1}{\alpha_{pq}} \iint f_{kl}(x_1, x_2) \psi_m(x_1, x_2) f^*_{pq}(x_1, x_2) \mathrm{d}A, \tag{2.49c}$$

$$\gamma_{m,pq} = \frac{1}{\alpha_{pq}} \iint \psi_m(x_1, x_2) f^*_{pq}(x_1, x_2) \mathrm{d}A, \tag{2.49d}$$

$$\lambda_{m,kl} = \Gamma_m \iint \psi_m(x_1, x_2) f_{kl}(x_1, x_2) \mathrm{d}A, \tag{2.49e}$$

$$b_{m,kl} = \Gamma_m \iint f_{kl}(x_1, x_2) \mathrm{d}A, \tag{2.49f}$$

$$c_m = \Gamma_m \iint \psi_m(x_1, x_2) \mathrm{d}A = \Gamma_m A_m. \tag{2.49g}$$

These integrals are calculated just once for a given current dentistry and optical mode profile. Eqs (2.48) are ordinary differential equations (ODEs) for $N_{kl}(t)$ and $S_m(t)$, which can be solved with any of the well-known methods with an initial condition.

As an example, Eqs. (2.48) are numerically solved for the 2D HCG-based cavity of Table 2.3. For conventional VCSELs, usually Bessel functions are employed as the basis set, due to the rotational symmetry of the structure [56], [57], [59]. However, a basis set of Fourier functions, i.e. cos and sin functions, are employed for HCG-based cavity, since it does not possess the rotational symmetry and

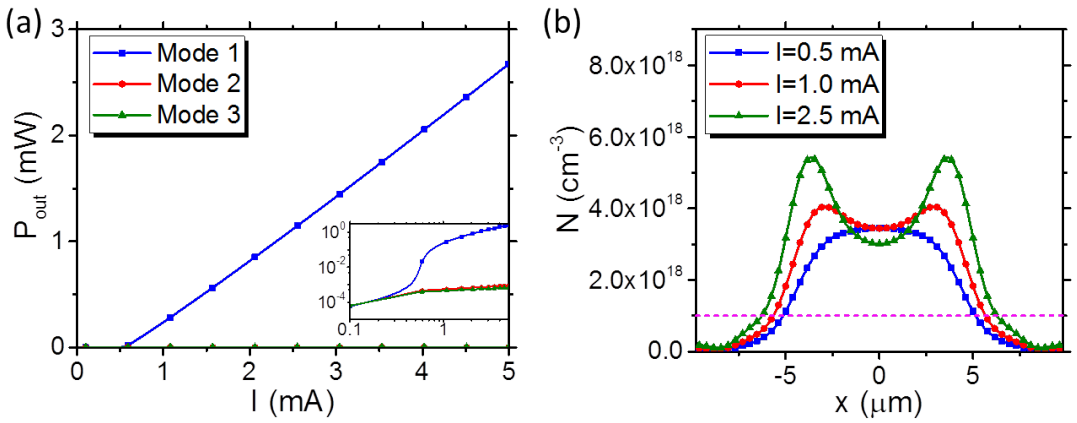

Figure 2.16: (a) The I-P curve for the HCG-based laser of Fig. 2.15. The inset shows the I-P curve in log-log scale. (b) The carrier density profile at several current values. Particularly, for high current values, the spatial hole-burning phenomena is observed.

also it is in-line with the FMM formulation which can simplify the evaluation of some of integrals in Eqs. (2.49). Three transverse modes of the cavity are shown in Fig. 2.15(a), and their optical properties are reported in table 2.3. Firstly, the convergence of the static carrier profile as a function of Fourier terms in the expansion N_t for a constant current is investigated and shown in Fig. 2.15(b). The convergence of the carrier profile is observed qualitatively form this graph. We chose N_t=15 as the sufficient number of terms for expansion, since it results in relatively accurate result (less than 1% change in carrier density by increasing N_t to 35). Figure 2.16(a) shows the I-P curve of the laser for a 7-μm square current aperture. Since higher order transverse modes have relatively small Q-factor compare to the fundamental modes, they are suppressed completely and the laser is a single mode laser. The carrier density profile is plotted in Fig. 2.16(b) for several current values, which shows spatial hole-burning phenomena especially in higher current values. Therefore, spatially-dependent rate equations, with Fourier functions as the basis set can be a strong tool for investigating the second order effects such as spatial hole burning in HCG-based lasers.

2.4 Summary

In this chapter, the numerical techniques for simulating the laser structures in this thesis are explained. For optical simulations, the Fourier modal method (FMM) is reviewed and the importance of absorbing boundary conditions implemented as perfectly-matched layer (PML) on an exemplary calculation is shown. Adaptive spatial resolution (ASR) technique is introduced and implemented, which is a

necessary tool for problems in which either high-level of accuracy is required, or metallic structures are included. However, for level of accuracy required in our computational problem, ASR does not provide considerable benefit. Several different numerical techniques for calculating the resonance wavelength and Q-factor of the cavity mode have been compared. Even though, they show good quantitative agreement with each other, quasi-normal mode method with real frequency is fast and accurate and is used in for calculations in chapter 4. We have shown and explained that the convergence rate of Q-factor is reduced by the value of Q compared to the resonance frequency or reflectivity amplitude convergence rate. Therefore, for the vertical cavity with N_g-periods of grating as the reflector in this thesis, employing 31^*N_g Fourier terms in the expansion provides accuracy of 1 % in the Q-factor and 0.01% for resonance wavelength of the mode, which is more than enough for our applications. We believe that the FMM is a robust and strong tool for investigating the physics of vertical cavity structures. Finally, spatially-dependent rate equations have been solved numerically with Fourier basis for a laser structure, which is compatible with the FMM and can be integrated with it easily.

References

[1] S. W. M. M. L. Coldren L.A. Corzine, *Diode Lasers and Photonic Integrated Circuits*, 2nd Ed. 2012 (cit. on pp. 16–18, 40, 44–47, 49).

[2] J. D. Joannopoulos, S. G. Johnson, J. N. Winn, and R. D. Meade, *Photonic Crystals: Molding the Flow of Light*, 2nd Ed. Princeton University Press, 2008 (cit. on pp. 21, 30).

[3] H. Kim, J. Park, and B. Lee, *Fourier Modal Method and Its Applications in Computational Nanophotonics*. CRC Press, 2012 (cit. on p. 21).

[4] R. C. Rumpf, "Improved formulation of scattering matrices for semi-analytical methods that is consistent with convention", *Progress In Electromagnetics Research B*, vol. 35, no. August, pp. 241–261, 2011 (cit. on pp. 22, 32–35).

[5] G. Granet and B. Guizal, "Efficient implementation of the coupled-wave method for metallic lamellar gratings in TM polarization", *Journal of the Optical Society of America A*, vol. 13, no. 5, pp. 1019–1023, 1996 (cit. on pp. 22, 23).

[6] J. J. Hench and Z. Strakos, "The RCWA method - a case study with open questions and perspectives of algebraic computations", *Electronic Transactions on Numerical Analysis*, vol. 31, pp. 331–357, 2008 (cit. on p. 22).

[7] L. Li, "Use of Fourier series in the analysis of discontinuous periodic structures", *Journal of the Optical Society of America A*, vol. 13, no. 9, pp. 1870–1876, 1996 (cit. on pp. 23, 32, 34).

[8] P. Lalanne and G. M. Morris, "Highly improved convergence of the coupled-wave method for TM polarization", *Journal of the Optical Society of America A*, vol. 13, no. 4, pp. 779–784, 1996 (cit. on pp. 23, 31).

[9] E. Popov and M. Neviere, "Maxwell equations in Fourier space: fast-converging formulation for diffraction by arbitrary shaped, periodic, anisotropic media", *Journal of the Optical Society of America A*, vol. 18, no. 11, pp. 2886–2894, 2001 (cit. on p. 23).

[10] A. David, H. Benisty, and C. Weisbuch, "Fast factorization rule and plane-wave expansion method for two-dimensional photonic crystals with arbitrary hole-shape", *Physical Review B*, vol. 73, no. 7, p. 075 107, 2006 (cit. on pp. 23, 24).

[11] T. Schuster, J. Ruoff, N. Kerwien, S. Rafler, and W. Osten, "Normal vector method for convergence improvement using the RCWA for crossed gratings", *Journal of the Optical Society of America A*, vol. 24, no. 9, pp. 2880–2890, 2007 (cit. on p. 23).

[12] P. Gotz, T. Schuster, K. Frenner, S. Rafler, and W. Osten, "Normal vector method for the rcwa with automated vector field generation", *Optics Express*, vol. 16, no. 22, pp. 17 295–17 301, 2008 (cit. on p. 23).

[13] L. Li, "New formulation of the Fourier modal method for crossed surface-relief gratings", *Journal of the Optical Society of America A*, vol. 14, no. 10, pp. 2758–2767, 1997 (cit. on pp. 23, 24, 32).

[14] P. Lalanne and H. Benisty, "Out-of-plane losses of two-dimensional photonic crystals waveguides: electromagnetic analysis", *Journal of Applied Physics*, vol. 89, no. 2, pp. 1512–1514, 2001 (cit. on p. 24).

[15] G. Lecamp, J. P. Hugonin, and P. Lalanne, "Theoretical and computational concepts for periodic optical waveguides", *Optics Express*, vol. 15, no. 18, pp. 11 042–11 060, 2007 (cit. on p. 24).

[16] T. Weiss, N. A. Gippius, S. G. Tikhodeev, G. Granet, and H. Giessen, "Efficient calculation of the optical properties of stacked metamaterials with a Fourier modal method", *Journal of Optics A: Pure and Applied Optics*, vol. 11, no. 11, p. 114 019, 2009 (cit. on pp. 24, 25).

[17] G. Granet, "Reformulation of the lamellar grating problem through the concept of adaptive spatial resolution", *Journal of the Optical Society of America A*, vol. 16, no. 10, pp. 2510–2516, 1999 (cit. on pp. 24, 25).

[18] T. Vallius and M. Honkanen, "Reformulation of the Fourier modal method with adaptive spatial resolution: application to multilevel profiles", *Optics Express*, vol. 10, no. 1, pp. 24–34, 2002 (cit. on pp. 24, 25).

[19] G. Granet and J.-P. Plumey, "Parametric formulation of the Fourier modal method for crossed surface-relief gratings", *Journal of Optics A: Pure and Applied Optics*, vol. 4, no. 5, S145–S149, 2002 (cit. on pp. 24, 25).

[20] T. Weiss, "Advanced numerical and semi-analytical scattering matrix calculations for modern nano-optics", PhD thesis, University of Stuttgart, 2011 (cit. on pp. 25, 27).

[21] A. Khavasi and K. Mehrany, "Adaptive spatial resolution in fast, efficient, and stable analysis of metallic lamellar gratings at microwave frequencies", *IEEE Transactions on Antennas and Propagation*, vol. 57, no. 4, pp. 1115–1121, 2009 (cit. on pp. 26, 27).

[22] J. Ctyroky, P. Kwiecien, and I. Richter, "Fourier series-based bidirectional propagation algorithm with adaptive spatial resolution", *Journal of Lightwave Technology*, vol. 28, no. 20, pp. 2969–2976, 2010 (cit. on p. 27).

[23] P. Debackere, P. Bienstman, and R. Baets, "Adaptive spatial resolution: application to surface plasmon waveguide modes", *Optical and Quantum Electronics*, vol. 38, no. 9-11, pp. 857–867, 2006 (cit. on p. 27).

[24] G. Granet and L. Li, "Convincingly converged results for highly conducting periodically perforated thin films with square symmetry", *Journal of Optics A: Pure and Applied Optics*, vol. 8, no. 6, pp. 546–549, 2006 (cit. on p. 27).

[25] J. P. Hugonin, P. Lalanne, I. D. Villar, and I. R. Matias, "Fourier modal methods for modeling optical dielectric waveguides", *Optical and Quantum Electronics*, vol. 37, no. 1-3, pp. 107–119, 2005 (cit. on pp. 28, 29).

[26] M. Pisarenco, J. Maubach, I. Setija, and R. Mattheij, "Aperiodic Fourier modal method in contrast-field formulation for simulation of scattering from finite structures", *Journal of the Optical Society of America A*, vol. 27, no. 11, pp. 2423–2431, 2010 (cit. on p. 28).

[27] P. Lalanne and E. Silberstein, "Fourier-modal methods applied to waveguide computational problems", *Optics Letters*, vol. 25, no. 15, pp. 1092–1094, 2000 (cit. on p. 28).

[28] E. Silberstein, P. Lalanne, J.-P. Hugonin, and Q. Cao, "Use of grating theories in integrated optics", *Journal of the Optical Society of America A*, vol. 18, no. 11, pp. 2865–2875, 2001 (cit. on p. 28).

[29] W. Chew, J. Jin, and E. Michielssen, "Complex coordinate system as a generalized absorbing boundary condition", *IEEE Antennas and Propagation Society International Symposium 1997. Digest*, vol. 3, no. 6, pp. 2060–2063, 1997 (cit. on p. 28).

[30] J. P. Hugonin and P. Lalanne, "Perfectly matched layers as nonlinear coordinate transforms: a generalized formalization", *Journal of the Optical Society of America A*, vol. 22, no. 9, pp. 1844–1849, 2005 (cit. on pp. 28, 29).

[31] Z.-Y. Li and K.-M. Ho, "Application of structural symmetries in the plane-wave-based transfer-matrix method for three-dimensional photonic crystal waveguides", *Physical Review B*, vol. 68, no. 24, p. 245 117, 2003 (cit. on pp. 30, 31).

[32] C. Zhou and L. Li, "Formulation of the Fourier modal method for symmetric crossed gratings in symmetric mountings", *Journal of Optics A: Pure and Applied Optics*, vol. 6, no. 1, pp. 43–50, 2004 (cit. on p. 31).

[33] M. G. Moharam, T. K. Gaylord, E. B. Grann, and D. A. Pommet, "Formulation for stable and efficient implementation of the rigorous coupled-wave analysis of binary gratings", *Journal of the Optical Society of America A*, vol. 12, no. 5, pp. 1068–1076, 1995 (cit. on p. 31).

[34] H. Yala, B. Guizal, and D. Felbacq, "Fourier modal method with spatial adaptive resolution for structures comprising homogeneous layers", *Journal of the Optical Society of America A*, vol. 26, no. 12, pp. 2567–2570, 2009 (cit. on p. 32).

[35] M. G. Moharam, T. K. Gaylord, D. A. Pommet, and E. B. Grann, "Stable implementation of the rigorous coupled-wave analysis for surface-relief gratings: enhanced transmittance matrix approach", *Journal of the Optical Society of America A*, vol. 12, no. 5, pp. 1077–1086, 1995 (cit. on p. 32).

[36] E. L. Tan, "Hybrid-matrix algorithm for rigorous coupled-wave analysis of multilayered diffraction gratings", *Journal of Modern Optics*, vol. 53, no. 4, pp. 417–428, 2006 (cit. on p. 32).

[37] M. Dems, T. Czyszanowski, and K. Panajotov, "Numerical analysis of high Q-factor photonic-crystal VCSELs with plane-wave admittance method", *Optical and Quantum Electronics*, vol. 39, no. 4-6, pp. 419–426, 2007 (cit. on p. 32).

[38] M. G. Moharam and A. B. Greenwell, "Efficient rigorous calculations of power flow in grating coupled surface-emitting devices", in *Proceedings of SPIE*, vol. 5456, 2004, pp. 57–67 (cit. on p. 32).

[39] P. Bienstman, "Rigorous and efficieent modelling of waveguide scale photonic components", PhD thesis, Gent University, 2001 (cit. on p. 34).

[40] Q. Cao, P. Lalanne, and J.-P. Hugonin, "Stable and efficient Bloch-mode computational method for one-dimensional grating waveguides", *Journal of the Optical Society of America A*, vol. 19, no. 2, pp. 335–338, 2002 (cit. on p. 35).

[41] Z.-Y. Li and L.-L. Lin, "Photonic band structures solved by a plane-wave-based transfer-matrix method", *Physical Review E*, vol. 67, no. 4, p. 046 607, 2003 (cit. on p. 35).

[42] Z.-Y. Li and K.-M. Ho, "Light propagation in semi-infinite photonic crystals and related waveguide structures", *Physical Review B*, vol. 68, no. 15, p. 155 101, 2003 (cit. on p. 35).

[43] A. Settimi and S. Severini, "Linking quasi-normal and natural modes of an open cavity", *Journal of Modern Optics*, vol. 57, no. 16, pp. 1513–1525, 2010 (cit. on p. 37).

[44] S. Severini, A. Settimi, C. Sibilia, M. Bertolotti, A. Napoli, and A. Messina, "Quasi-normal frequencies in open cavities: an application to photonic crystals", *Acta Physica Hungarica B: Quantum Electronics*, vol. 23, no. 3-4, pp. 135–142, 2005 (cit. on p. 37).

[45] T. Weiss, N. a. Gippius, S. G. Tikhodeev, G. Granet, and H. Giessen, "Derivation of plasmonic resonances in the Fourier modal method with adaptive spatial resolution and matched coordinates", *Journal of the Optical Society of America A*, vol. 28, no. 2, pp. 238–244, 2011 (cit. on p. 37).

[46] J. R. de Lasson, P. T. Kristensen, J. Mork, and N. Gregersen, "Roundtrip matrix method for calculating the leaky resonant modes of open nanophotonic structures", *Journal of the Optical Society of America A*, vol. 31, no. 10, pp. 2142–2151, 2014 (cit. on p. 37).

[47] G. Lecamp, P. Lalanne, J. Hugonin, and J. Gerard, "Energy transfer through laterally confined bragg mirrors and its impact on pillar microcavities", *IEEE Journal of Quantum Electronics*, vol. 41, no. 10, pp. 1323–1329, 2005 (cit. on p. 37).

[48] N. Gregersen, S. Reitzenstein, C. Kistner, M. Strauss, C. Schneider, S. Hofling, L. Worschech, A. Forchel, T. R. Nielsen, J. Mork, and J.-M. Gerard, "Numerical and experimental study of the Q factor of high-Q micropillar cavities", *IEEE Journal of Quantum Electronics*, vol. 46, no. 10, pp. 1470–1483, 2010 (cit. on p. 38).

[49] A. Mock, "First principles derivation of microcavity semiconductor laser threshold condition and its application to FDTD active cavity modeling", *Journal of the Optical Society of America B*, vol. 27, no. 11, pp. 2262–2272, 2010 (cit. on p. 41).

[50] B. Demeulenaere, P. Bienstman, B. Dhoedt, and R. Baets, "Detailed study of AlAs-oxidized apertures in VCSEL cavities for optimized modal performance", *IEEE Journal of Quantum Electronics*, vol. 35, no. 3, pp. 358–367, 1999 (cit. on pp. 41, 42).

[51] P. Bienstman, R. Baets, J. Vukusic, A. Larsson, M. Noble, M. Brunner, K. Gulden, P. Debernardi, L. Fratta, G. Bava, *et al.*, "Comparison of optical VCSEL models on the simulation of oxide-confined devices", *Quantum Electronics, IEEE Journal of*, vol. 37, no. 12, pp. 1618–1631, 2001 (cit. on p. 42).

[52] A. M. Ivinskaya, A. V. Lavrinenko, and D. M. Shyroki, "Modeling of nanophotonic resonators with the finite-difference frequency-domain method", *IEEE Transactions on Antennas and Propagation*, vol. 59, no. 11, pp. 4155–4161, 2011 (cit. on p. 43).

[53] P. Debernardi, "HOT-VELM: a comprehensive and efficient code for fully vectorial and 3-D hot-cavity VCSEL simulation", *IEEE Journal of Quantum Electronics*, vol. 45, no. 8, pp. 979–992, 2009 (cit. on p. 47).

[54] P. Debernardi, A. Kroner, F. Rinaldi, and R. Michalzik, "Surface relief versus standard VCSELs: a comparison between experimental and hot-cavity model results", *IEEE Journal of Selected Topics in Quantum Electronics*, vol. 15, no. 3, pp. 828–837, 2009 (cit. on p. 47).

[55] A. Valle, J. Sarma, and K. A. Shorey, "Secondary pulsations driven by spatial hole burning in modulated vertical-cavity surface-emitting laser diodes", *Journal of the Optical Society of America B*, vol. 12, no. 9, pp. 1741–1746, 1995 (cit. on pp. 47, 48).

[56] M. Jungo, D. Erni, and W. Bachtold, "VISTAS: a comprehensive system-oriented spatiotemporal VCSEL model", *IEEE Journal of Selected Topics in Quantum Electronics*, vol. 9, no. 3, pp. 939–948, 2003 (cit. on pp. 47–49).

[57] H. Zhang, G. Mrozynski, A. Wallrabenstein, and J. Schrage, "Analysis of transverse mode competition of VCSELs based on a spatially independent model", *IEEE Journal of Quantum Electronics*, vol. 40, no. 1, pp. 18–24, 2004 (cit. on pp. 47, 49).

[58] J. Morikuni, P. Mena, A. Harton, K. Wyatt, and S.-M. Kang, "Spatially independent VCSEL models for the simulation of diffusive turn-off transients", *Journal of Lightwave Technology*, vol. 17, no. 1, pp. 95–102, 1999 (cit. on p. 47).

[59] X. Li, W. Pan, B. Luo, and D. Ma, "Multi-transverse-mode dynamics of vertical-cavity surface-emitting lasers with external optical injection", *Journal of the Optical Society of America B*, vol. 23, no. 7, pp. 1292–1301, 2006 (cit. on pp. 47, 49).

[60] M. S. Torre, A. Valle, and L. Pesquera, "Transverse mode selection in vertical-cavity surface-emitting lasers with optical injected signal", *IEEE Journal of Quantum Electronics*, vol. 46, no. 1, pp. 105–111, 2010 (cit. on pp. 47, 48).

[61] A. Valle, "Selection and modulation of high-order transverse modes in vertical-cavity surface-emitting lasers", *IEEE Journal of Quantum Electronics*, vol. 34, no. 10, pp. 1924–1932, 1998 (cit. on p. 48).

[62] M. Jungo, D. Erni, and W. Baechtold, "Quasi-analytic steady-state solution of VCSEL rate equations including spatial hole burning and carrier diffusion losses", *International Journal of Numerical Modelling: Electronic Networks, Devices and Fields*, vol. 16, no. 2, pp. 143–159, 2003 (cit. on p. 48).

We men who serve science serve only a reflection in a mirror.

— Richard Byrd

3 Subwavelength Gratings

Contents

Gratings are periodic structures with many interesting properties and applications. They were first discovered by James Gregory in 16^{th} century due to their diffraction properties, since they can split a light beam into several beams, propagating in different directions. Afterwards, diffraction gratings found many applications such as monochromators and spectrometers, optical filters and spectral beam combiners. They also are used widely as a dispersive element, since their optical properties change with the frequency. Recently, due to the fabrication possibility of grating structures with a periodicity value on the order of light wavelength, gratings become interesting again and find new applications. Gratings in general can be one-, two- or three-dimensional, depending on the available spatial periodicity. In this thesis, our concentration is on the one-dimensional (1D)

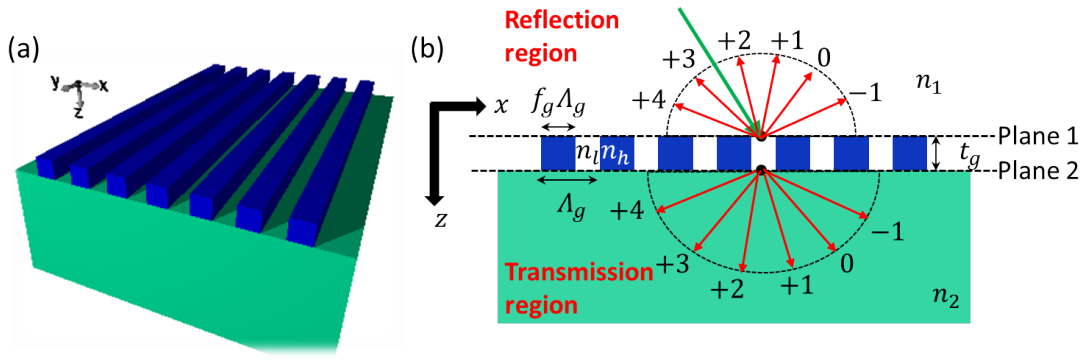

Figure 3.1: (a) Schematic view of a 1D grating structure. (b) Schematic cross-sectional view of the grating structure in (a) with its parameter definitions.

gratings, which are made of periodic array of bars surrounded by other material as shown schematically in Fig. 3.1. The grating equation, which is a relationship between grating period and angle of incident and diffracted beams, is employed to understand the fundamental properties of grating. If a monochromatic light beam with a wavelength of λ_0 and wavenumber of $k_0 = 2\pi/\lambda_0$ is incident on the grating at angle θ_{inc}, the grating equation is written as:

$$k_{x,m} = k_{x,inc} - mK, \quad m = 0, \pm1, \pm2, ..., \tag{3.1}$$

where m is the diffracted wave order, $K = 2\pi/\Lambda_g$ is the grating wavenumber, $k_{x,iinc} = n_1 k_0 \sin(\theta_{inc})$ is the x-component of incident wavevector and $k_{x,m}$ is the x-component of the diffracted beam wavevector in either reflection or transmission media. Using $k_{x,m} = n_1 k_0 \sin(\theta_{m,ref})$ and $k_{x,m} = n_2 k_0 \sin(\theta_{m,trn})$ for the reflected and transmitted beams, respectively, result in:

$$n_1 \sin(\theta_{m,ref}) = n_1 \sin(\theta_{inc}) - m\frac{\lambda_0}{\Lambda_g}, \quad m = 0, \pm1, \pm2, ..., \tag{3.2a}$$

$$n_2 \sin(\theta_{m,trn}) = n_1 \sin(\theta_{inc}) - m\frac{\lambda_0}{\Lambda_g}, \quad m = 0, \pm1, \pm2, ... \tag{3.2b}$$

For a diffracted beam, if $\sin(\theta_{m,ref})$ or $\sin(\theta_{m,trn})$ obtained from Eqs. (3.2) becomes larger than one; the beam will be evanescent in the reflection or transmission media. In other words, it can not propagate in the z-direction outside the grating region and far from the grating, it will be zero.

For a diffraction grating $\Lambda_g > \lambda_0/n_1$ or $\Lambda_g > \lambda_0/n_2$, and there are several diffracted beams in the reflection or transmission media, respectively [1]. The number of diffracted beams is increased for a larger grating period. In the opposite direction, a subwavelength grating is a grating with periodicity shorter than the wavelength $\Lambda_g < \lambda_0/max(n_1, n_2)$. Therefore, at the normal incident $\theta_{inc} = 0$, all

the diffracted beams with $m \neq 0$ are evanescent in the reflection and transmission media for a subwavelength grating structure, and only 0-th order diffracted beams are propagating inside the reflection and transmission regions. In the extreme case, for a deep-subwavelength grating with $\Lambda_g << \lambda_0$, the grating appears as an homogeneous medium to the incident light, with an effective refractive-index which depends on the light polarization [2].

High-index-contrast grating (HCG) is a special class of near-subwavelength grating, in which the grating period is close to the incident light wavelength and there is a large refractive-index contrast between the grating bars and materials surround it. HCGs can provide extraordinary properties that have not been reported for conventional diffraction gratings with similar periodicity, including high reflectivity ($> 99\%$) over a broad bandwidth [3], [4] or high quality (Q) factor resonances ($Q > 10^7$) [5], [6]. Extensive theoretical studies of HCGs have revealed that the high index-contrast between the grating and surrounding materials is essential for achieving the extraordinary properties [7]. However, we have found that the combination of a near-subwavelength grating and a cap layer, both made of high-refractive-index materials and surrounded by low-refractive-index materials, can achieve a high reflectivity over a broader wavelength range than the HCG [8], and also make resonances with ultra-high Q-factor [9]. We refereed to this novel grating structure as hybrid grating (HG).

In this chapter, two different physical pictures are introduced for understanding the working mechanism of grating structures. Using these two equivalent pictures, the working mechanism of the HCG as a broadband reflector or high Q-factor resonator is explained. Then, our novel proposed HG structure is investigated in details. Experimental characteristic of a fabricated HG reflector is provided which shows relatively good agreement with the theory. All the numerical results in this chapter are obtained by the implemented FMM as explained in chapter 2. Non-dispersive materials are assumed for ease of simulation, but dispersion can be easily introduced to the calculations.

3.1 Two Equivalent Physical Pictures

There are two equivalent pictures to understand the physics of a grating; guided-mode resonance (or leaky mode) picture and waveguide-array mode (or Bloch mode) picture. In the first picture, the grating layer is considered as a waveguide with a periodic refractive-index modulation in the x-direction which supports the so-called leaky modes [10]. This picture was first developed for low-index-contrast grating

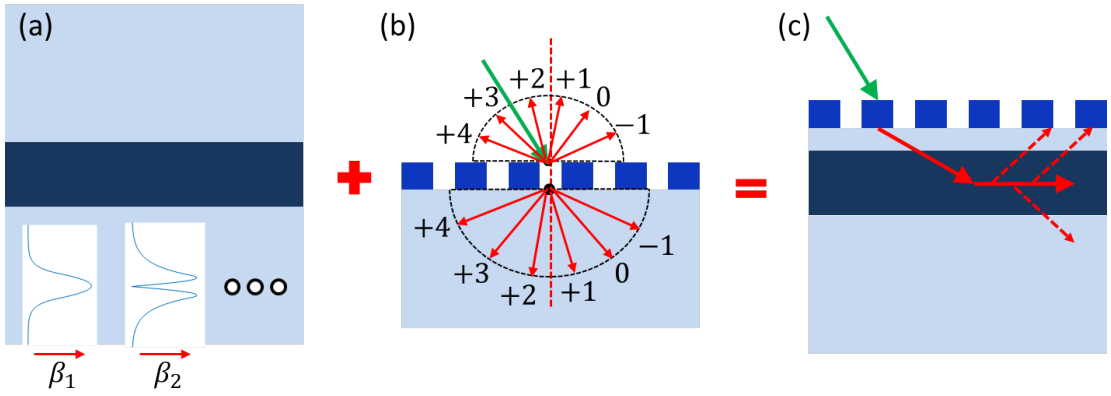

Figure 3.2: (a) Schematic of the cross section of a slab waveguide with several waveguide modes. (b) Schematic cross-sectional view of a grating with its diffracted beams. (c) A guided-mode resonance is obtained by an interaction between a waveguide mode and a grating mode. Dashed-lines show the leaky nature of the guided-mode.

structures [10], [11], but later, it was employed also for high-index-contrast grating structures [8], [12]. In the second picture, the grating is seen as a periodic array of short slab waveguides along the z-direction [2], [13]. This approach is introduced recently and provides a clear picture about the HCG and HG working mechanism [2], [8], [13]. In the following sections these two pictures are explained in more details.

3.1.1 Guided-Mode Resonance Picture

Guided-mode resonance (GMR) is a well-known phenomenon in the structures includes gratings, which has found many applications such as in optical filters and grating couplers [14], [15]. To understand the concept of GMR, first a simple slab waveguide is considered as shown schematically in Fig. 3.2(a). This waveguide can support one or several guided-modes with propagating constants of $\beta_n = n_{eff,n}k_0$, n=1,2,3, depending on the frequency and waveguide width. On the other hand, a grating can split the incident beam into several diffracted beams as shown schematically in Fig. 3.2(b), each one with a specific x-component wavevector, denoted by $k_{x,m}$. If the grating is placed in close proximity to the slab waveguide as shown in Fig. 3.2(c), and at a specific frequency, $k_{x,m} = \beta_n$ holds for a particular diffracted mode and a slab waveguide mode, the two modes can couple to each other [16]. This phase-matched condition, results in a sharp resonance in the reflectivity or transmissivity spectrum, since the electromagnetic power can be transferred between the grating diffracted beams and waveguide guided-modes. The guided-mode is sometimes referred to as the leaky mode, since it can transfer its power back to the diffracted beam, i.e. it is leaky.

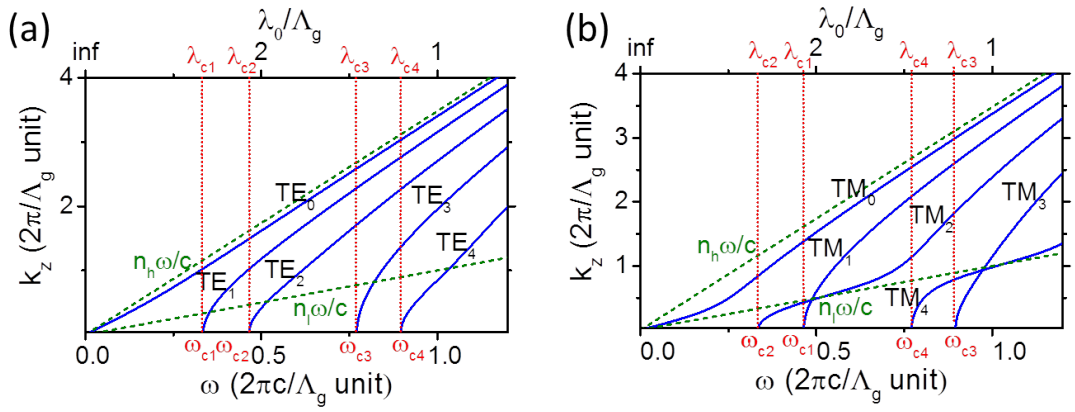

Figure 3.3: Dispersion curves for several waveguide-array modes (blue solid-lines) in (a) TE polarization, (b) TM polarization. The grating duty cycle is $f_g = 0.58$ and its refractive-indices are $n_h = 3.48$ and $n_l = 1.0$. Two light lines (green dashed-lines) corresponds to n_h and n_l. The cut-off frequencies (and corresponding wavelengths) are denoted by ω_{ci} (λ_{ci}), where i is the mode number.

It is not necessary to couple a separate waveguide and grating in order to observe GMRs. Similarly, a single grating layer can be seen as a waveguide with a periodic refractive-index modulation, which may support one or several guided-modes. Whenever, there is a phase-matched condition between grating guided-modes and its diffracted beams, a GMR appears in the reflectivity spectrum. If the refractive-index contrast is small in the grating layer, i.e. $n_h - n_l << 1$, the grating layer can be modeled as an effective homogeneous layer. In this case, the reflectivity spectrum consists of a slowly varying spectrum, due to the of the effective homogeneous layer, with sharp resonances, due to the GMRs [14]. This simple and elegant idea is used widely nowadays for designing optical filters based on GMR [11], [14].

3.1.2 Waveguide-Array Mode Picture

A grating can also be considered as a periodic array of short slab waveguides along the z-direction, which can support one or several waveguide-array modes [2], [13]. An incident wave on the grating excites one or several of these modes. The waveguide-array modes propagate along the z-direction inside the grating with different propagation constants, until they reach at the boundary of the grating layer, where they will be partially reflected back and partially transmitted to the propagating modes in the transmission region. The grating properties can be well-understood through the investigation of these modes and their interaction at the two interfaces. First, the dispersion of these waveguide modes should be studied.

The dispersion curves of the waveguide-array modes of a HCG are plotted in Fig. 3.3. In the FMM, these modes correspond to the grating layer eigenmodes with real propagation constants. In low-frequency regime, just the fundamental mode (TE_0 or TM_0) is propagating and all higher order modes are cut-off. In this single-mode regime, i.e. $\omega < \omega_{c1}$ for TE polarization or $\omega < \omega_{c2}$ for TM polarization, the grating can be seen as a homogeneous medium with an effective refractive-index. By increasing the frequency, the number of propagating modes is increased. Many interesting properties of the HCG and also the HG occurs in a region, where only two waveguide-array modes are propagating inside the grating layer, which is referred to as dual-mode (or two-mode) regime. For a normally-incident wave, it is the frequency range between ω_{c2} to ω_{c4}, since the odd waveguide-array modes cannot be excited by the normally-incident plane-wave [13].

3.2 High-Index-Contrast Grating

HCGs were first introduced and experimentally fabricated in 2004 [3], [4]. Due to their capability of providing high reflectivity over a broad wavelength range, they became an attractive alternative to DBRs in vertical cavity devices, particularly in VCSELs. Huang et al.[17] and Boutami et al.[18] independently demonstrated VCSELs with a HCG as a reflector. Since then, various novel vertical cavity laser structures employing the HCG have been reported, demonstrating MEMS-based wavelength tunability [19], [20], strong single-transverse-mode operation [21], and integration with an SOI wafer [22], [23]. Another interesting feature that might be integrated to VCSELs is the possibility of beam steering or focusing [24], [25]. There are many other interesting applications for HCGs besides replacing DBRs. Since HCGs can provide ultra-high Q-factor resonances [5], [26], standalone HCG-resonator lasers with surface normal emission have been demonstrated, with properties of interest for sensing, communication, or display applications [5], [6]. Moreover, hallow-core waveguides using HCGs are also proposed and fabricated [27], [28], where speed of propagating light can be controlled [29]. In this thesis, the properties and physics of HCG as a broadband reflector or a high Q-factor resonator are mainly discussed.

3.2.1 HCG as a Broadband Reflector

A HCG structure with a periodicity of Λ_g, thickness of t_g and duty cycle of f_g is shown in Fig. 3.1. Since Maxwell equations are scalable with respect to dimensions, without loss of generality, all the length scales are normalized with respect to

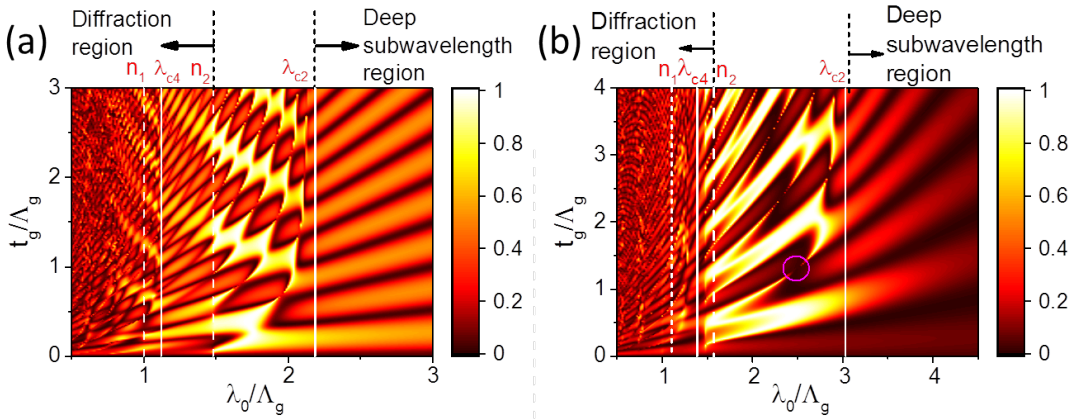

Figure 3.4: HCG contour maps of the reflectivity (color scale) versus normalized wavelength λ_0/Λ_g and grating thickness t_g/Λ_g for a normally-incident (a) TE-polarized, and (b) TM-polarized plane-wave. HCG parameters are defined in Fig. 3.1 and their values are n_h=3.48, n_l=1, n_1=1, n_2=1.48, and f_g=0.58. λ_{c2} and λ_{c4} are the (normalized) cut-off frequencies of waveguide-array modes and are defined in Fig. 3.3, and n_1 and n_2 are the refractive-indices of reflection and transmission regions, respectively, and define the wavelength boundaries for which higher-order diffracted beams appear. Dual-mode regime is also illustrated. The circle shows an example anti-crossing point.

Λ_g. Figures 3.4(a) and 3.4(b) show HCG reflectivity contour maps as a function of normalized grating thickness t_g/Λ_g and normalized wavelength λ_0/Λ_g for a normally-incident TE-polarized and TM-polarized plane-wave, respectively. Several distinct wavelength regions with different reflectivity patterns are clear from these contour maps as discussed below.

For very long wavelengths (i.e. $\lambda_0 > \lambda_{c2}$), the reflectivity contour maps remind us of the ones for a single dielectric slab. In this regime, the grating behaves like a homogeneous layer with an effective refractive-index, which is $n_{TE}^2 = f_g n_h^2 + (1-f_g) n_l^2$ for the TE polarization and $n_{TM}^{-2} = f_g n_h^{-2} + (1-f_g) n_l^{-2}$ for the TM polarization. This pattern is due to a constructive or destructive interference between the light beams which are reflected from the interface planes 1 and 2. For short wavelengths (i.e. $\lambda_0/\Lambda_g < n_2$), higher-order diffracted beams begin to appear in the reflection and transmission media. On top of that, there are three or more waveguide-array modes above the cut-off condition. Complex interaction between the diffracted beams and waveguide-array modes results in a interference pattern which makes the contour map less-ordered. Between the two regions, in which only two waveguide-array modes are propagating inside the grating and 0-th order diffracted beam is propagating outside the grating, a checker-board pattern with very high reflectivity areas (close to unity) is observed. The broadband high-reflectivity phenomenon in HCG occurs in this wavelength region.

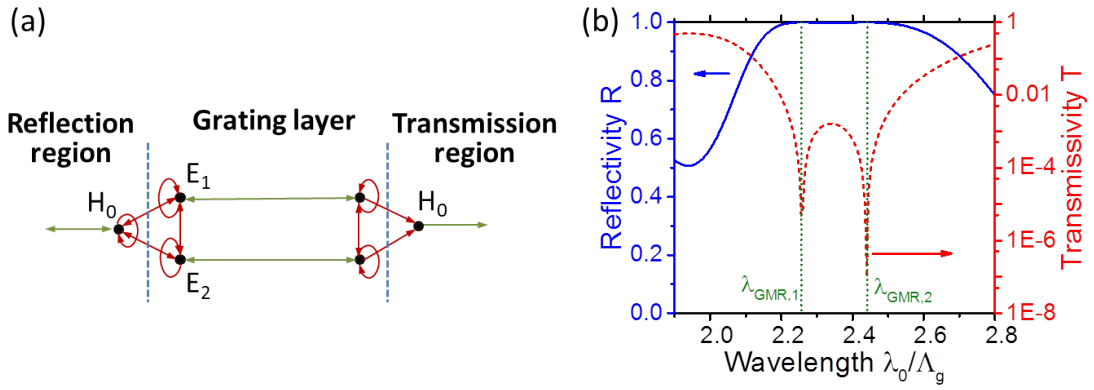

Figure 3.5: (a) Signal flow graph of HCG in dual-mode regime. The black dots represent the propagating modes in different layers; the red arrows show the interactions between modes at each interface; the circular red arrows bring self-couplings; the green arrows illustrate the propagations in each layer. (b) Reflectivity spectrum in linear scale (blue solid-line) and transmissivity spectrum in log-scale (red dashed-line) for a TM-polarized plane-wave, normally-incident to a HCG structure. The HCG is the one simulated in Fig. 3.4(b) at t_g/Λ_g=0.67.

The broadband reflection properties can be understood as a combined result of propagations of the two waveguide-array modes within the grating layer and their reflection at the interfaces [13]. Outside the grating region, there is one propagating mode, i.e. the 0-th order diffracted mode. A signal flow graph (SFG) in Fig. 3.5(a) illustrates how these modes interact with one another at interfaces [30]. Each dot, which is called a node, corresponds to a propagating mode. Interaction between modes are shown by arrows, and called branches, which take place at interfaces. The circular arrow represents reflection of a mode back to itself at the interface. If a plane-wave is normally incident to the grating layer, two waveguide-array modes are excited at the interface plane 1. These two modes propagate until they reach to the interface plane 2, where they are reflected back to themselves and also each other. Furthermore, they partially couple to the 0-th order diffracted mode in the transmission region. If the coupling occurs with opposite phase, i.e. a destructive interference of two waveguide-array modes at the interface plane 2, no power is transmitted to the transmission region. Consequently, all incident power is reflected back which makes unity reflectivity value. If two such unity-reflectivity points are located at close spectral vicinity, a broadband high reflectivity is achieved as shown in Fig. 3.5(b).

The HCG broadband high-reflectivity phenomenon can be understood using the GMR concept. As mentioned before, whenever a phase-matching condition between a grating diffracted beam and a guided-mode of the slab waveguide is satisfied, a GMR appears in the reflectivity spectrum. GMRs can also be viewed

as Fano resonances between the discrete grating modes and the continuous modes in surrounding homogeneous media. If multiple GMRs combined together, i.e. they locate at close spectral vicinity and they have good coupling with each others, high reflectivity can be achieved in broad wavelength range [12]. The GMR wavelengths correspond to the transmissivity dips, where the transmissivity becomes zero [12]. For instance, Fig. 3.5(b) shows reflectivity spectrum in linear-scale and transmissivity spectrum in log-scale of an HCG. Usually, there are two dips in the transmissivity spectrum inside the high-reflectivity bandwidth of HCG; each one corresponds to a GMR. The two GMRs provide two Fano-shape resonances with opposite parity which can make a broadband reflectivity spectrum in the wavelength range between them [31]. It should be noted that by breaking the reflection-symmetry in the grating unit-cell, it is possible to introduce more GMRs and increase the bandwidth [32], [33].

3.2.2 HCG as a High Q-Factor Resonator

Besides being used as a highly-reflective mirror in Fabry-Perot resonators, a standalone HCG can be employed as an optical resonator with ultra-high Q-factor and surface-normal emission [5], [6]. In this case, the HCG has a high Q-factor resonance which manifests itself by very sharp change in the reflectivity spectrum. As it was explained in Ref. [2], the resonance occurs around an anti-crossing point in the dual-mode regime, as one of them is indicated by a circle in Fig. 3.4(b). Figure 3.6(a) shows the reflectivity spectrum of the HCG of Fig. 3.4(b) close to the anti-crossing point. The Q-factor of this mode is approximately 10000, which results in a relatively strong field buildup in the grating region as illustrated in Fig. 3.6(b). This strong field buildup is a sign of constructive interference of the modes inside the grating, as discussed below. It should also be noted that the selected example is only for illustrating the physics of a high Q-factor resonance in the HCG, and it is possible to find ultra-high Q-factor resonances (as high as 10^9) simply by applying the systematic method, which is described for the HG structure in section 3.3.3.

The mechanism of HCG high Q-factor resonances is similar to the resonance mechanism in a conventional Fabry-Perot cavity. However, for the HCG, two waveguide-array modes simultaneously are contributing to the resonance instead of one mode in a conventional Fabry-Perot cavity [26]. If the propagation of the two modes in the grating layer and their reflectivity at interface planes 1 and 2 are denoted by matrix $\mathbf{\Psi}$ and $\mathbf{R}_i$, i =1,2 for each interface, respectively, a round-trip matrix can be defined as $\mathbf{U} = \mathbf{\Psi}\mathbf{R}_1\mathbf{\Psi}\mathbf{R}_2$. Therefore, a resonance occurs whenever the constructive interference condition is satisfied for a combination of two

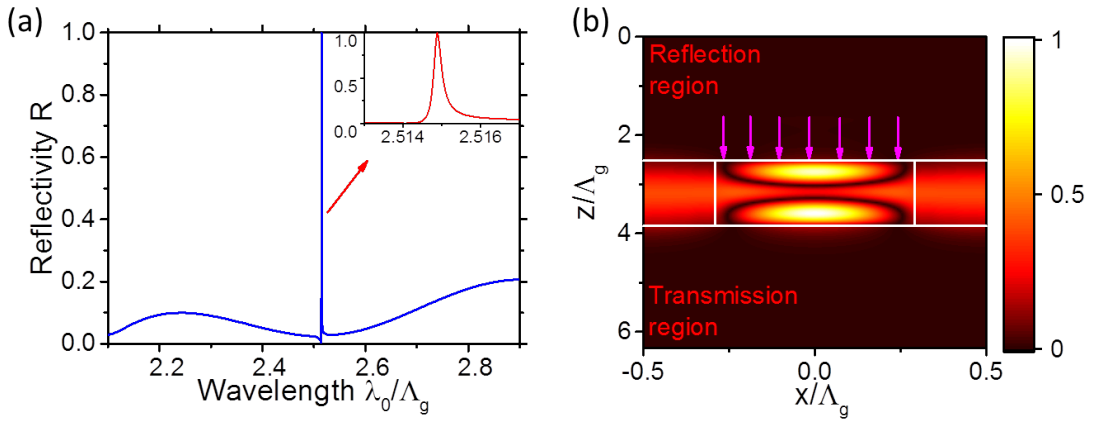

Figure 3.6: (a) Reflectivity spectrum of a HCG structure with a high Q-factor resonance in the spectrum. A TM-polarized light is normally-incident to the grating. The HCG structure dimensions and refractive indices are defined in Fig. 3.4 at thickness of t_g/Λ_g=1.33. (b) Normalized magnetic field profile $|H_y|$ at the resonance wavelength of (a).

waveguide-array modes, which corresponds to a unity eigenvalue for the round-trip matrix **U** [26]. It should be mentioned that by increasing the HCG thickness, the high Q-factor resonances occur periodically [26].

3.3 Hybrid Grating

A hybrid grating (HG) consists of a subwavelength grating layer and an un-patterned high refractive-index cap layer, being surrounded by low refractive-index materials. It can be seen as a HCG with an additional high refractive-index layer as shown schematically in Fig. 3.7. The name hybrid grating is chosen, since it may comprise two different materials, e.g. Si for the grating and InP for the cap layer. It should be mentioned that Magnusson has independently reported similar structure in Ref. [34], and referred to it as zero-contrast grating. In this section, the physics of HG as a bordabnd reflector and high Q-factor resonator is investigated. Since we are interested in employing HG in a hybrid III-V on SOI laser, it is assumed that the cap layer is made of InP and a silicon grating is patterned on the SiO_2 substrate, and the HG is excited from superstrate made of air with a TM-polarized light.

3.3.1 Hybrid Grating as a Broadband Reflector

Figures 3.8(a) and 3.8(b) show simulated transmissivity contour maps as a function of normalized wavelength λ_0/Λ_g and grating layer thickness t_g/Λ_g for a HCG, or cap layer thickness t_c/Λ_g for a HG, respectively. Here, bright lines which are

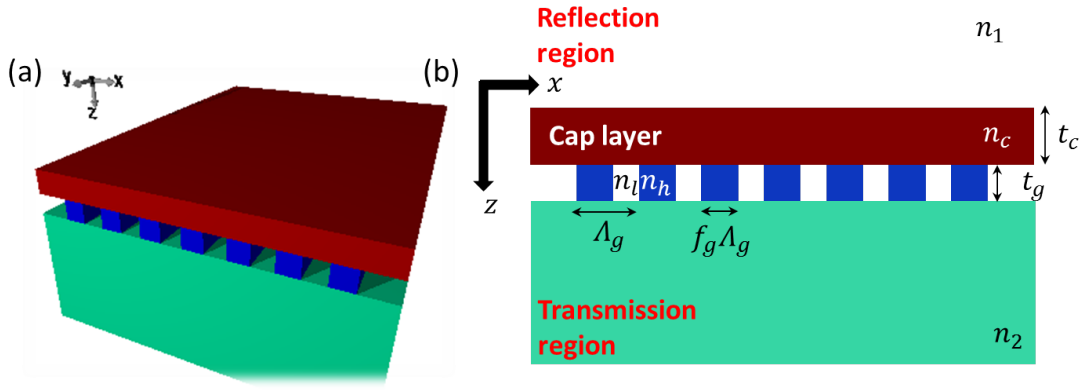

Figure 3.7: (a) Schematic view of a hybrid grating structure. (b) Schematic cross-sectional view of the hybrid grating with its parameter definitions. Refractive-indices used for simulations of this section are based on an InP cap layer with a silicon grating on SiO_2 substrate excited from air superstrate; n_h=3.48, n_l=1, n_1=1, n_2=1.48, and n_c=3.166.

transmissivity dips, correspond to GMRs. In the HCG case, i.e. Fig. 3.8(a), more guided-modes are introduced as the grating layer thickness is increased, which result in a larger number of GMRs. The same trend is observed for the HG case, i.e. Fig. 3.8(b), as the cap layer thickness is increased while the grating layer thickness is fixed. A difference between the HG and the HCG structure is that for the HG structure good overlaps between different modes can be provided due to cap layer: In the HCG structure, only two nearby band-edge modes overlap while others are well separated. As a result, a broader high-reflectivity is obtained in the HG case than in the HCG case as shown in Figs. 3.8(c) and 3.8(d).

Similar to the HCG case, the HG can be seen as a coupled waveguide-array and only propagating modes in the layers participate in the reflection process [8]. The SFG of HG in the dual-mode regime is shown in Fig. 3.9. There are two propagating modes in the grating, several (three or five) propagating modes in the cap layer, and a propagating mode outside the HG structure. In homogeneous layers, e.g. cap layer, each mode corresponds to a single spatial harmonic (or diffracted beam), as it was explained previously. So in the input and output media, the only propagating mode corresponds to 0-th harmonic (0-th order diffracted beam) and for the cap layer due to the higher refractive-index the three propagating modes correspond to 0-th and ±1-st harmonics. Note that the ±1-st harmonics interact with the two waveguide-array modes in the grating layer, but not with the 0-th harmonic in the air. Thus, it is expected that most of the power coupled from the waveguide-array modes in the grating layer to the ±1-st harmonics is returned to the waveguide-array modes with some phase change, not escaping from the HG

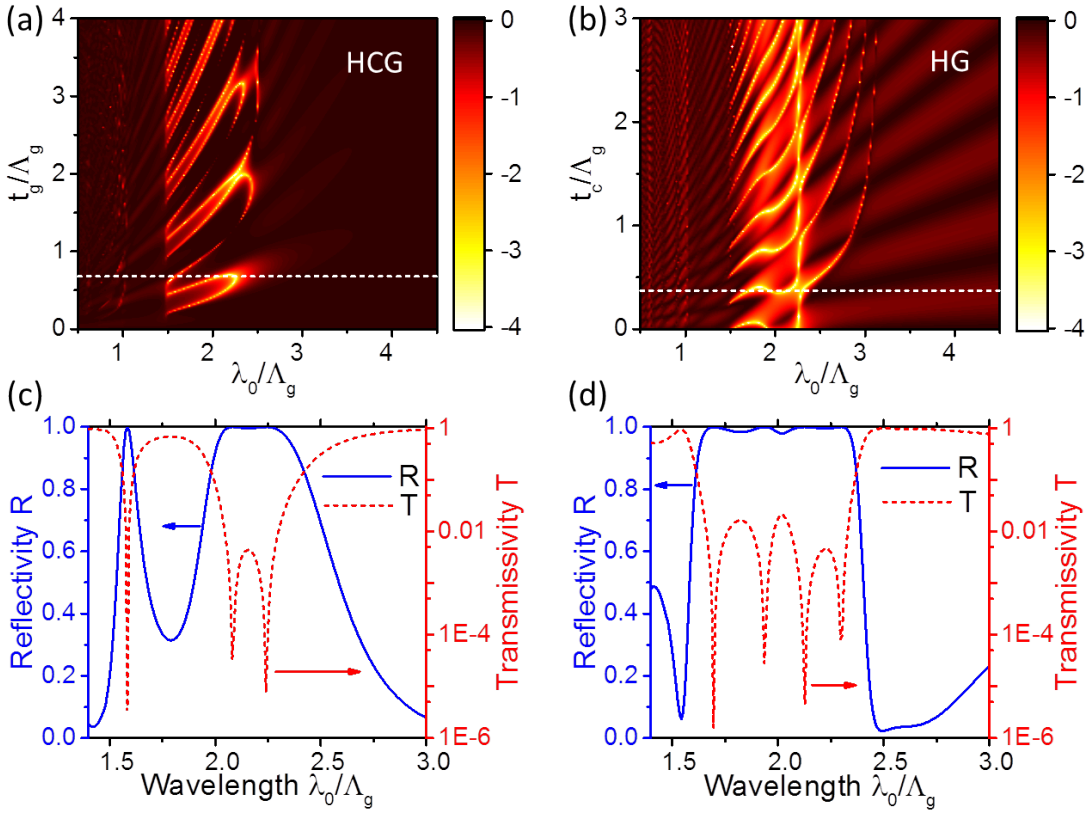

Figure 3.8: Contour plot of transmissivity (color scale) in dB as a function of normalized wavelength λ_0/Λ_g and (a) normalized grating thickness t_g/Λ_g with no cap layer (t_c=0), (b) normalized cap layer thickness t_c/Λ_g with constant grating thickness of t_g/Λ_g=0.62. The white dashed line shows the selected grating thickness and selected cap layer thickness for reflectivity and transmissivity spectra considered in (c) and (d), respectively. Reflectivity in linear scale (blue solid-lines) and transmissivity in dB scale (red dashed-lines) spectra of (c) HCG structure with f_g=0.45 and t_g/Λ_g=0.68, and (d) HG structure with f_g=0.45, t_g/Λ_g=0.62 and t_c/Λ_g=0.37. All refractive indices are defined in Fig. 3.7 caption.

structure. From this arguing, it is qualitatively understandable that adding the cap layer introduces change in GMR wavelengths but not in peak reflectivity [8].

Considering only the propagating modes in the different layers, the reflectivity spectrum of the HG can be reconstructed with a good approximation to rigorous FMM result. Firstly, as illustrated in Fig. 3.10(a), all evanescent modes with an imaginary propagation constant are discarded in all layers. This simplifies the scattering matrices $\mathbf{r}_1$ and $\mathbf{r}_2$ at the interfaces and the propagation matrix $\exp(-j2\beta t_c)$. Using these simplified matrices, the reflectivity, $\mathbf{r}_{eq}$ from the HG can be found from a matrix version of the well-known reflectivity formula for two interfaces, as illustrated in Fig. 3.10(b).

$$\mathbf{r}_{eq} = \left[\mathbf{r}_1 + \mathbf{r}_2 \exp(-j2\beta t_c)\right]\left[\mathbf{I} + \mathbf{r}_1\mathbf{r}_2 \exp(-j2\beta t_c)\right]^{-1} \tag{3.3}$$

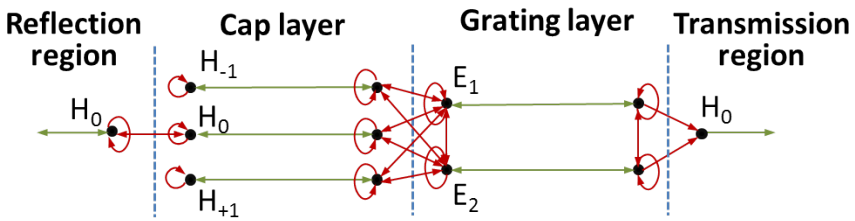

Figure 3.9: Signal flow graph of an HG in dual-mode regime. More explanation about this graph is provided in the caption of Fig. 3.5.

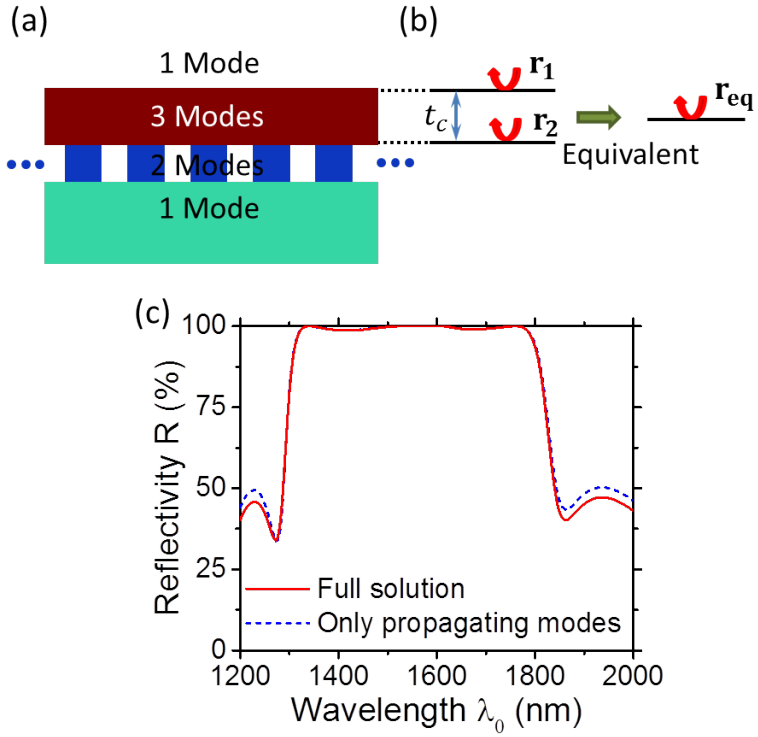

Figure 3.10: (a) Schematic cross-sectional view of the HG with considered modes in each layer. (b) The equivalent reflectivity from the two interface of the cap layer and grating. (c) Calculated reflectivity spectrum of an HG structure using full solution (red solid-line) and with discarding non-propagating modes (blue dashed-line). It shows a very good agreement especially in the wavelength region with high reflectivity.

where **I** represents a unity matrix. In Fig. 3.10(c), the reflectivity spectrum obtained by this semi-analytic approach is compared with the rigorous solution, showing a good agreement, especially in the high-reflectivity region. This supports the explanation that high reflectivity value and its broadband nature depends mainly on propagating modes.

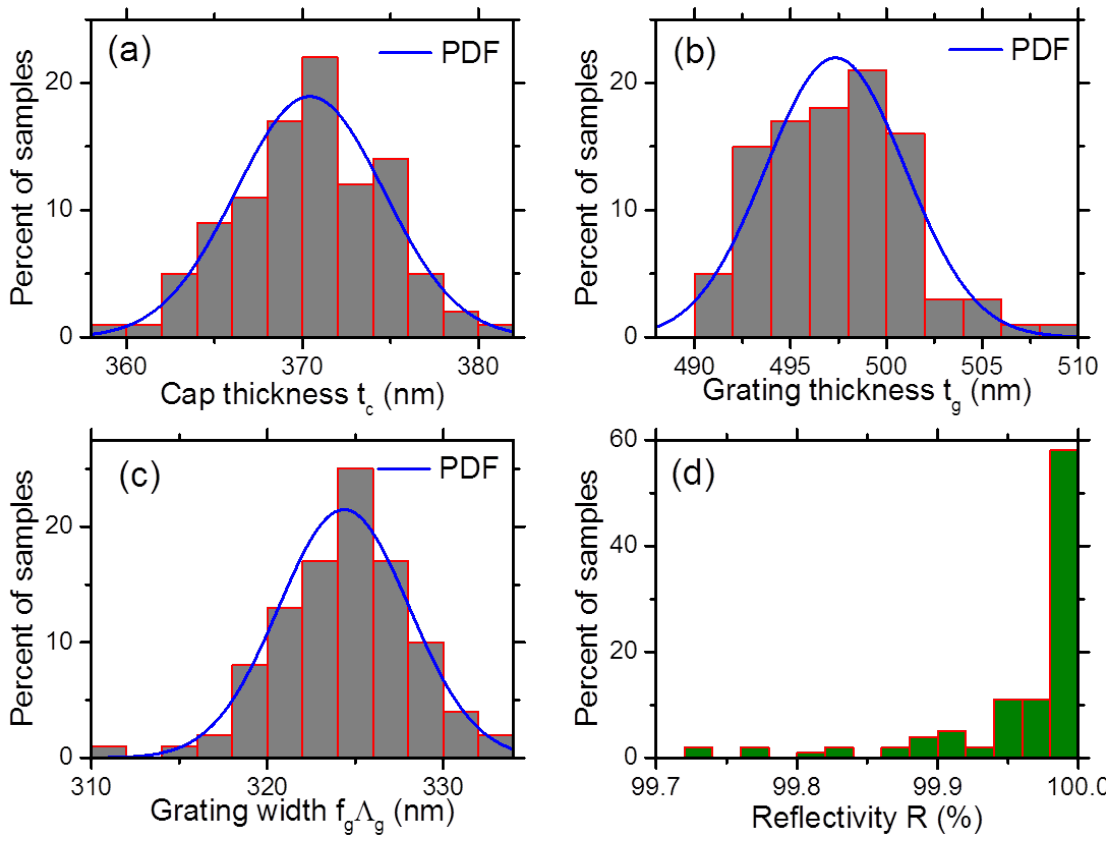

Figure 3.11: Monte Carlo analysis of fabrication tolerance in an example HG structure. The designed parameters are Λ_g=720 nm, t_g=497 nm, f_g=0.45, t_c=370 nm n_h=3.48, n_l=1.0, n_1=1.0, n_2=1.0 and n_c=3.166. Distributions of (a) grating thickness, (b) duty cycle, (c) cap layer thickness. and (d) resulting Q-factor distribution.

Fabrication Tolerances

The HG reflector has good tolerance to fabrication errors. During fabrication steps including epitaxy growth, cap layer thickness, t_c, grating thickness, t_g, and grating width, $W_g = f_g\Lambda_g$ may have ± 10 nm variations from designed values. Grating period, Λ_g can be relatively accurately defined. To estimate the effect of fabrication variations in t_c, t_g, and $f_g\Lambda_g$ on reflectivity, Monte Carlo analysis is performed. In this analysis, 100 samples each with different t_c, t_g, and W_g values are chosen. Each parameter value is chosen to un-correlated to each other and to have a normal distribution with a probability density function of $f(x) = \frac{1}{\sigma\sqrt{2\pi}} \exp(-\frac{(x-x_0)^2}{2\sigma^2})$, where x_0 is the value of designed parameter and 3σ is the fabrication error. I have assumed $\sigma = 4$ nm which corresponds to ±12 nm error. Figures 3.11(a), 3.11(b), and 3.11(c) show the histogram distribution of each parameter in the 100 samples chosen for a designed HG structure. Monte Carlo analysis result presented in Fig. 3.11(d) shows that all HG samples have reflectivity above 99.7%, indicating the HG is tolerable to most of probable fabrication errors.

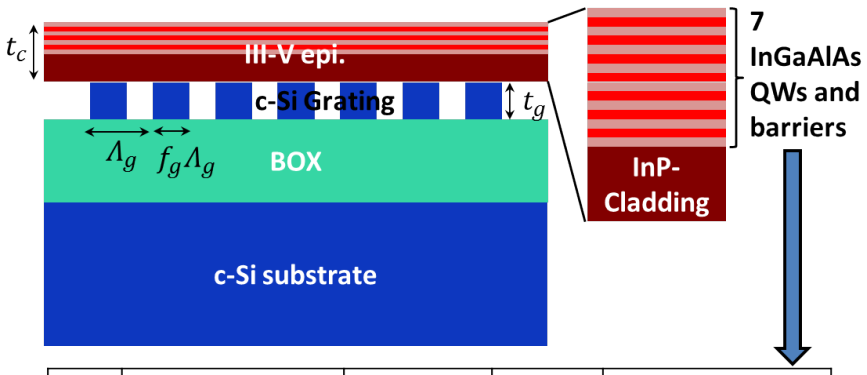

No.	Material	Thickness	Repeat	Refractive index
1	InGaAlAs-Barrier	7.5 nm	1	3.583
2	InGaAlAs-QW	6.5 nm	7	3.583
3	InGaAlAs-Barrier	7.5 nm	7	3.583
4	InP-Cladding	191.7	1	3.1661

Figure 3.12: Schematic of the designed hybrid grating structure made of a Si grating with III-V epitaxial layer as a cap layer. The III-V epitaxy contains 7 quantum wells with barriers (layer thicknesses are provided in the table), since it was planned to use as the bottom reflector in a VCSEL structure. Si grating parameters are Λ_g=720 nm, t_g=492 nm and f_g=0.5.

3.3.2 Experimental Results

To verify the capability of hybrid grating as a broadband reflector, it was fabricated by my colleague using DTU Danchip facility and its reflectivity spectrum was measured. Since we had a plan to use this structure as the bottom mirror in a VCSEL structure (it will be explained with details in the next chapter), the designed structure has a epitaxial-grown structure which contains several quantum wells as active region. The grating is formed on a SOI wafer using electron-beam lithography. Then a direct wafer bonding process is used for hybridizing the III-V active layer onto the SOI wafer and make the structure [35]. Since the III-V epitaxial structure contains several additional layers which are not required for the optimized HG reflector design, they are removed using wet-etching process [36]. Figure 3.12 shows the cross-sectional view of the III-V epitaxy with detailed layer thicknesses after it was processed for the HG. It should be noted that for using this HG in the VCSEL, the light is incident from SiO_2 medium. However, here air is used as the superstrate medium which results in a drop in the reflectivity value compared to the designed case.

A scanning electron microscope (SEM) image of the fabricated device is illustrated in the Fig. 3.13(a). A supercontinuum laser source (SuperK EXTREME

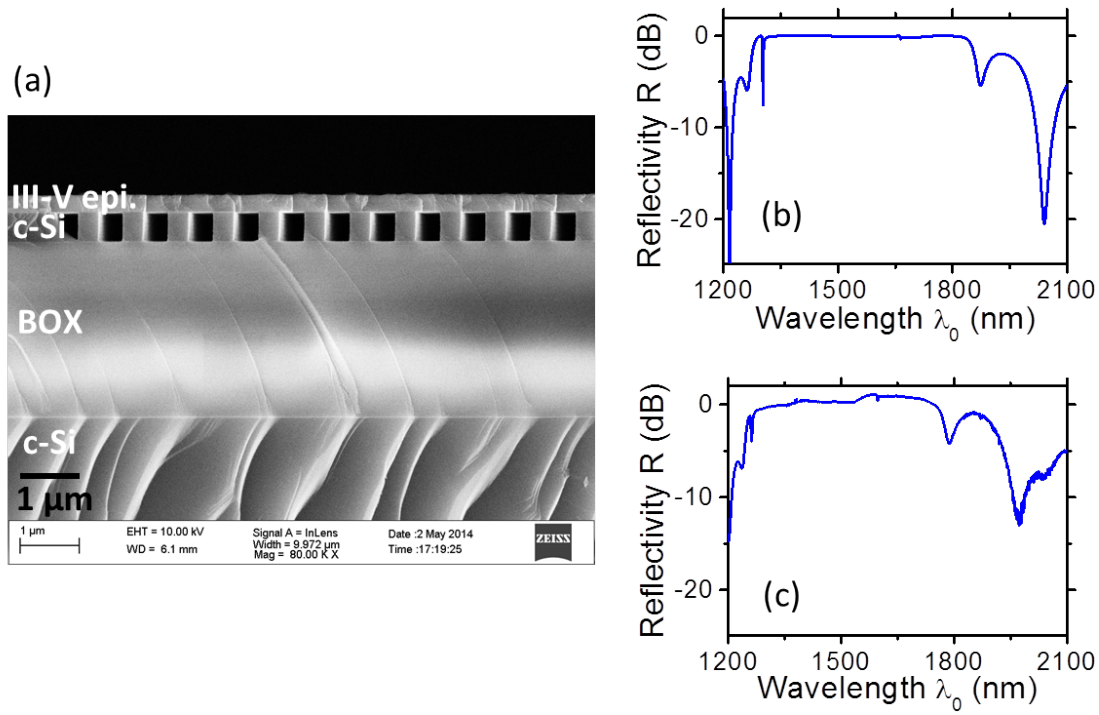

Figure 3.13: (a) SEM image of the fabricated hybrid grating structure. (b) Simulated reflectivity spectrum of the designed HG structure for TM-polarized light at 3.5 degree angle. (c) Measured reflectivity spectrum of the fabricated HG for TM-polarized light at 3.5 degree angle of incidence [36]. The measured data are not exact reflectivity, since they require calibration. There is a good agreement in the spectrum shape and position of the dips.

supercontinuum laser) is used for illuminating the fabricated device and the reflected light is gathered and analyzed by an optical spectrum analyzer (OSA) (AQ6375 Yokogawa). A polarizer is used to make the TM-polarized light and photonic crystal fibers are used for connections due to their capability to maintain the polarization state. Due to the measurement set-up limitations, it was not possible to measure the reflectivity at the normal incident angle and it was measured at 3.5 degree angle. The reflectivity spectrum predicted by theory and the measured one are shown in Figs. 3.13(b) and 3.13(c), respectively. In our measurement set-up, it is difficult to measure the exact reflectivity value, and it was measured compared to a reference gold mirror. Therefore, when the reflectivity is higher than 1, it means hybrid grating reflectivity value is larger than the gold mirror. By comparing the simulation and measured results, we can conclude that there is a good agreement in the shape of reflectivity spectrum and also the position of reflectivity dips. This illustrates the feasibility of the hybrid grating as a broadband reflector.

3.3.3 Hybrid Grating as a High Q-Factor Resonator

Similar to the HCG case, we may expect that HG also has high Q-factor resonances which can be found close to the anti-crossing point in the reflectivity contour maps [9]. Therefore, the reflectivity contour maps of a HG as a function of λ_0/Λ_g and t_g/Λ_g are plotted in Figs. 3.14(a) and 3.14(b) for two different cap layer thicknesses. Results look similar to the simulation results obtained for HCGs. The checker-board pattern seen in these contour maps reflects the interference between several waveguide-array modes and is similar to the HCG case as it was explained in the previous section. The single- and dual-mode regimes in Fig. 3.14(a) denote the wavelength ranges with one and two propagating modes in the grating layer, respectively. Some of the *candidate* points for high Q-factor resonances are indicated by magenta circles in Fig. 3.14.

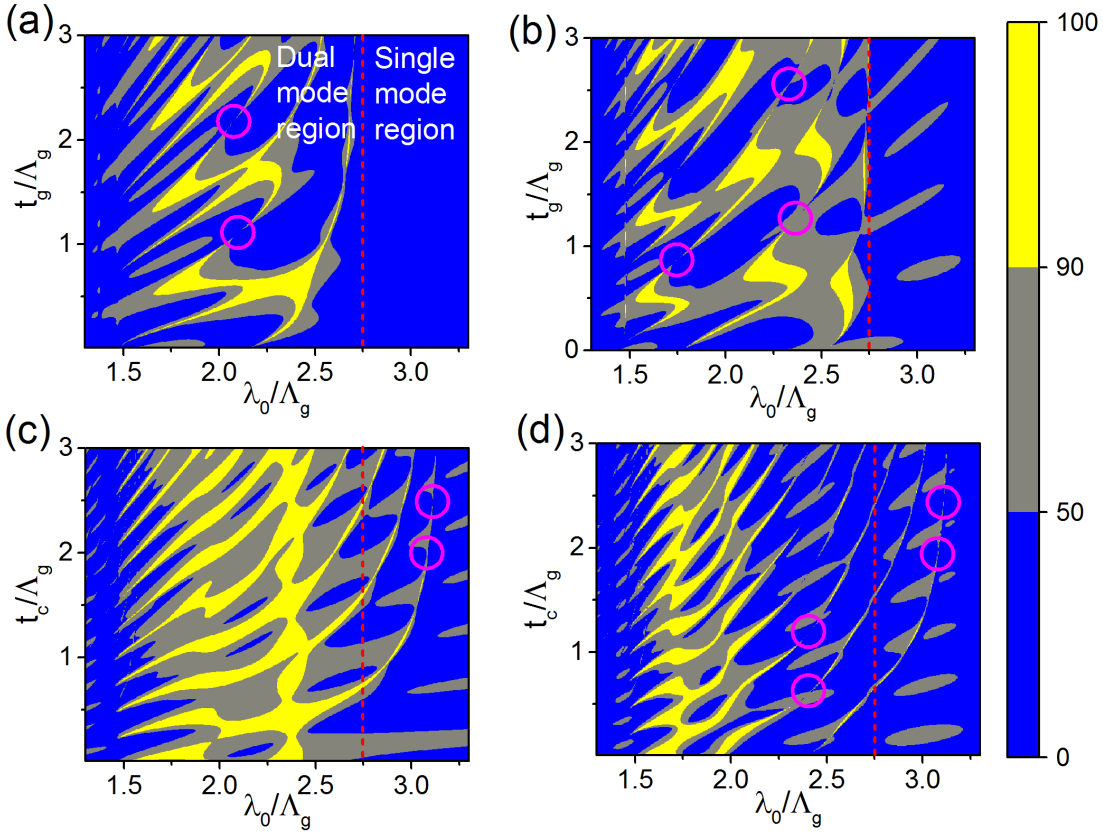

Figure 3.14: Contour maps of the reflectivity (color scale) versus normalized wavelength and grating thickness (a,b) or normalized wavelength and cap thickness (c,d) at f_g=0.50 for TM-polarized light. (a) t_c/Λ_g=0.4, (b) t_c/Λ_g=0.6, (c) t_g/Λ_g=0.6, (d) t_g/Λ_g=1.35. Only three color levels are used. Dimensions are defined in Fig. 3.7 caption and refractive indices are also provided there.

In order to discuss the influence of the cap layer thickness t_c, two reflectivity contour maps as a function of λ_0/Λ_g and t_c/Λ_g for two values of t_g are plotted in Figs. 3.14(c) and 3.14(d). High reflectivity lines extend into the single-mode regime, while they are found only within the dual-mode regime in Figs. 3.14(a) and 3.14(b). Candidate points for resonances are found in both regimes. Note that the resonances found in different regimes have different origins and properties. The resonances observed in the single mode regime, henceforth referred to as type-I resonances, have the same physical origin as the resonances found in conventional GMR-based filters [11]. This type-I resonance is due to the constructive interference of the diffraction orders +1 and -1 in *the cap layer* with total internal reflection at the (air)-(cap layer) interface. Its characteristic feature is that at normal incidence, the diffraction orders +1 and -1 result in two resonance peaks degenerate at the same wavelength in the reflectivity spectrum, but for a finite angle of incidence the peaks will separate spectrally [11]. This resonance type is also found in conventional shallow etched grating structures. It typically has a low Q-factor because the diffraction orders +1 and -1 inside the cap layer result in the appearance of diffraction order 0 when reflected again from the grating and the 0-th order component is lossy at the (air)-(cap layer) interface.

The resonances found only in the dual mode regime, are the main focus of this section, are referred to as type-II resonances, and have a different origin and different properties. As explained below in detail, they originate from the constructive interference of two waveguide-array modes in *the grating layer*. Since this constructive interference condition requires a certain grating thickness, the type-II resonance is sensitive to the grating thickness while the type-I resonance is not. Type-II resonances may have much higher Q-factor than type-I. Furthermore, a type-II resonance peak in the reflection spectrum at normal incidence does not separate into two peaks but shifts with a small incidence angle. Type-II resonances are not observed in conventional GMR-based grating filters.

As shown in Fig. 3.15(a), the Q-factor of a type-II resonance is very sensitive to small changes in HG parameters, while its resonance wavelength is relatively insensitive and just linearly increases with the grating layer thickness. Thus, after finding several high Q-factor candidate parameter sets from a coarse scanning of parameters, several runs using particle swarm optimization (PSO) technique [37] were performed around each candidate set to find the local solution that gives the highest possible Q-factor. Without resorting to the use of PSO, very fine-resolution scan are required due to the sensitiveness of the Q-factor, demanding significant computational efforts.

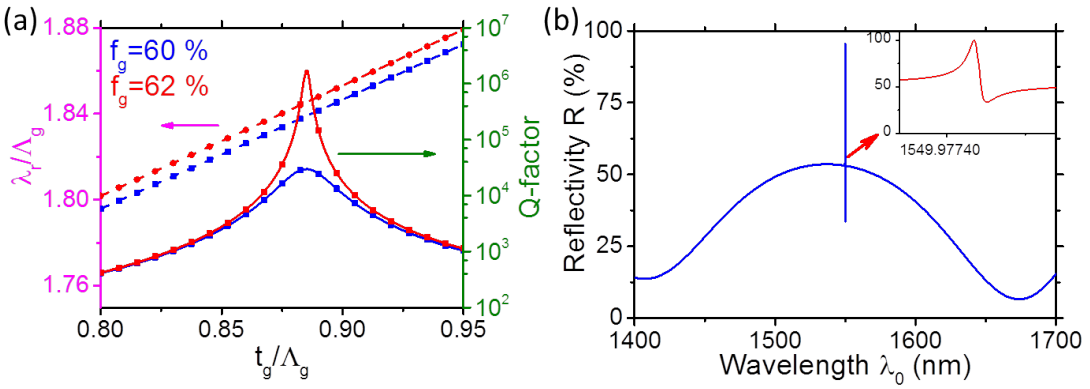

Figure 3.15: (a) Resonance wavelength λ_r (dashed lines) and Q-factor (solid lines) as a function of grating thickness around a candidate point for resonance at two values of the duty cycle, f_g=60 % (blue lines) and f_g=62 % (red lines). The Q-factor depends sensitively on the structure parameters. (b) Reflectivity spectrum for TM-polarized light of an HG structure with ultrahigh Q-factor found by PSO with Λ_g=853.5 nm, t_g=742.3 nm, f_g=0.616, t_c=830.5 nm.

Using PSO, several designs are identified that result in ultra-high Q-factors. Figure 3.15(b) shows an example of the reflectivity spectrum for an optimal structure with a Q-factor of 1.12×10^9. The structure dimensions are specified in the caption and scaled to have a resonance at telecommunication wavelength of 1550 nm. This type-II resonance is of the Fano type [38], which means that the resonance occurs as a result of the interference of discrete modes in the HG structure with continuous modes outside the structure. Note that as shown in the inset of Fig. 3.15(b), this resonance reaches 100% reflectivity but not 100% transmissivity. The reason is that the HG structure inherently does not possess mirror symmetry along the z-direction, which results in different decay rates of the electromagnetic energy stored in the HG structure into input and output regions [38]. In contrast, HCG resonators suspended in air have mirror symmetry and the reflectivity varies from 100% to 0% around a resonance peak [5], [26].

Figure 3.16(a) shows the field profile of this high Q-factor resonance excited by a TM-polarized plane wave incident from the air side. The field is strongly enhanced in the cap layer as well as in the grating layer. To get insight into the field confinement properties of the structure, I have plotted the field strength of different spatial harmonics in Fig. 3.16(b). As described in the previous section, these spatial harmonics are the Bloch modes in the cap layer. But for the grating layer, the harmonics contributions from waveguide-array modes are added together to plot this figure. It is noteworthy in Fig. 3.16(b) that the field in the cap layer mainly contains the 1-st spatial harmonic component, while the grating layer contains the

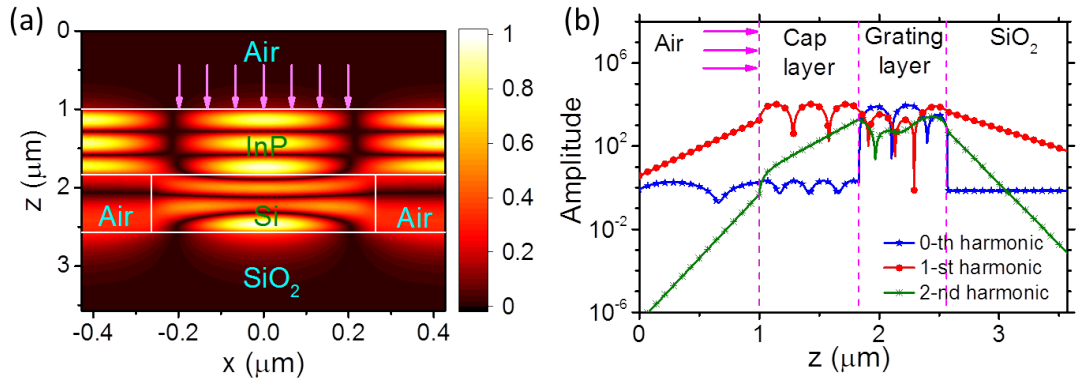

Figure 3.16: (a) Normalized magnetic field profile $|H_y|$ for the HG structure of Fig. 3.7, excited by an incident plane wave with the same wavelength as the resonance wavelength found in Fig. 3.15(b). (b) Amplitudes of the magnetic modal fields in dB scale for 0-th, 1-st and 2-nd spatial harmonic inside all the layers at the resonance wavelength. TM-polarized light is incident from the left.

0-th and 2-nd spatial harmonics as well. This observation is a clue to understanding how such a high Q-factor resonance appears in the HG structure.

As it was mentioned in the previous section, SFG shows how the propagating waves interact with each other. For a high Q-factor Type-II resonance, the SFG is similar to the HG as a broadband reflector case and is shown in Fig. 3.9. At the (cap layer)-(grating layer) interface, the excitation of H_0 is very small since the coupling from E_1 and E_2 to H_0, and the self-coupling to H_0 cancel each another at the interface. As a result, the loss at the (air)-(cap layer) interface H_0 is very small as it is clear from Fig. 3.16(b). However, the couplings to $H_{\pm 1}$ do not cancel efficiently, resulting in strong excitation of the first harmonic component in the cap layer. At the (grating layer)-(SiO_2) interface, the 0-th harmonic components of E_1 and E_2 cancel each other, resulting in very small coupling to H_0 in the SiO_2 layer. As shown in the (air)-(cap layer) and (grating layer)-(SiO_2) interfaces, the only loss channel from the HG resonator to the input and output media is through H_0, since other higher-order harmonics become evanescent due to the subwavelength periodicity. Thus, the overall loss becomes very small, which explains the observation of very high Q-factors.

Fabrication Tolerances and Finite Size Effect

We are interested in applications of HG resonator structure as a laser with a moderate Q-factor and a size of 10 to 15 μm and would estimate the effect of fabrication-related deviations of geometrical parameters from the designed values, on the Q-factor. For this estimation, Monte Carlo analysis is employed, assuming that within this length scale of 10 to 15 μm, the fabrication-related deviations of the

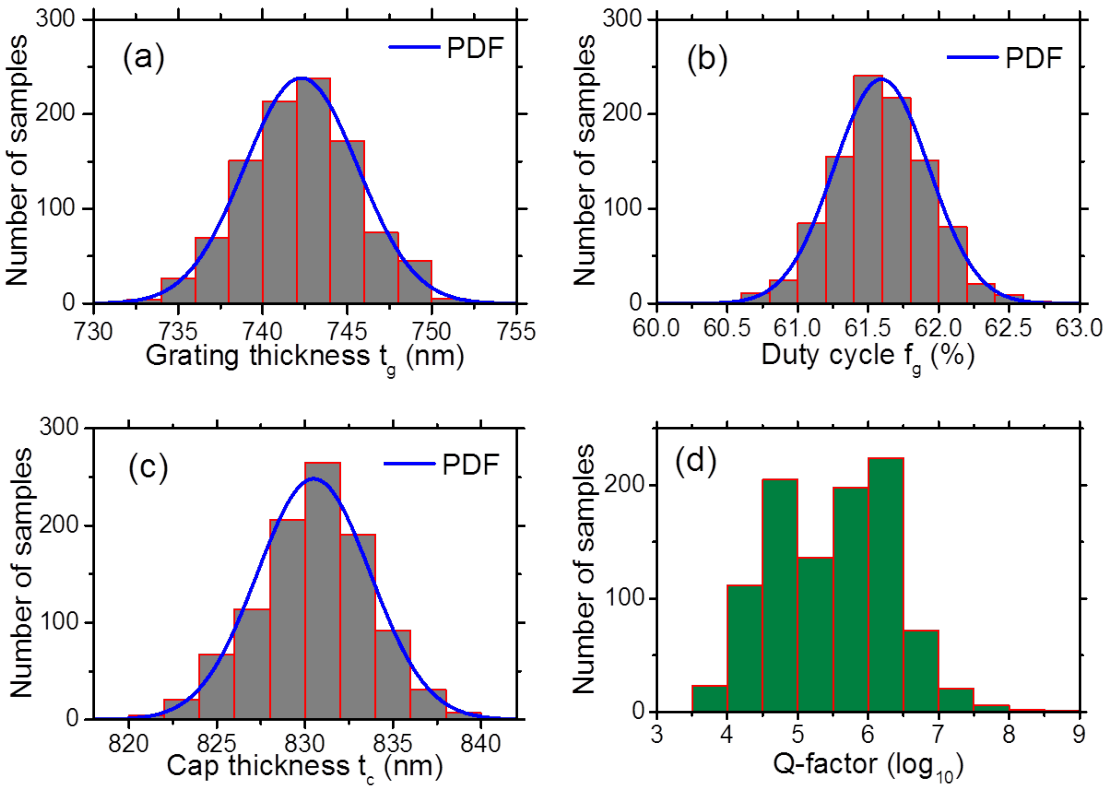

Figure 3.17: Monte Carlo analysis of fabrication tolerance for a hybrid grating. Distributions of (a) grating thickness, (b) duty cycle, (c) cap layer thickness. and (d) resulting Q-factor distribution.

grating period and bar width are not completely random, rather locally synchronized. In this analysis method, simulations are performed for a large number of parameters, which are chosen from a Gaussian probability distribution and the results are aggregated. As shown in Figs. 3.17(a) to 3.17(c), variations in grating thickness, duty cycle, and cap layer thickness are analyzed. The variations are assumed to be ±10 nm for the cap layer and grating layer thickness and ±1% for the duty cycle, i.e., ±8 nm for the grating bar width. These fabrication errors often occur in epitaxial growth and e-beam lithography with an image transfer to a hard mask followed by dry etching. A total of 1000 simulations is performed, each one being referred to as a sample. The Q-factor distribution in Fig. 3.17(d) shows that all simulated structures have Q-factors higher than 6000 and 98% of the samples have Q-factors above 10^4, which is sufficiently high for laser applications of our interest.

In a real HG resonator with a finite number of periods and finite length of grating bars, the lateral loss from the end of the grating bars will reduce the Q-factor. This reduction is estimated by performing a 3D simulation. The simulated structure has 21 grating bars in the x-direction, is 12 μm long in the y-direction and is truncated with air outside. The field profile is shown in Fig. 3.18 and the measured Q-factor

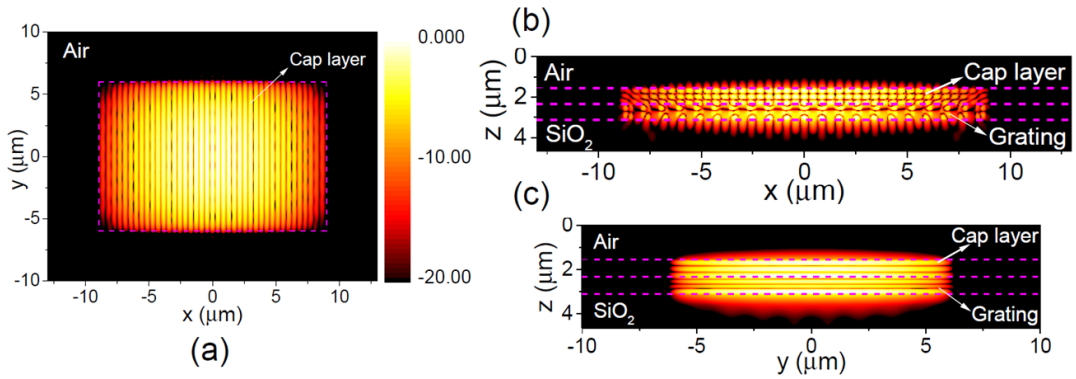

Figure 3.18: Normalized mode profiles $|H_y|$ in dB of an HG resonance in (a) x-y plane in the cap layer, (b) x-z plane, and (c) y-z plane.

is 12000. It is observed in plots with finer details that the scattering loss causing the reduction in Q-factor occurs mostly downwards into SiO_2 layer. The observed Q-factor is acceptable for most laser diode designs. It is also similar to the value obtained for HCG-based resonators [5]. This Q-factor can be considerably increased by simply increasing the size of the structure or introducing heterostructures in the grating in both x- and y-directions. Also, we expect that similar to photonic crystal surface-emitting lasers [39], it should be possible to design the resonator with enhanced radiation power in specific direction.

3.4 Summary

In summary, this chapter has discussed the physics of subwavelength grating structures with high refractive-index contrast between the grating bar and materials surround it. Two equivalent physical pictures have been employed to understand the working mechanism of these structures; guided-mode resonance picture and waveguide-array picture. Firstly, these two pictures have been used to explain the properties of high-index-contrast grating (HCG) as a broadband reflector and also standalone high Q-factor resonator. Next the proposed hybrid grating (HG), that consists of a subwavelength grating layer and an unpatterned high refractive-index cap layer, is investigated thoroughly. Numerical simulations show that the HG reflector has a near-unity reflectivity in a broad bandwidth, surpassing that of a conventional HCG. It has been revealed that the cap layer introduces more GMRs without loss of peak reflectivity leading to this broader high-reflectivity bandwidth. We have also shown that this broadband reflection properties originate mainly from propagating modes within the structure. The fabrication and characterization of a HG sample shows the feasibility of this structure. Furthermore, we have shown

that HG structure can work also as a high Q-factor resonator and analyzed the origin of the high-Q resonances. We have found that the cancellation of the 0-th spatial harmonic of two propagating modes of the grating layer at the interfaces to surrounding layers leads to high-Q resonances, which is similar to the resonances appearing in HCG resonators. Given typical fabrication errors and finite extension of 10 to 15 μm, the Q-factor of a HG resonator drops from a ultrahigh value to a moderate value that is still sufficient for laser diode applications.

References

[1] T. Gu, A. Andryieuski, Y. Hao, Y. Li, J. Hone, C. W. Wong, A. Lavrinenko, T. Low, and T. F. Heinz, "Photonic and plasmonic guided modes in graphene-silicon photonic crystals", *ACS Photonics*, vol. 2, no. 11, pp. 1552–1558, 2015. arXiv: 1504.04911 (cit. on p. 58).

[2] V. Karagodsky and C. J. Chang-Hasnain, "Physics of near-wavelength high contrast gratings", *Optics Express*, vol. 20, no. 10, pp. 10 888–10 895, 2012 (cit. on pp. 59–61, 65).

[3] C. Mateus, M. Huang, Y. Deng, A. Neureuther, and C. Chang-Hasnain, "Ultrabroadband mirror using low-index cladded subwavelength grating", *IEEE Photonics Technology Letters*, vol. 16, no. 2, pp. 518–520, 2004 (cit. on pp. 59, 62).

[4] C. Mateus, M. Huang, L. Chen, C. Chang-Hasnain, and Y. Suzuki, "Broad-band mirror (1.12–1.62 um) using a subwavelength grating", *IEEE Photonics Technology Letters*, vol. 16, no. 7, pp. 1676–1678, 2004 (cit. on pp. 59, 62).

[5] Y. Zhou, M. Moewe, J. Kern, M. C. Huang, and C. J. Chang-Hasnain, "Surface-normal emission of a high-Q resonator using a subwavelength high-contrast grating", *Optics Express*, vol. 16, no. 22, pp. 17 282–17 287, 2008 (cit. on pp. 59, 62, 65, 75, 78).

[6] T. T. Wu, S. H. Wu, T. C. Lu, and S. C. Wang, "GaN-based high contrast grating surface-emitting lasers", *Applied Physics Letters*, vol. 102, no. 8, p. 081 111, 2013 (cit. on pp. 59, 62, 65).

[7] C. J. Chang-Hasnain and W. Yang, "High-contrast gratings for integrated optoelectronics", *Advances in Optics and Photonics*, vol. 4, no. 3, pp. 379–440, 2012 (cit. on p. 59).

[8] A. Taghizadeh, G. C. Park, J. Mork, and I.-S. Chung, "Hybrid grating reflector with high reflectivity and broad bandwidth", *Optics Express*, vol. 22, no. 18, pp. 21 175–21 184, 2014 (cit. on pp. 59, 60, 67, 68).

[9] A. Taghizadeh, J. Mork, and I.-S. Chung, "Ultracompact resonator with high quality-factor based on a hybrid grating structure", *Optics Express*, vol. 23, no. 11, pp. 14 913–14 921, 2015 (cit. on pp. 59, 73).

[10] S. Peng, T. Tamir, and H. Bertoni, "Theory of periodic dielect waveguides", *IEEE Transactions on Microwave Theory and Techniques*, vol. 23, no. 1, pp. 123–133, 1975 (cit. on pp. 59, 60).

[11] S. S. Wang and R. Magnusson, "Theory and applications of guided-mode resonance filters", *Applied Optics*, vol. 32, no. 14, pp. 2606–2613, 1993 (cit. on pp. 60, 61, 74).

[12] R. Magnusson and M. Shokooh-Saremi, "Physical basis for wideband resonant reflectors", *Optics Express*, vol. 16, no. 5, pp. 3456–3462, 2008 (cit. on pp. 60, 65).

[13] V. Karagodsky, F. G. Sedgwick, and C. J. Chang-Hasnain, "Theoretical analysis of subwavelength high contrast grating reflectors", *Optics Express*, vol. 18, no. 16, pp. 16 973–16 988, 2010 (cit. on pp. 60–62, 64).

[14] S. Tibuleac and R. Magnusson, "Reflection and transmission guided-mode resonance filters", *Journal of the Optical Society of America A*, vol. 14, no. 7, pp. 1617–1626, 1997 (cit. on pp. 60, 61).

[15] Z. S. Liu and R. Magnusson, "Concept of multiorder multimode resonant optical filters", *IEEE Photonics Technology Letters*, vol. 14, no. 8, pp. 1091–1093, 2002 (cit. on p. 60).

[16] D. Rosenblatt, A. Sharon, and A. Friesem, "Resonant grating waveguide structures", *IEEE Journal of Quantum Electronics*, vol. 33, no. 11, pp. 2038–2059, 1997 (cit. on p. 60).

[17] M. C. Huang, Y. Zhou, and C. J. Chang-Hasnain, "A surface-emitting laser incorporating a high-index-contrast subwavelength grating", *Nature Photonics*, vol. 1, no. 5, pp. 297–297, 2007 (cit. on p. 62).

[18] S. Boutami, B. Benbakir, J.-L. Leclercq, and P. Viktorovitch, "Compact and polarization controlled 1.55 um vertical-cavity surface-emitting laser using single-layer photonic crystal mirror", *Applied Physics Letters*, vol. 91, no. 7, p. 071 105, 2007 (cit. on p. 62).

[19] M. C. Y. Huang, Y. Zhou, and C. J. Chang-Hasnain, "A nanoelectromechanical tunable laser", *Nature Photonics*, vol. 2, no. 3, pp. 180–184, 2008 (cit. on p. 62).

[20] I.-S. Chung and J. Mork, "Silicon-photonics light source realized by III–V/Si-grating-mirror laser", *Applied Physics Letters*, vol. 97, no. 15, p. 151 113, 2010 (cit. on p. 62).

[21] I.-S. Chung, J. Mork, P. Gilet, and A. Chelnokov, "Subwavelength grating-mirror VCSEL with a thin oxide gap", *IEEE Photonics Technology Letters*, vol. 20, no. 2, pp. 105–107, 2008 (cit. on p. 62).

[22] I.-S. Chung, V. Iakovlev, A. Sirbu, A. Mereuta, A. Caliman, E. Kapon, and J. Mork, "Broadband MEMS-tunable high-index-contrast subwavelength grating long-wavelength VCSEL", *IEEE Journal of Quantum Electronics*, vol. 46, no. 9, pp. 1245–1253, 2010 (cit. on p. 62).

[23] C. Sciancalepore, B. B. Bakir, X. Letartre, J. Harduin, N. Olivier, C. Seassal, J.-M. Fedeli, and P. Viktorovitch, "CMOS-compatible ultra-compact 1.55-um emitting VCSELs using double photonic crystal mirrors", *IEEE Photonics Technology Letters*, vol. 24, no. 6, pp. 455–457, 2012 (cit. on p. 62).

[24] D. Fattal, J. Li, Z. Peng, M. Fiorentino, and R. G. Beausoleil, "Flat dielectric grating reflectors with focusing abilities", *Nature Photonics*, vol. 4, no. 7, pp. 466–470, 2010 (cit. on p. 62).

[25] L. Carletti, R. Malureanu, J. Mork, and I.-S. Chung, "High-index-contrast grating reflector with beam steering ability for the transmitted beam", *Optics Express*, vol. 19, no. 23, pp. 23 567–23 572, 2011 (cit. on p. 62).

[26] V. Karagodsky, C. Chase, and C. J. Chang-Hasnain, "Matrix Fabry–Perot resonance mechanism in high-contrast gratings", *Optics Letters*, vol. 36, no. 9, pp. 1704–1706, 2011 (cit. on pp. 62, 65, 66, 75).

[27] Y. Zhou, V. Karagodsky, B. Pesala, F. G. Sedgwick, and C. J. Chang-Hasnain, "A novel ultra-low loss hollow-core waveguide using subwavelength high-contrast gratings", *Optics Express*, vol. 17, no. 3, pp. 1508–1517, 2009 (cit. on p. 62).

[28] Y. Yue, L. Zhang, X. Wang, H. Huang, W. Yang, J. Ferrara, V. Karagodsky, C. Chase, M. Tur, C. J. Chang-Hasnain, and A. E. Willner, "Three-dimensional chirped high-contrast grating hollow-core waveguide", *IEEE Photonics Journal*, vol. 4, no. 5, pp. 1372–1380, 2012 (cit. on p. 62).

[29] W. Yang, J. Ferrara, K. Grutter, A. Yeh, C. Chase, Y. Yue, A. E. Willner, M. C. Wu, and C. J. Chang-Hasnain, "Low loss hollow-core waveguide on a silicon substrate", *Nanophotonics*, vol. 1, no. 1, pp. 23–29, 2012 (cit. on p. 62).

[30] T. Estruch, F. Pardo, B. Portier, J. Jaeck, S. Derelle, and R. Haidar, "Mason's rule and signal flow graphs applied to subwavelength resonant structures", *Optics Express*, vol. 20, no. 24, pp. 27 155–27 162, 2012 (cit. on p. 64).

[31] B. C. P. Sturmberg, K. B. Dossou, L. C. Botten, R. C. McPhedran, and C. M. de Sterke, "Fano resonances of dielectric gratings: symmetries and broadband filtering", *Optics Express*, vol. 23, no. 24, pp. 1672–1686, 2015 (cit. on p. 65).

[32] M. Shokooh-Saremi and R. Magnusson, "Wideband leaky-mode resonance reflectors: influence of grating profile and sublayers", *Optics Express*, vol. 16, no. 22, pp. 18 249–18 263, 2008 (cit. on p. 65).

[33] H. Wu, L. Huang, Y. Xiao, C. Zhang, S. Li, N. Luo, X. He, and Y. Gao, "A wideband reflector realized by a subwavelength multi-subpart profile grating structure", *Journal of Optics*, vol. 15, no. 3, p. 035 703, 2013 (cit. on p. 65).

[34] R. Magnusson, "Wideband reflectors with zero-contrast gratings", *Optics Letters*, vol. 39, no. 15, pp. 4337–4340, Aug. 2014 (cit. on p. 66).

[35] G. C. Park, W. Xue, A. Taghizadeh, E. Semenova, K. Yvind, J. Mork, and I.-S. Chung, "Hybrid vertical-cavity laser with lateral emission into a silicon waveguide", *Laser & Photonics Reviews*, vol. 9, no. 3, pp. L11–L15, 2015 (cit. on p. 71).

[36] G. C. Park, A. Taghizadeh, and I.-S. Chung, "Hybrid grating reflectors: origin of ultrabroad stopband", *Submitted to Applied Physics Letters*, 2015 (cit. on pp. 71, 72).

[37] M. Shokooh-Saremi and R. Magnusson, "Particle swarm optimization and its application to the design of diffraction grating filters", *Optics Letters*, vol. 32, no. 8, pp. 894–896, 2007 (cit. on p. 74).

[38] K. X. Wang, Z. Yu, S. Sandhu, and S. Fan, "Fundamental bounds on decay rates in asymmetric single-mode optical resonators", *Optics Letters*, vol. 38, no. 2, pp. 100–102, 2013 (cit. on p. 75).

[39] C. Peng, Y. Liang, K. Sakai, S. Iwahashi, and S. Noda, "Coupled-wave analysis for photonic-crystal surface-emitting lasers on air holes with arbitrary sidewalls", *Optics Express*, vol. 19, no. 24, pp. 24 672–24 686, 2011 (cit. on p. 78).

I believe that in every person is a kind of circuit which resonates to intellectual discovery—and the idea is to make that resonance work.

— Carl Sagan

4 Vertical Cavity Structures

Contents

The vertical cavity is a rich platform for fundamental physics studies of light-matter interaction such as cavity quantum electrodynamics (QED) [1], [2] and cavity polaritons [3], [4], as well as various applications including vertical-cavity surface-emitting lasers (VCSELs) [5]–[7], single-photon light sources [8], and silicon integrated on-chip lasers [9]. A vertical cavity is formed by two mirrors arranged vertically as shown schematically in Fig. 4.1. In conventional vertical cavities, distributed Brag reflectors (DBRs) are used as the top and bottom mirrors, which hereafter are referred to as DBR-based vertical cavities. Recently, other types

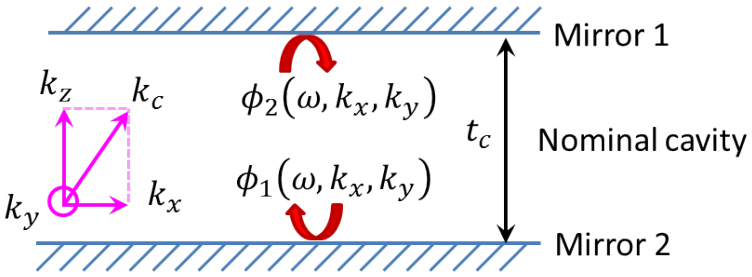

Figure 4.1: Schematic view of a vertical cavity, consists of two mirrors, separated by a nominal cavity with thickness of t_c. The reflectivity phase of two mirrors, ϕ_1 and ϕ_2, depends on the frequency ω and in-plane wavevector components k_x and k_y.

of reflectors using photonic crystal (PhC) structures such as high-index-contrast gratings (HCGs) or hybrid gratings (HGs), are replacing one or even both DBRs, which result in novel functionality and properties for the vertical cavities [9]–[16]. In particular, the dispersion of a vertical cavity, i.e., the relation between the frequency ω and wavevector k of a cavity mode, can be engineered by using the HCG as reflector and designing the dispersion of the HCG [17]–[19]. The dispersion curvature is the second-order derivative of the frequency of a propagating mode with respect to the in-plane wavevector, and its inverse can be interpreted as an effective photon mass along the wavevector direction. As discussed below, the dispersion curvatures along transverse directions can be engineered in vertical cavities with the HCG or HG mirrors to have a specific positive, zero, or negative value. The control of the dispersion characteristics in the cavity may result in various well-known effects such as enhancing the spontaneous emission through the Purcell factor [20] or controlling the properties of polariton lasers [21].

In this chapter, vertical cavity structures with bottom HCG or HG reflector and top DBR as shown schematically in Figs. 4.2(a) and 4.2(b) are investigated numerically. They are referred to as HCG-based or HG-based vertical cavities, respectively. Firstly, the concept of dispersion in vertical cavity is introduced, and several numerical methods for rigorously computing the dispersion are explained with examples. Then, an analytic expression for the cavity dispersion is derived and its accuracy is confirmed by comparing its results with the exact numerics. The dispersion has contributions from the both mirrors and nominal cavity, and it can be engineered by designing the mirror phase response, using HCG or HG reflectors. The effects of dispersion curvature on the mode confinement, mode spacing, and order of transverse modes are investigated. Moreover, the importance of anisotropic dispersion curvatures of the HCG-based cavities along the x- and y-directions is illustrated. The concept of vertical cavity in-plane (VCI) heterostructure is

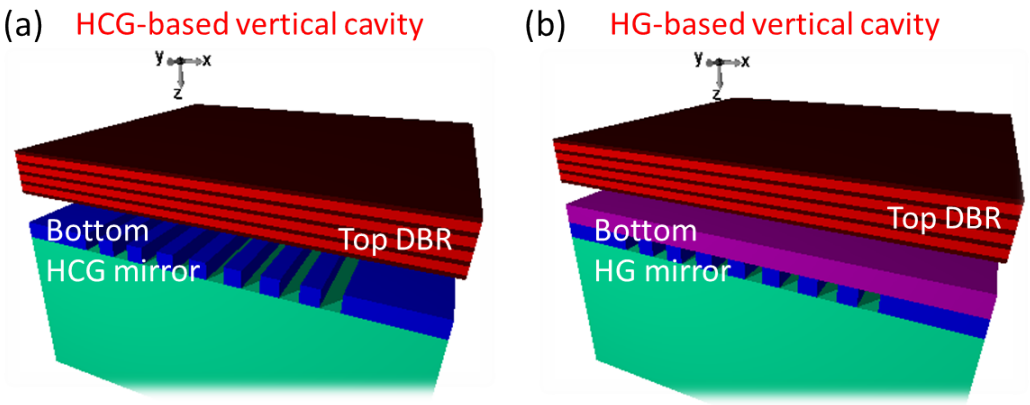

Figure 4.2: Schematic view of a (a) HCG-based, (b) HG-based vertical cavity structure with top DBR and bottom HCG or HG reflector, respectively.

introduced and investigated by numerical simulations. Finally, several interesting HCG/HG-based vertical cavities are designed and simulated such as a HCG-based cavity with very large in-plane emission into a silicon waveguide, an electrically-pumped HG-based cavity with superior thermal properties and a system of two laterally-coupled HCG-based vertical cavities exhibiting parity-time symmetry breaking phenomenon.

4.1 Cavity Dispersion

4.1.1 Calculation Methods

For rigorous calculation of the cavity dispersion in the HCG/HG-based vertical cavities, several different approaches in the Fourier modal method (FMM) are employed and discussed in this section. For all approaches, one period of a HCG/HG-based vertical cavity in Fig. 4.2 is considered for simulations, i.e. it is assumed that there are an infinite number of grating periods in the x-direction and the grating bars are infinity long in the y-direction.

Method I

In 'Method I', the reflectivity or transmissivity spectrum of the cavity is investigated with a plane-wave that is illuminated from the top with a non-zero in-plane wavevector component k_x or k_y, i.e. the plane-wave has an incident angle θ with respect to the normal direction to the grating surface. Figures 4.3(a) and 4.3(b) illustrate the transmissivity contour maps of an exemplary HCG-based cavity versus the wavelength and incident angle in the x- and y-directions, respectively. As it

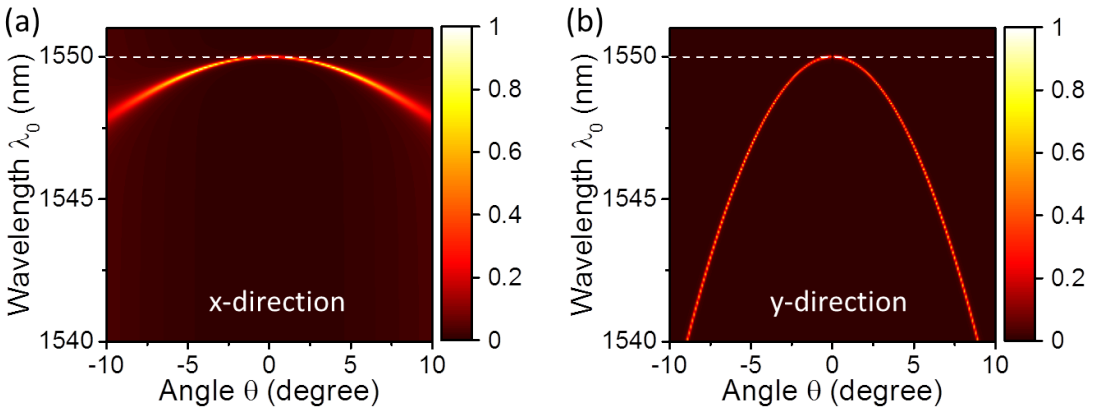

Figure 4.3: Contour maps of the transmissivity (color scale) versus incident angle θ and wavelength λ_0 for a HCG-based vertical cavity to a TM-polarized plane-wave. The incident angle is defined with respect to the normal direction to the grating surface in the (a) x-direction, or (b) y-direction. The cavity is designed to have a resonance at 1550 nm wavelength (shown in white dashed-lines). Structure dimensions and refractive-indices are: HCG Λ_g=640 nm, f_g=0.58, t_g=430 nm, n_h=3.48, n_l=1; DBR t_h=111.4 nm, t_l=261.8 nm, n_h=3.48, n_l=1.48, N_{dbr}=4.5 pairs; nominal cavity t_c=725.1 nm, n_c=1.0; superstrate n_{sup}=1; substrate n_{sub}=1.48.

was explained in chapter 2, the resonance frequency ω corresponds to the peak in the transmissivity spectrum, and a dispersion curve is obtained by plotting ω as a function of in-plane wavevector components k_x or k_y as shown in Fig. 4.4(a). The curvature of the dispersion curve, which is the second derivative of frequency with respect to the in-plane wavevector $\partial^2\omega/\partial k_{x,y}^2$, is an important characteristic of the cavity and referred to as cavity dispersion curvature. It can be in general positive, negative or even zero, as discussed in the following sections.

Method II

Similar to the discussion in section 2.2.6, the resonance wavelength of a cavity mode can be found in quasi-normal mode (QNM) picture. In the FMM formalism without any PML implementation, it is possible to introduce an in-plane incident wavevector in the equations as it was explained in chapter 2. The dispersion curves obtained from this method are in a very good quantitative agreement with 'Method I'. In the FMM, this method is the more efficient compared to the other two approaches, since it requires only several iterations for determining the resonance compared to the 'Method I' [c.f. section 2.2.6], and the computation domain size in the transverse direction is much smaller compared to the 'Method III'.

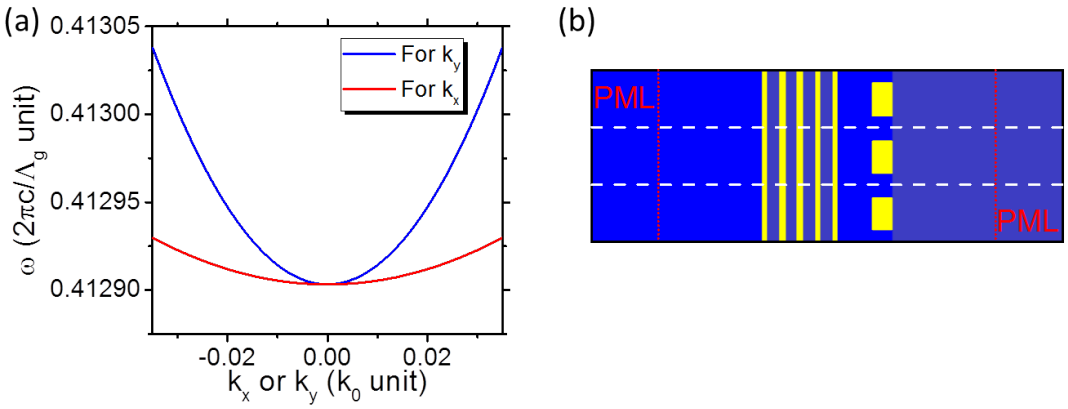

Figure 4.4: (a) Cavity dispersion in the x-direction (red) or y-direction (blue), for the HCG-based cavity in Fig. 4.3. The calculated dispersion curvatures, $\partial^2\omega/\partial k_{x,y}^2$ are 7.82 and 39.53 m^2/s for the x- and y-directions, respectively. (b) Schematic of the structure used for calculating cavity dispersion in 'Method III'. A unit cell in the propagation direction, which is used for calculating the Bloch modes, is shown by white dashed-lines. The PMLs are implemented and their boundaries are shown in red dotted-lines.

Method III

'Method III' can be used only for evaluating the cavity dispersion along the x-direction. For implementing this method, the structure should be rotated 90 degrees [22], i.e. the x-direction and z-direction in the Fig. 4.2 will switch their roles as it is illustrated in Fig. 4.4(b). The PMLs are implemented at the boundaries of computation domain in the x-direction. Using the scattering matrices, the Bloch modes can be calculated as it is already explained in section 2.2.4. The cavity mode is a Bloch mode with low loss, since it is confined by two highly-reflective mirrors. This method also produces the same value for cavity dispersion curvature along the x-direction, as the two previous approaches do. 'Method III' is the most time-consuming method among the three approaches, since it requires a large number of Fourier terms for expanding the Bloch mode accurately due to the larger computation domain in the x-direction compared to the others.

4.1.2 Physical Interpretation

All possible cavity dispersion curves for a vertical cavity are shown schematically in Fig. 4.5(a). By analogy with electron bandstructure, the positively and negatively curved dispersion curvatures are referred to as electron-like and hole-like, respectively. The dispersion curvature can be interpreted simply by a geometrical optic picture, assuming an oblique ray with an in-plane wavevector inside the cavity as illustrated in Fig. 4.5(b). In this picture, positive dispersion curvature corresponds to a

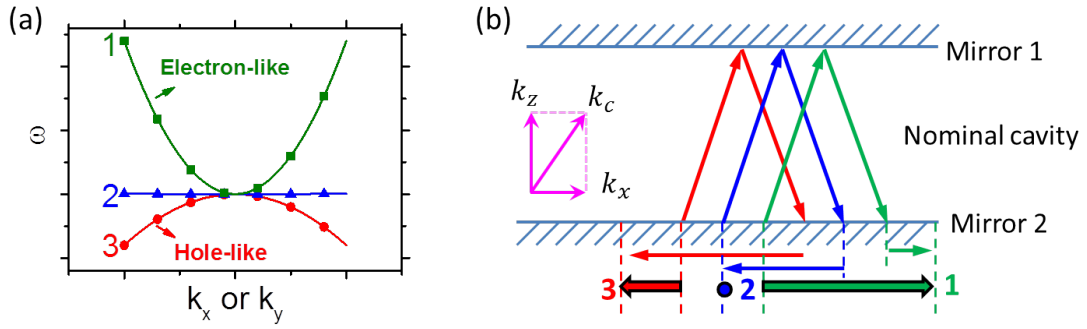

Figure 4.5: (a) All possible cavity dispersion for a vertical cavity structure. They are denoted by analogy to electron bandstructure in the conduction and valance bands, as electron-like (green) or hole-like (red). (b) The geometrical optic interpretations correspond to three cases in (a). Top mirror is assumed to have no dispersion and depending on the dispersion properties of the bottom mirror, three cases are plotted schematically.

forward beam propagation after a round-trip, while negative dispersion curvature corresponds to backward propagation [14]. As it will be shown in the next section, always the nominal cavity has positive dispersion contribution and for simplification, here the top mirror is assumed to be a mirror with negligible dispersion (such as a DBR). Depending on bottom mirror dispersion properties, the corresponding ray pictures for the three cases are possible and shown in Fig. 4.5(b). This phenomena can also viewed as slowing down or speeding up the light in the in-plane direction, for an electron-like or hole-like case, respectively, which is similar to the slow or fast light effect in the PhC waveguide structures [23]–[25]. However, in the vertical cavities the light propagation speed is controlled in the transverse directions compared to the PhC waveguides, in which the light speed is varied in the longitudinal direction [24].

4.1.3 Analytic Expression

In this section, a general expression for the dispersion of a vertical cavity structure is derived [18]. In a vertical cavity, the mode frequency ω is found by solving the oscillation condition, which is the constructive interference condition after a round-trip for a propagating mode:

$$\begin{aligned} &\phi_1(\omega, k_x, k_y) + \phi_2(\omega, k_x, k_y) - 2k_z t_c = 2m\pi, \\ &k_z = \sqrt{\left(\frac{n_c\omega}{c}\right)^2 - k_x^2 - k_y^2}. \end{aligned} \tag{4.1}$$

Here, k_x, k_y, and k_z are wavevector components of a mode in the nominal cavity layer with a refractive index of n_c, and a thickness of t_c, and c is the speed of light in vacuum. Note that the reflectivity phases from the two mirrors, ϕ_1 and

ϕ_2, depend on the in-plane wavevectors, k_x and k_y. The resonance frequency at normal incidence, ω_0 is determined by setting the in-plane wavevectors zero: $2k_{z,0}t_c = -2m\pi + \phi_{1,0} + \phi_{2,0}$, where $k_{z,0} = \omega_0 n_c/c$ and $\phi_{i,0} = \phi_i(\omega_0, 0, 0)$ for i=1,2.

In a vertical cavity, the modes of our interest have a lateral extension of several times of wavelength [18]. Thus, k_x and k_y distributions are close to the Γ-point where $(k_x, k_y) = (0, 0)$ [26]. This validates the following Taylor expansion, keeping the first non-zero derivatives with respect to k_j and ω:

$$\phi_i(\omega, k_x, k_y) \simeq \phi_{i,0} + \frac{1}{2}\sum_{j=x,y} \left.\frac{\partial^2\phi_i}{\partial k_j^2}\right|_0 k_j^2 + \left.\frac{\partial\phi_i}{\partial\omega}\right|_0 \Delta\omega, \tag{4.2}$$

where $\Delta\omega = \omega - \omega_0$ and the derivatives are evaluated at $(\omega, k_x, k_y) = (\omega_0, 0, 0)$. Inserting Eq. (4.2) into Eq. (4.1) leads to:

$$\begin{aligned} \omega &= \omega_0 + \sum_{j=x,y} \beta_j k_j^2, \\ \beta_j &= \frac{c^2}{2n_c^2\omega_0}\frac{t_c}{t_{\text{eff}}} + \frac{c}{4n_c}\frac{1}{t_{\text{eff}}}\left(a_{1,j} + a_{2,j}\right), \end{aligned} \tag{4.3}$$

where t_{eff} $(= t_c + t_1 + t_c)$ is the effective cavity thickness, t_i $(= -\frac{c}{2n_c}\partial\phi_i/\partial\omega)$ is the phase penetration into the i-th mirror, and $a_{i,j} = \partial^2\phi_i/\partial k_j^2$ is the phase curvature of the mirror. The parameter β_j represents the cavity dispersion curvature along the j-direction. The first term of β_j results from the round-trip propagation in the nominal cavity, and is always positive. The second term of β_j accounts for the dispersion curvature from the mirrors. This mirror contribution can be either positive, negative, or even zero for novel mirror structures such as HCG or HG as shown below. Furthermore, it is polarization sensitive and anisotropic.

4.1.4 Discussion

Firstly, to validate Eq. (4.3), the dispersion curvature obtained from this expression is compared with the rigorous calculations. For the exemplary HCG-based cavity of Figs. 4.3 and 4.4, the value of the parameters used in the Eq. (4.3) are obtained as: t_1=193.6 nm, t_2=1014.4 nm, $a_{1,x}$=-0.2754, $a_{2,x}$=0.0185, $a_{1,y}$=0.1331, $a_{2,y}$=0.0185 all in rad/μm^{-2}. These parameters result in a cavity dispersion curvatures of 7.82 m^2/s and 39.53 m^2/s for the x- and y-directions, respectively, which are exactly equal to the values found from the rigorous calculations. Therefore, there is a very good quantitative agreement between the rigorous computations and derived analytic expression. The derived expression provides valuable insight about the important factors in cavity dispersion.

Using the derived expression Eq. (4.3), we can explain the quantitative differences between different types of cavities. For instance, at a wavelength of 1550 nm, the contributions of a 0.5λ-long nominal air cavity to the cavity dispersion curvature is approximately 30 m^2/s. As seen in Eq. (4.3), this nominal cavity contribution increases linearly with the cavity thickness, t_c. The mirror contribution of a typical DBR is on the order of 1 m^2/s and gets smaller for larger refractive index contrast of the DBR layers. This mirror contribution is isotropic due to the rotational symmetry of DBR structures (i.e $a_{i,x} = a_{i,y}$). Therefore, in DBR-based cavities, the cavity dispersion curvature is dominated by the nominal cavity contribution and is always positive and isotropic. Its shape resembles the conduction band of semiconductors. However, in the case of HCGs/HGs, the mirror contribution can be on the order of ± 100 m^2/s or even larger. If the cavity thickness t_c is small, e.g., less than 2λ, the cavity dispersion curvature of HCG/HG-based cavities can be positive, zero or negative, being dominated by the HCG/HG dispersion curvature. Also, the cavity dispersion is anisotropic along the x- and y-directions, and depends on the incident light polarization, as does the HCG/HG mirror dispersion. In HCG/HG-based vertical cavities, it is possible to engineer the cavity dispersion by designing the phase response of the HCG/HG while keeping its reflectivity high as discussed below.

Here, the possibility of varying mirror dispersion of a HCG reflector (i.e. the value of $a_{i,x}$ and $a_{i,y}$), while keeping its reflectivity high, is illustrated with an example. Figure 4.6(a) shows the reflectivity phase contour map as a function of grating bar width W_g and gating period Λ_g for a constant grating thicknesses of t_g=450 nm. This contour demonstrates how the reflectivity phase can be changed, while reflectivity amplitude is kept high, by changing the grating period and bar width [27], [28]. By changing the reflectivity phase of the reflector, we can engineer the resonance frequency of the cavity mode. Thus, as it will be explained in section 4.2, an in-plane heterostructure in the HCG-based cavities can be designed simply by varying the grating parameters.

Figures 4.6(c) and 4.6(d) illustrate the transverse phase curvature contour maps, which are defined as $\partial^2\phi/\partial k_x^2$ and $\partial^2\phi/\partial k_y^2$ in the x- and y-directions, respectively, The value of the phase curvature is controlled in the both transverse directions just by varying the grating parameters, and its value can be positive, negative or zero. In comparison, for a DBR structure made of Si/SiO_2, the phase curvature value is always positive and relatively small, e.g. on the order of 0.01 $rad/\mu m^{-2}$. The phase curvature can be large for the HCG or HG reflectors, since in oblique incident angle odd waveguide modes contribute to the reflection process considerably [17]. In Fig. 4.6(b), the reflectivity phase contour map is plotted for a small incident

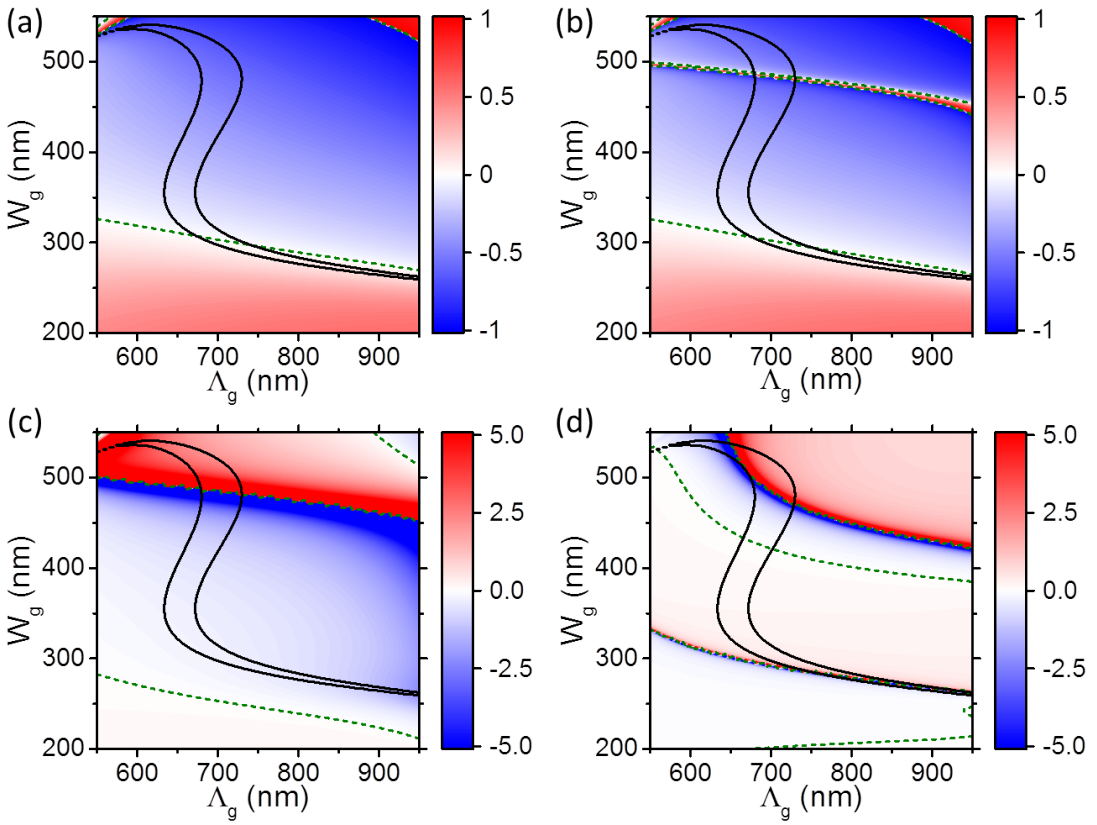

Figure 4.6: HCG contour maps (color scale) of (a) reflectivity phase at normal incident (π unit), (b) reflectivity phase at 5 degree incident angle (π unit), (c) phase curvature in the x-direction $\partial^2\phi/\partial k_x^2$ (μm^{-2} unit), (d) phase curvature in the y-direction $\partial^2\phi/\partial k_y^2$ (μm^{-2} unit), versus grating period Λ_g and grating bar width $W_g = f_g\Lambda_g$ for a TM-polarized plane-wave at 1550 nm wavelength with grating thickness of t_g=450 nm. Black solid-lines correspond to reflectivity amplitude of 99.5 % at normal incident angle, and in the region between them, the reflectivity amplitude is above 99.5. Green dashed-lines correspond to th zero values in the contours. These contours illustrate the flexibility of designing a HCG with very high reflectivity amplitude and at the same time various dispersion curvatures, for both in-plane directions. In Figs. (c) and (d) the color bars are only limited to ±5 range which is usually interesting from laser application point of view.

angle in the x-direction, i.e. small k_x value. Compared to the normal incident angle case [Fig. 4.6(a)], a region of rapidly-changed phase appears in the contour, which is due to the resonance excitation of an odd waveguide mode in grating layer. Therefore, in the vicinity of this region, a large phase curvature $a_{i,j}$ is possible for the reflector [17]. Similar results can be obtained for a HG reflector. It should be mentioned that if the phase curvature becomes very large, i.e. the reflectivity phase vary rapidly with incident angle, usually the reflectivity amplitude will also drop considerably, which results in an increase for the threshold gain in laser applications [29]. Thus, for the HCG/HG-based laser applications, usually the phase curvature value in the range of ±5 seems useful from our experience.

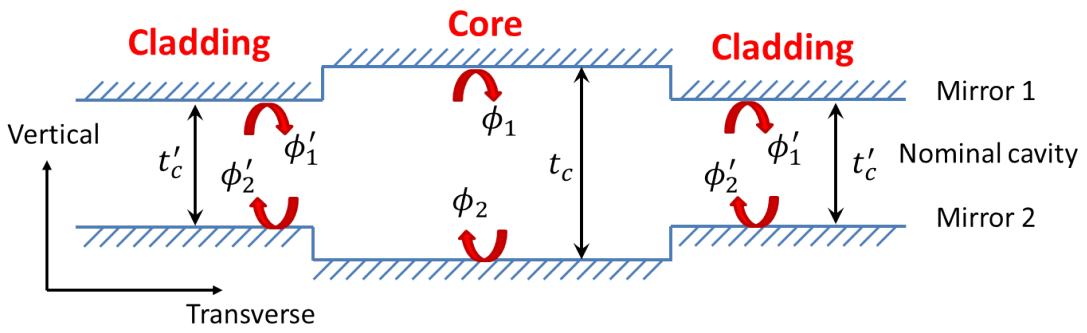

Figure 4.7: Schematic of a vertical cavity structure with transverse variation of the cavity parameters (t_c, ϕ_1 and ϕ_2) in the core and cladding sections to form transverse confinement.

4.2 Vertical Cavity In-Plane Heterostructure

In designing a VCSEL, arranging vertical cavity sections as shown in Fig. 4.7 to obtain an ideal transverse confinement profile is a key step, since the transverse confinement profile significantly influences important properties, such as threshold current, modulation speed, single-mode property, and output beam profile. Various VCSEL structures have been reported for controlling the transverse confinement, including ones with an oxide aperture [30], a tunnel junction [31], an anti-guiding geometry [32], a shallow surface relief [33], inverted-surface relief [34], photonic crystals [35], or a HCG heterostructure [36]. The transverse confinement mechanisms in many of these different VCSEL structures can be understood by the concept of in-plane heterostructure, as discussed in this section.

In vertical cavities, an in-plane heterostructure is formed by changing the cavity parameters in different sections of the cavity as shown in Fig. 4.7, which results in transverse mode confinement. In early studies on VCSELs employing DBRs as mirrors, the transverse confinement was explained as resulting from a lower resonance frequency of the core section compared to that of the cladding section [37]. However, with new types of reflectors such as the HCG or HG, cavity dispersion curvature can determine the transverse confinement properties [18]. When the curvature is positive, i.e., electron-like, the frequency of the core section needs to be lower than that of the cladding to achieve field confinement in the core section. This is analogous to a quantum well (QW) in the conduction-band of semiconductors, with the frequencies of the confined mode being allowed in the well (core) section and forbidden in the barrier (cladding). On the contrary, when the curvature is negative, the frequency of the core section needs to be higher than

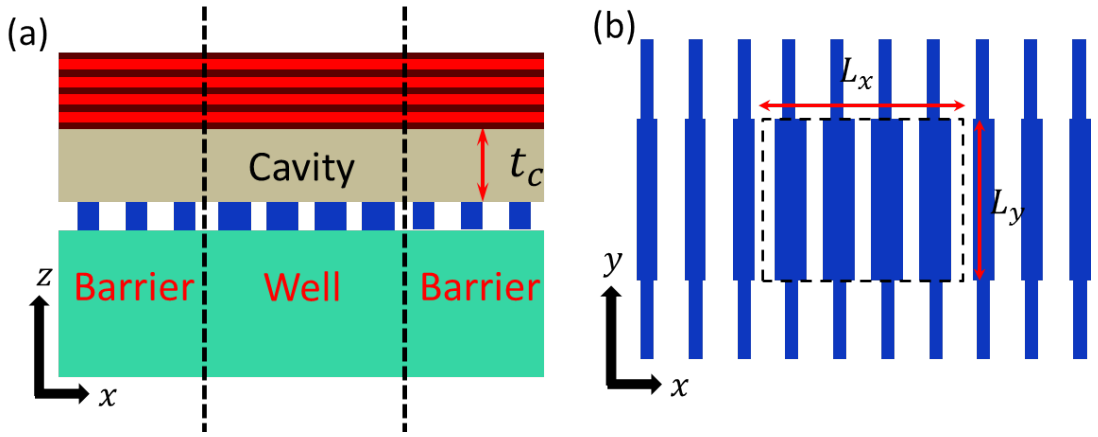

Figure 4.8: (a) Cross-sectional schematic of a HCG-based vertical cavity structure consisting of a DBR and a HCG mirror and a low-refractive-index cavity layer. (b) Top view of the HCG layer. The grating bar width W_g is varied along the x- and y-directions to make a heterostructure with the well sizes of L_x and L_y.

the cladding, which is analogous to a valence-band QW. For quantitative analysis of heterostructure, the envelope approximation can be used.

The envelope approximation derived for photonic crystal heterostructures [38], [39], can be applied to analyze VCI heterostructures [18], [40]. In this section, HCG-based cavities with in-plane heterostructure such as those shown in Fig. 4.8 are investigated mainly. The effective mass m_j defined for the envelope approximation, is related to the dispersion curvature, β_j: $1/m_j = \partial^2\omega^2/\partial k_j^2 = 4\omega_0\beta_j$. By changing the vertical cavity parameters in the core and cladding sections, a photonic well can be formed for in-plane directions. This can be obtained by any geometrical change in the device dimensions such as cavity thickness or any carrier-induced change such as carrier-induced refractive-index changes. For instance, in a VCSEL with an oxide aperture, the oxide aperture region works as the photonic well section. Therefore, in the transverse directions, the cavity acts as a two-dimensional (2D) photonic well structure. Using the envelope approximation, the resonance frequency of a rectangular VCI photonic well $\omega_{p,q}$ is found as [18], [40]:

$$\omega_{p,q}^2 \simeq \omega_0^2 + \frac{\alpha_x(p\pi)^2}{2m_xL_x^2} + \frac{\alpha_y(q\pi)^2}{2m_yL_y^2}, \tag{4.4}$$

where p and q are mode numbers in the x and y directions, respectively, L_x and L_y are the lengths of the heterostructure as defined in Fig. 4.8(b), and the rational factors α_x and α_x account for the effect of finite barrier heights. This expression can be used to interpret the simulation results for HCG/HG-based vertical cavities.

4.2.1 Dispersion Curvature Effects

In this section, the influences of dispersion curvature on VCI heterostructures are investigated with numerical simulations of several characteristic photonic well structures. All structures have a 0.5λ-long air cavity, which can be formed by sacrificial etching in a similar way as in Ref. [40], and a HCG that is designed to be highly reflective for a TM-polarized light. Although, most of the simulations are performed for a 2D cross-section of the structure, similar results will be obtained for three-dimensional (3D) simulations of the structure.

Transverse Mode Order

It is well known in the VCSEL literature that higher order transverse modes have higher frequencies, i.e., shorter wavelengths, due to their higher in-plane wavevectors. However, the dispersion of HCG or HG reflectors in HCG/HG-based cavities can significantly modify this characteristics [18], [19]. For the photonic wells with positive dispersion curvatures, we have the usual situation of VCSELs, as shown in Fig. 4.9(a): the fundamental mode has the longest wavelength. However, for the negative dispersion curvature case, the fundamental mode has a shorter wavelength than the higher order mode, as shown in Fig. 4.9(b). Referring to Eq. (4.4), this observation can be interpreted like this: the higher order mode with more spatial modulation adds a larger negative kinetic energy due to a negative mass, lowering the total energy. The positive dispersion curvature (electron-like) and negative dispersion curvature (hole-like) cases are analogous to the electronic QWs in the conduction band and valence band, respectively.

Transverse Mode Wavelength Spacing

Figure 4.10(a) plots the wavelength spacing of the two lowest transverse modes as a function of the x-direction dispersion curvature β_x, in the well region. It shows that the wavelength spacing increases with the dispersion curvature. This observation can be understood also by referring to Eq. (4.4): with a smaller dispersion curvature, corresponding to a larger effective mass, the kinetic energy contribution to the total energy becomes smaller, leading to a smaller energy difference between two transverse modes. Therefore, the transverse mode spacing can be controlled by engineering the dispersion of the HCG or HG, without changing the transverse mode size. This results in interesting phenomena such as mode grouping and mode degeneracy, with several possible applications, as discussed below.

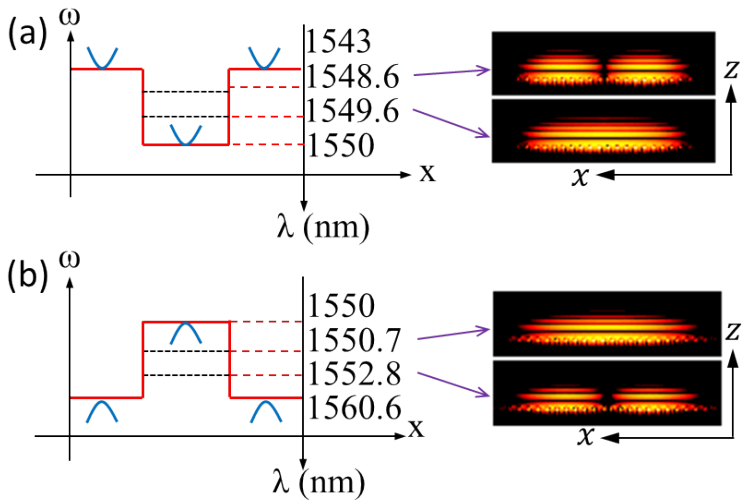

Figure 4.9: Band edge profiles in red color for (a) positive and (b) negative dispersion curvatures, respectively. The first two transverse mode profiles are shown with their resonance wavelengths. Blue curves in (a) and (b) represent dispersion curves. Structure dimensions and refractive-indices are provided in Appendix C, section C.2.1.

Transverse Mode Grouping and Degeneracy

For a VCI heterostructure, if m_x and m_y largely differ, the transverse modes are grouped as shown schematically in Fig. 4.10(b). In Fig. 4.10(b), the effective mass along the y-direction is ∼10 times smaller than that along the x-direction. As a result, the second mode number for the y-direction determines the larger wavelength spacing between groups, while the first one for the x-direction determines the smaller wavelength spacing within a group. This mode grouping is experimentally observed in a HCG-based cavity laser [40]. The wavelengths and mode profiles in Figs. 4.10(b) and 4.10(c) are obtained by 3D simulations. Furthermore, the fundamental mode frequency $\omega_{0,0}$ and higher order mode frequencies, $\omega_{p,p}$ can be made degenerate, by designing the effective mass so that $m_x = -m_y$ and $\alpha_x/L_x^2 = \alpha_y/L_y^2$ [c.f., Eq. (4.4)]. This transverse mode-degeneracy is also confirmed by 3D simulations.

This control over transverse mode spacings can be used to boost the speed of a laser diode. Recently, the bandwidth boost of laser diodes has attracted a lot of attention [41], [42]. The boost mechanism is based on the introduction of a photon-photon resonance at a frequency higher than the relaxation oscillation frequency by exploiting external optical feedback or cross-gain modulation. In HCG/HG-based vertical cavities, multiple transverse modes can be designed to have specific wavelength spacings, e.g., 0.15 nm, which determines the photon-photon resonance frequency. In this way, multiple photon-photon resonances can be introduced at designed frequencies through cross-gain modulation. For this, all the

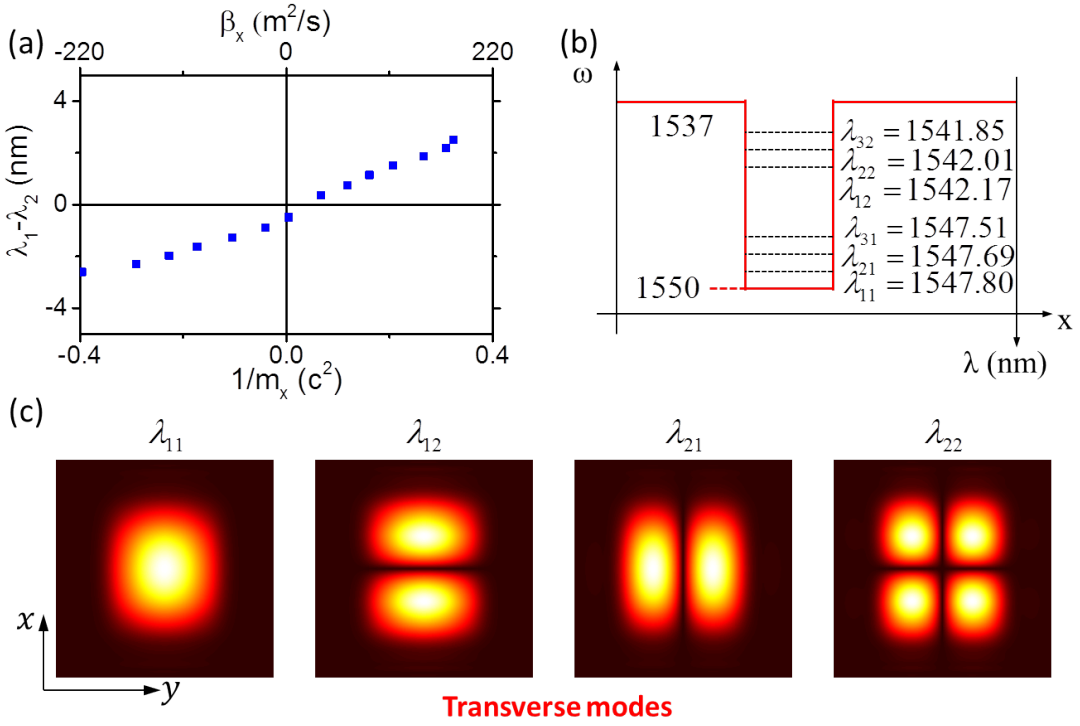

Figure 4.10: (a) Transverse-mode wavelength spacing between the two lowest modes as a function of dispersion curvature for a HCG-based cavity. (b) Band edge profile of a 2D photonic well, and (c) mode profiles therein, obtained by 3D simulations. This explains the mode grouping effect in a 2D photonic well due to different effective mass in x- and y-directions. Structure dimensions and refractive-indices are provided in Appendix C, section C.2.2.

involved transverse modes need to be lasing, which is feasible in the HCG/HG-based cavities, since we can separately control the mode profile and the gain profile.

Heterostructure with Mixed Effective Masses

The unique possibility to design various effective masses in well and barrier regions enables exotic photonic well configurations. An interesting example is a photonic well where the sign of effective mass in the barrier region is opposite to that of the well region, e.g. hole-like barrier with electron-like well. In order to obtain transverse mode confinement, the band edge of the barrier should be lower than that of the well. This band edge alignment is opposite to the case of the Fig. 4.10(a), where both barrier and well are electron-like cavities. To compare these two cases, a VCI heterostructure with positive effective masses in the well and right barrier and a negative effective mass for the left barrier is investigated, as illustrated in Fig. 4.11(a). The mode is well confined within the well section, as shown in Fig. 4.11(b). If the band edge of the left barrier is moved above the band edge

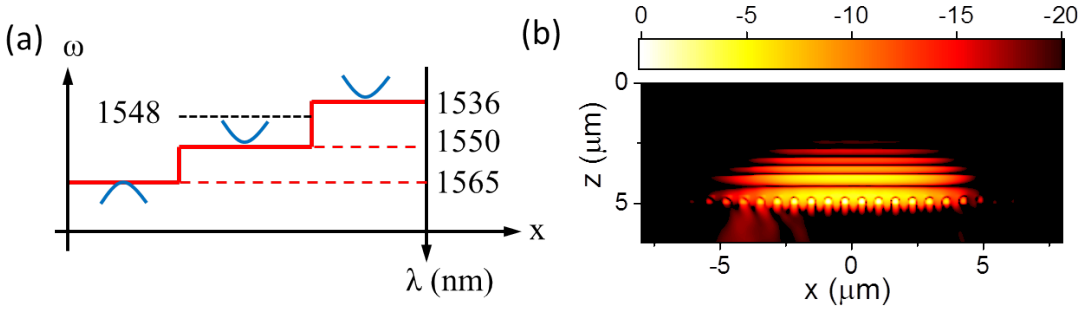

Figure 4.11: (a) Band edge profile of a photonic well structure with opposite effective masses in left and right barriers. (b) Normalized field profile ($|H_y|$) of the structure in (a) (dB scale). Structure dimensions and refractive-indices are provided in Appendix C, section C.2.3.

of the well, the field is no longer confined in the well. This example shows that HCG/HG-based VCI heterostructures allow more freedom for designing photonic wells by controlling the effective mass as well as the band edge.

Penetration Depth into the Barrier

It is well-known from the quantum mechanics that a confined mode in the well has a finite penetration into the barrier. Similarly, in a photonic well structure, the optical mode penetrates spatially into the barrier section. The penetration is quantified by penetration depth or equivalently its inverse, decay rate into the barrier. By using a simple 1D photonic well model, it can be easily shown that the decay rate into the barrier γ_x is obtained as [38]:

$$\gamma_x = \sqrt{2m_x(\omega_b^2 - \omega_w^2)} \approx \sqrt{4m_x\omega_w\Delta\omega} \tag{4.5}$$

where m_x is the effective mass in the barrier section and ω_w and ω_b are the frequency of band edge in the well and barrier sections, respectively, and $\Delta\omega = \omega_b - \omega_w$ is the barrier height. Figure 4.12 compares the envelope approximation results using Eq. (4.5) with the rigorous calculations found by curve fitting of field in numerical simulation for electron-like or hole-like cavities. There is good quantitative agreement between the two, particularly for small barrier heights. By increasing the barrier height, the penetration depth into the barrier decreases, since it is more difficult for the photons to penetrate into a larger barrier. In a HCG/HG-based VCI heterostructure, the barrier decay rate is an important characteristic, which affects the design of heterostructure as discussed in the section 4.2.3.

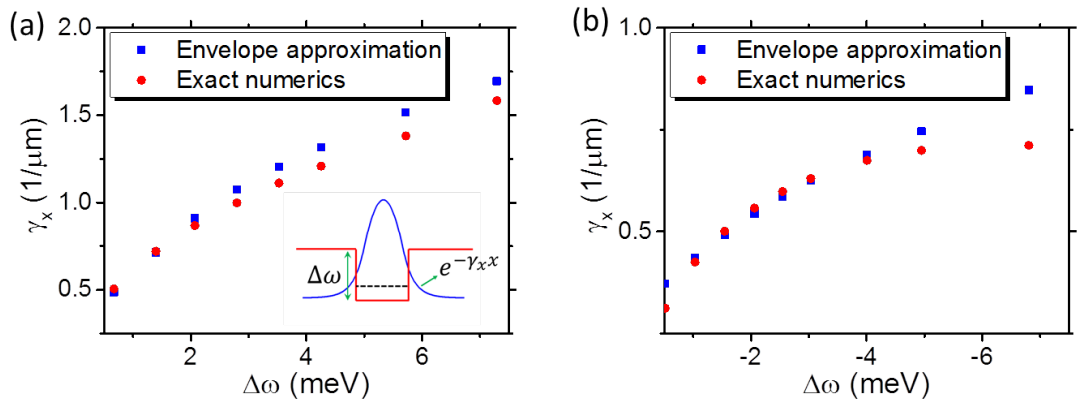

Figure 4.12: Spatial decay rate into the barrier for the fundamental mode in a VCI heterostructure with (a) positive dispersion curvature (b) negative dispersion curvature, versus the barrier height $\Delta\omega = \omega_b - \omega_w$. The results from rigorous numerical simulations (red) are compared with envelope approximation using Eq. (4.5) (blue), which show relatively good agreement. Structure dimensions and refractive-indices can be found in Appendix C, section C.2.4.

4.2.2 Simulation

For a HCG/HG-based VCI heterostructure, it is possible to simplify the simulation of in-plane heterostructure by using low-dimensional simulations of structure, as shown schematically in Fig. 4.13 for the HCG case. Furthermore, by performing low-dimensional simulations, one can estimate the cavity loss in the transverse directions separately. This approach is particularly useful for optimizing the in-plane heterostructures design in a enormously faster way, compared to cumbersome 3D simulations. In the lowest dimensional simulation, referred to as one-half-dimensional (1.5D) simulation, a structure with one period of the HCG or HG is used, and it is assumed that the structure is uniform in the y-direction. Actually, it is a 2D simulation for a structure with infinite number of grating periods due to periodic boundary conditions in the x-direction. This kind of simulation has been already employed for computing the cavity dispersion. For a 2D simulation, a finite number of grating periods is considered as illustrated in Fig. 4.13(b), and the structure is assumed to be uniform in the y-direction, similar to the 1.5D case. Absorbing boundary conditions should be implemented in the x-direction (red dot line in the figure). A 2D simulation can be employed to estimate the loss in x-direction, and also to design an optimized VCI heterostructure in this direction. Many simulations in this dissertation are performed on these type structures. Figure 4.13(c), shows a 2.5D structure used for 2.5D simulations, in which only a single grating period is used, similar to the 1.5D structure. However, the structure is not uniform in the y-direction any more, and absorbing boundary conditions are

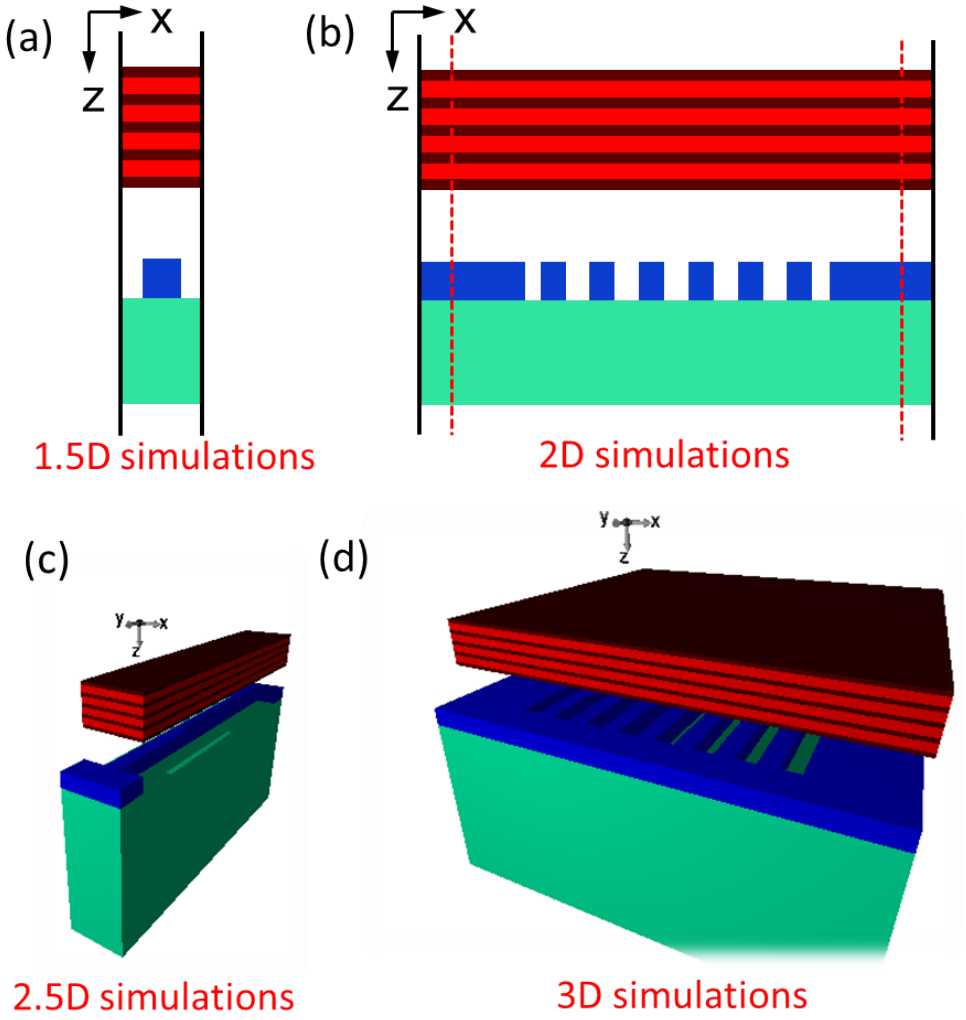

Figure 4.13: Schematic view of a HCG-based vertical cavity structure used for (a) 1.5D simulations, (b) 2D simulations, (c) 2.5D simulations, and (d) 3D simulations.

employed in the y-direction. A two-half-dimensional (2.5D) simulation is used to design an appropriate in-plane heterostructure in the y-direction. Finally, the complete structure consists of finite number of grating periods with variation in the y-direction is shown in Fig. 4.13(d). This is the most numerically cumbersome simulation in which absorbing boundary conditions are required in both x- and y-directions. This technique can be used for designing and optimizing the in-plane heterostructure, and for final validation a rigorous 3D simulation is performed.

4.2.3 Design

VCI heterostructure can easily be formed in the HCG/HG-based cavities as it is already discussed in the previous section and shown also in Fig. 4.8. These

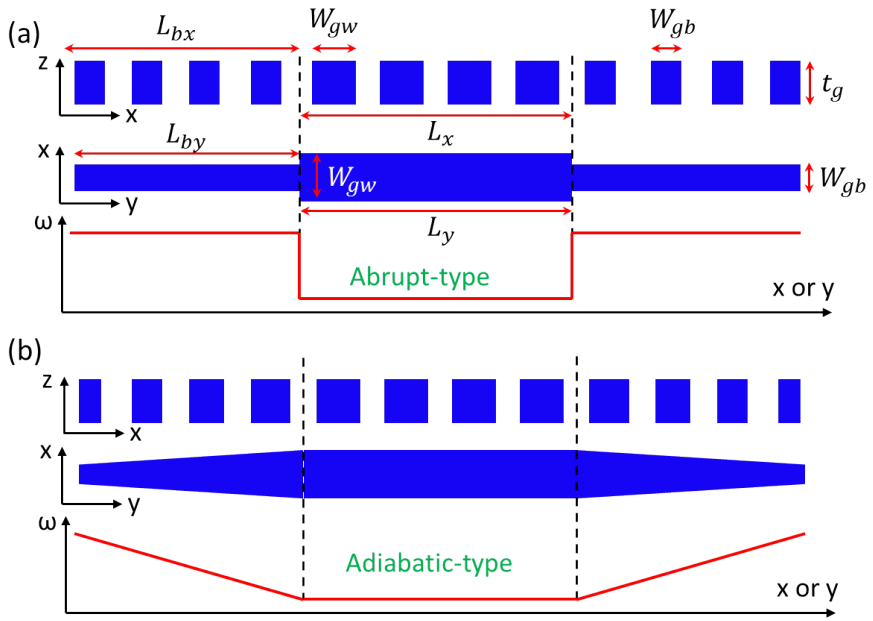

Figure 4.14: (a) Cross-sectional schematic of a grating bar in the x-z plane (top), and x-y plane (middle) for HCG-based VCI heterostructure with (a) Abrupt-type barrier, and (b) Adiabatic-type barrier. The grating bar width W_g is varied along the x- and y-directions to make a heterostructure with the well sizes of L_x and L_y as shown schematically (bottom).

heterostructures are easy to be fabricated, since they are defined simply by changing the grating bar width in the e-beam lithography process. We are particularly interested in the photonic well structures to make an efficient transverse mode confinement for VCSEL applications. In this section, important considerations for designing an effective barrier are reviewed, and numerical examples for the barrier in the x-direction are provided. Similar conclusions are valid for the y-direction. The barriers can be formed adiabatically or abruptly as it is shown in Figs. 4.14(a) and 4.14(b), respectively.

In the VCI heterostructure, three different loss mechanisms can be defined; vertical out-coupling loss through the both mirrors, lateral out-coupling loss through the in-plane barriers, and scattering loss due to the refractive-index perturbation of the cavity by heterostructure [36]. In this section, both mirrors are designed to be highly-reflective (reflectivity amplitude above 99.99%), which result in a low vertical out-coupling loss. Figure 4.15(a) shows the Q-factor of the two highest-order transverse modes of an exemplary 2D HCG-based VCI heterostructure versus the barrier length for several different barrier heights. The barrier length in the transverse directions should be at least several times of the barrier penetration depth, in order to have an effective barrier. Otherwise, the optical mode tail will not be attenuated enough, when it reaches the boundary of the barrier region, which

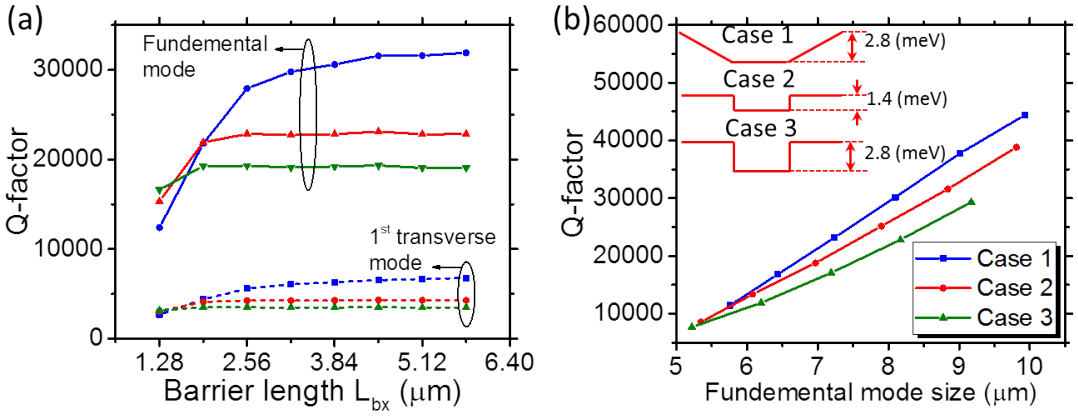

Figure 4.15: (a) Q-factor of the fundamental and 1^{st}-order transverse mode in a 2D HCG-based cavity as a function of barrier length L_{bx}, for a abrupt-barrier with height of 1.37 meV (in blue), 2.77 meV (in red), and 4.22 meV (in green). As long as the barrier length is large enough the Q-factor saturates. Shorter barrier requires longer barrier length, and result in higher Q-factor, since the scattering loss becomes smaller. (b) Q-factor of the fundamental transverse mode of structure in (a) versus its mode size for several different barrier cases. The mode size is defined as the width, where the field amplitude drops to 1/e of its maximum value. Adiabatic-barrier results in higher Q-factor compared to abrupt-barrier cases. Structure dimensions and refractive-indices can be found in Appendix C, section C.2.5.

results in additional lateral loss. For a large-enough barrier length, shorter barrier height is advantageous, since it results in smaller perturbation and consequently less scattering loss. However, it should be noted that the optical mode will also be larger for shorter barrier, since it will penetrate longer into the barrier region. Therefore, to compare different types of barrier, the comparison should be made for a constant mode size including the penetration depth into barrier. Here, the fundamental mode size is defined as the width, where the field amplitude drops to 1/e of its maximum value.

We may improve the performance of the barrier by using an adiabatic-type heterostructure. The adiabatic-type barrier reduces the scattering loss considerably, since the perturbation in the cavity is less in the region where the field amplitude is large, and it increases for the region with smaller field amplitude. Figure 4.15(b) compares the Q-factor of the fundamental transverse mode versus its size for three different barriers for the same barrier length. 'Case 1', in which the barrier is adiabatic-type shows higher Q-factor and less lateral loss compared to the other cases.

4.3 Vertical Cavity Examples

In this section, several HCG/HG-based vertical cavity structures are designed and simulated to show the capability of this platform. Firstly, a HG-based vertical cavity structure is designed and simulated for using as an electrically-pumped laser, which possesses a more feasible fabrication process and superior thermal characteristics compared to its HCG-based laser counterpart. Secondly, a HCG-based vertical cavity with very efficient power emission into an in-plane waveguide is designed and investigated numerically, which shows promising results for being used as a Si-integrated light source. Finally, a system of two laterally-coupled vertical cavities is introduced and the parity-time breaking phenomena is illustrated in this structure, which can be interesting for the fundamental physics study in this platform.

4.3.1 Electrically-Pumped HG-Based Vertical Cavity

As it is already mentioned, an interesting possibility with HG is that the cap layer may include an active material such as QWs or quantum dots (QDs). Using this active HG, one may implement a HG-based vertical cavity laser, where light is generated inside the mirror, rather than in the middle of the cavity. Thus, the HG-based vertical cavity laser consists of a passive DBR, a very thin passive cavity made of low refractive-index materials, e.g., air or SiO_2, and an active HG reflector as shown schematically in Fig. 4.2(b). Since we are interested in Si-integrated light source applications, the cap layer is a III-V epitaxial structure contains QWs, which can directly be wafer-bonded to the Si grating layer [43]. The grating is formed by electron-beam lithography and dry etching processes on a silicon-on-insulator (SOI) wafer [40]. The HG-based laser is advantageous compared to the HCG-based one proposed in Ref. [40]. For instance, it possesses a more feasible fabrication process, since the sacrificial layer etching step can be removed. Furthermore, in the HG-based laser the heat generated inside the active region can be dissipated more easily, through the silicon grating layer, since it is in a direct contact with it. Contrastingly, for the HCG-based structure, the active region is above the air cavity [40], [43], which makes the heat dissipation less efficient.

Here, an electrically-pumped laser is designed with a HG-based vertical cavity using a InP cap layer, which includes seven InGaAlAs QWs. A tunnel junction is employed to reduce the series resistance, since both contact regions can be made of n-doped semiconductor materials with lower resistance compared to the p-doped counterparts. Free-carrier absorption is modeled by introducing loss in the doped regions, through an imaginary refractive-index value. The DBR is made

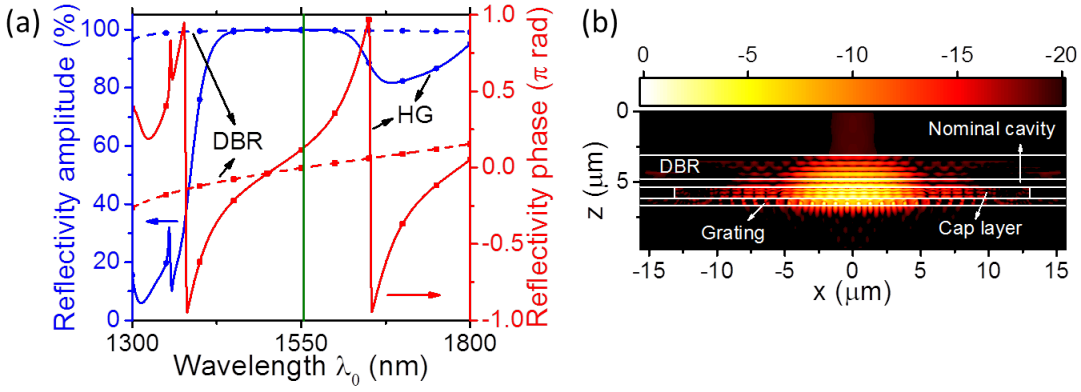

Figure 4.16: (a) Reflectivity amplitude in percentage (blue curves) and reflectivity phase in radians (red curves) for the designed HG reflector (solid-lines) and DBR (dashed-lines). The green line indicates the designed wavelength which is 1554.2 nm. (b) Normalized field profile $|H_y|$ in dB of the fundamental mode in the designed 2D HG-based cavity. The mode resonance wavelength and Q-factor are 1554.3 nm and 4138, respectively. Structure dimensions and refractive-indices can be found in Appendix C, section C.2.6.

of amorphous Si and SiO_2, and due to large refractive-index contrast only a few pairs are required. Figure 4.16(a) shows the reflectivity phase and amplitude for the active HG reflector and passive DBR. It should be noted that the QWs were placed at the electric field maximum to maximize the optical confinement factor and the tunnel junction layers were positioned at the minimum of the field to reduce the free carrier absorption. The normalized field profile of the fundamental mode in 2D simulated structure is also shown in Fig. 4.16(b). The nominal cavity thickness is designed for a resonance at wavelength of 1554.2 nm, since the gain peak is estimated to be at this wavelength for laser working temperature. The Q-factor of the fundamental mode is 4138, considering all the absorption losses in the contact and tunnel junction regions, which is sufficient for laser applications.

4.3.2 HCG-Based Vertical Cavity with In-Plane Emission

An important requirement for a monolithic light source in silicon photonic applications is the possibility to emit light into a silicon waveguide. The HCG-based vertical cavity is a promising candidate for this possibility [9]. So far, the properties of the HCG-based cavities considering vertical emission through the top or bottom mirrors have been investigated. However, for HCG-based vertical cavities, it is also possible to emit the light into an in-plane silicon waveguide, which is placed where the grating modulation is terminated as shown schematically in Fig. 4.17(a). In this case, the light is propagating and amplified in the vertical direction but small portion of it, can be coupled to the in-plane waveguide due to the coupling between

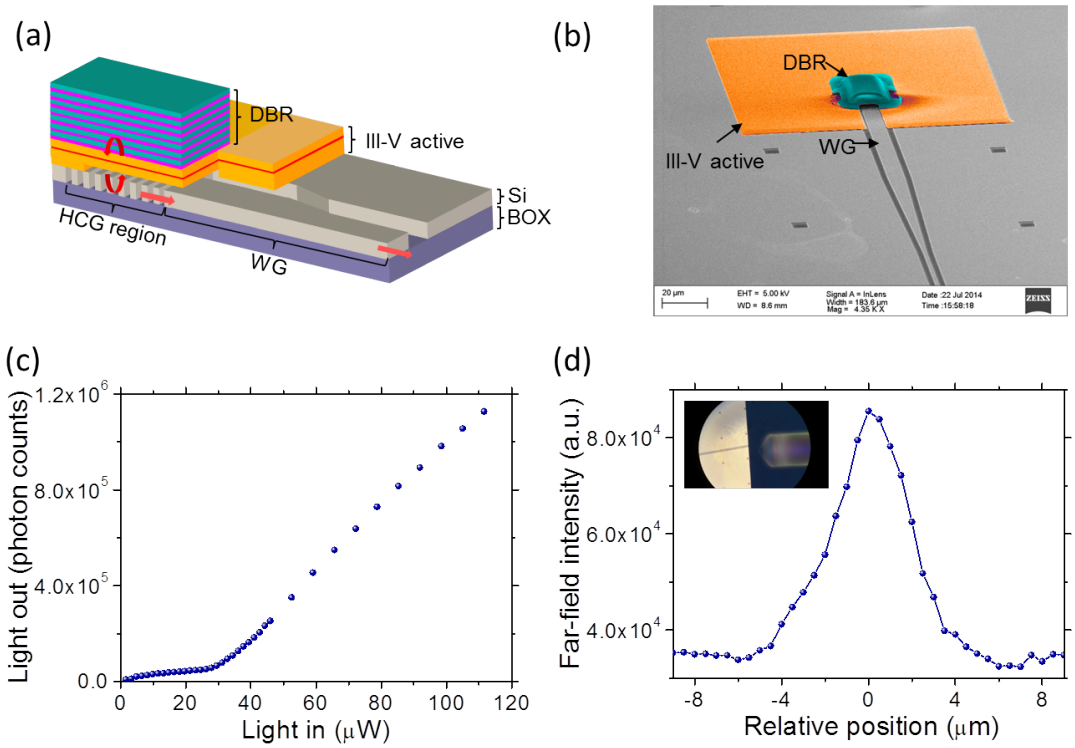

Figure 4.17: (a) Schematic view of a HCG-based hybrid laser with in-plane silicon waveguide. (b) Scanning electron microscope (SEM) image from the top of the fabricated device. (c) In-plane light emission from the silicon waveguide as a function of absorbed input light. (d) Intensity profile of the in-plane emission from the waveguide. The position zero corresponds to the waveguide center position [40].

the tail of optical mode and the waveguide [9], [44]. In our group, based on this structure, a hybrid laser was designed, fabricated and experimentally characterized recently as shown in Fig. 4.17 [40]. Figure 4.17(c) illustrates the laser output from the in-plane silicon waveguide graph versus input light, which clearly shows the laser characteristic. Also, the far-field intensity from the in-plane waveguide is shown in Fig. 4.17(d) [40]. Therefore, these experimental results demonstrate the feasibility of emitting the light into an in-plane waveguide. The design rules for maximizing the out-coupling efficiency $\eta_{in-plane}$, which is defined as the ratio of the power emitted to in-plane waveguide to the total power emitted out of cavity, are reviewed below with a numerical example.

In order to maximized the out-coupling efficiency $\eta_{in-plane}$, all light emission in the vertical directions should be minimized. Thus, the DBR is deigned to be 6.5 pairs of Si/SiO_2 which results in a very high reflectivity amplitude (above 99.997 % at 1550 nm wavelength). Similarly, the HCG should be designed to show high reflectivity amplitude. Beside the HCG reflectivity, several other important characteristics for the bottom HCG reflector should be considered. Firstly, the HCG

reflectivity should not drop dramatically with incident angle, since it can increase the threshold gain. Secondly, the in-plane phase response, which determines the cavity dispersion curvature, should be designed carefully. The cavity dispersion curvature defines the lateral penetration into the barrier, mode size and also the light lateral velocity. Finally, the position of the waveguide with respect to the optical mode position is very important. Figure 4.18 shows the field profile of a HCG reflector illuminated by a TM-polarized Gaussian beam at two different beam position, while keeping all the other parameters unchanged. By moving the center of the beam toward to waveguide starting position, the coupling efficiency to the waveguide is increased dramatically. Therefore, for an efficient in-plane light coupling, the cavity mode tail should have a good overlap with the in-plane waveguide [9]. In the HCG-based cavity, the optical mode waist (size) and its position depend on the transverse mode confinement scheme and cavity dispersion curvature.

When there is no separate transverse mode confinement scheme in the HCG-based vertical cavity, the mode is mainly defined by the grating region area, i.e. the optical mode size is roughly defined where grating is terminated. By introducing in-plane heterostructure as explained before, it is possible to make the appropriate lateral confinement. The penetration depth into the barrier depends on the cavity dispersion curvature in the barrier region. To maximize the emission to the waveguide, no in-plane heterostructure is introduced for the right side. However, an adiabatic in-plane heterostructure is designed for the left side to prevent the light from escaping from that side. Furthermore, a relatively large cavity dispersion curvature is required in order for light to have the enough momentum while escaping from the cavity from right side. Considering all of the above consideration, a HCG-based vertical cavity structure with an InP active region is designed with high in-plane light emission into a silicon waveguide. Figures 4.19(a) and 4.19(b) show the schematic of simulated structure and its field profile, respectively. The large field value in the silicon waveguide is observed, which results in a large out-coupling efficiency of approximately 68%.

4.3.3 Laterally-Coupled HCG-Based Vertical Cavities

Coupled micro-cavity structures have displayed many interesting phenomena, such as miniband formation [45], heavy photons [46], coupled-cavity QED [47], and recently parity-time (PT) symmetry breaking [48], [49]. For the implementation of them, various structures have been suggested, including PhC coupled cavities [45], microring resonators [48], [49], and vertically-coupled VCSELs [50]. Here, a system of two laterally-coupled vertical cavities is proposed, as shown schematically in Fig.

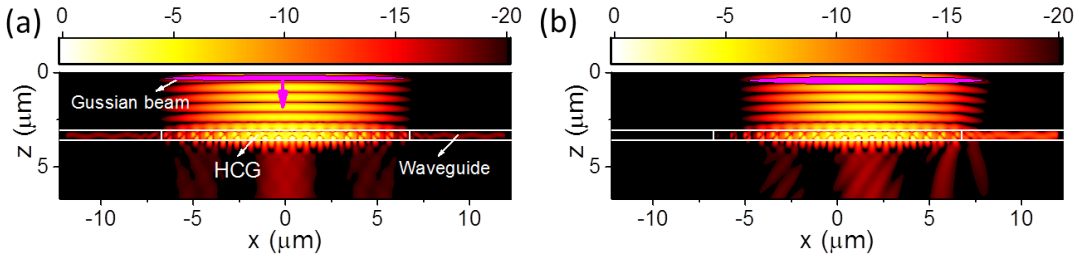

Figure 4.18: Normalized profiles $|H_y|$ in dB of a HCG illuminated by a TM-polarized Gaussian beam with beam waist of 7 μm with beam center at (a) x_0=0 , (b) x_0=1.5 μm. By moving the beam toward right, i.e. making it closer to the waveguide starting position, the lateral emitted power is increased considerably. Structure dimensions and refractive-indices can be found in Appendix C, section C.2.7.

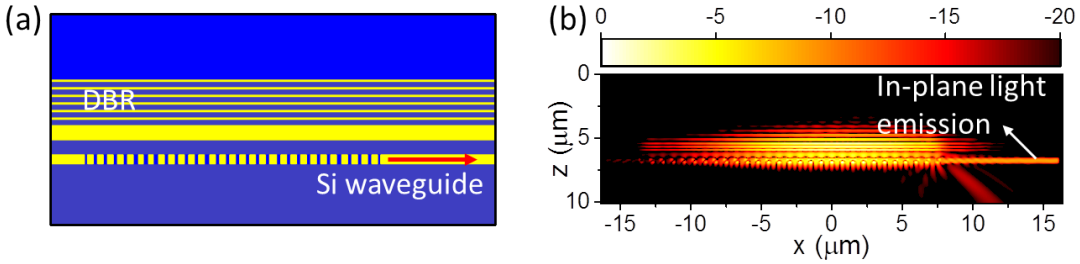

Figure 4.19: A HCG-based vertical cavity with an InP active region designed for large in-plane light emission into a waveguide. (a) Schematic view of the simulated structure. (b) Normalized mode profile $|H_y|$ in dB scale of the fundamental cavity mode. The out-coupling efficiency to the silicon waveguide is more than 68%. The resonance wavelength and Q-factor of the fundamental cavity mode are λ_r=1549.3 and Q=6590, respectively. Structure dimensions and refractive-indices can be found in Appendix C, section C.2.8.

4.20(a). In this structure, the directions of the light propagation (vertical) and coupling (lateral) are separated from each other, while they are in the same directions in other coupled cavities. This makes access to the properties of the individual cavities easier. As shown in Fig. 4.20(b), the coupling of two identical cavities leads to two coupled states with even and odd parities. The coupling strength can be tuned by changing the barrier width, height, or effective mass. Here, the barrier width W_c is chosen. As shown in Fig. 4.20(c), the separation between the wavelengths of the two resulting states becomes larger for a larger coupling, i.e., smaller W_c.

Recently, there is a great interest for understanding and utilizing the unusual properties of PT-symmetric structures, in which there are gain and loss sections in a mirror symmetrical form. Particularly, two coupled cavities in PT-symmetric arrangement exhibit exotic behaviors close to the exceptional point such as enhancement of laser bandwidth [51], pump-induced lasing death [52] and suppressing higher order modes [53]. The exceptional point is a characteristic signature of

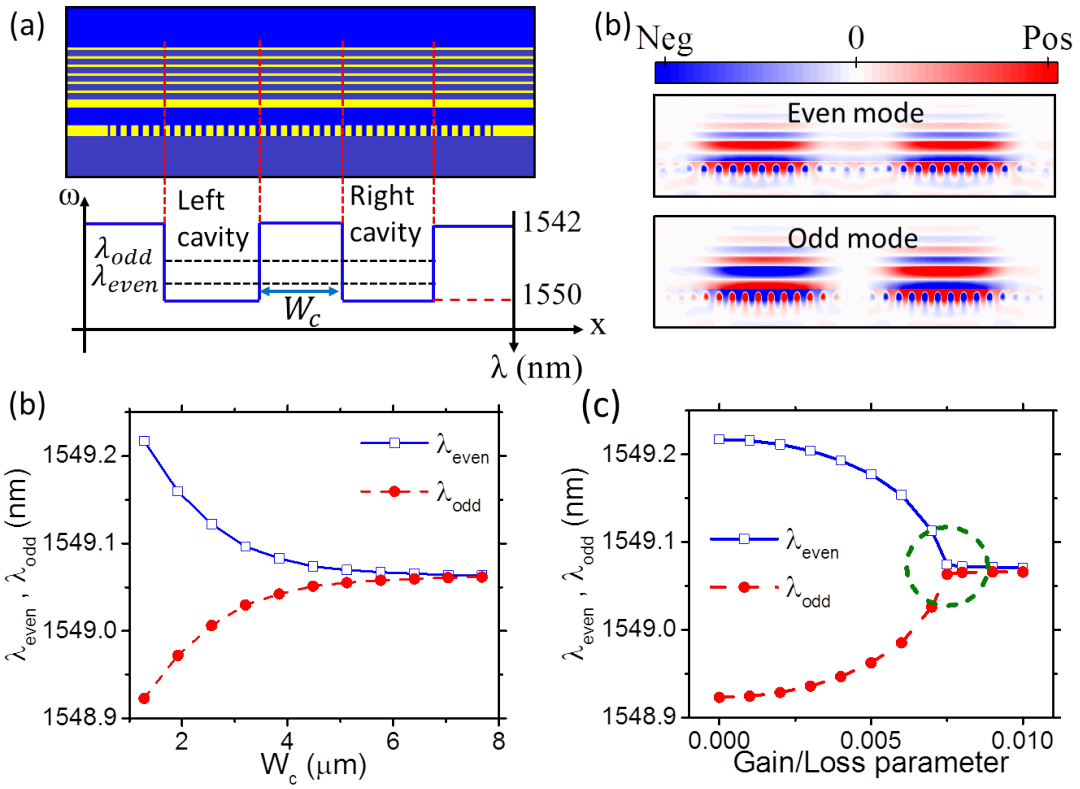

Figure 4.20: (a) Schematic view of a system of two laterally coupled HCG-based vertical cavities. A III-V active region is introduced below the DBR to introduce required gain and loss into the cavities. The corresponding band-edge profile of the structure is plotted below of the schematic with the specified even and odd modes. (b) Mode profiles (real value of H_y) of even and odd modes. (c) Wavelengths of even and odd modes versus lateral spacing between two cavities. (d) Wavelengths of even and odd modes as function of gain/loss parameters, which are the imaginary part of refractive-indices of QWs. The exceptional point, as indicated by a green dotted circle, shows the breaking of PT-symmetry in the structure by increasing the gain/loss parameter. The Structure dimensions and refractive-indices can be found in Appendix C, section C.2.9.

PT-symmetry breaking [48], [49], [54], [55]. As shown in Fig. 4.20(d), the PT symmetry of this coupled cavities can be broken by introducing a gain region in one cavity and a loss region in the other cavity, which reduces the wavelength separation. The exceptional point, as indicated by a green dotted circle, does not show very steep (perpendicular) bifurcation observed in the ideal PT-symmetry broken case [48], [54], [56]. This is due to the unbalanced total gain/loss in the system as explained in Ref. [54], [57].

4.4 Summary

In this chapter, numerical investigation of the HCG/HG-based vertical cavity is conducted. It is shown that the in-plane dispersion is a an important characteristics of the vertical cavities, The dispersion curvature, which is also interpreted as the photon effective mass, influences the optical properties of cavity such as mode confinement and mode spacing. We show that by varying the structural parameters of the grating, it is possible to control the effective mass of the photons, both in terms of sign and absolute value. In this way, it is possible to create a heterostructure, where the photons, in some regions, behave analogous to the conduction band electrons in a solid, while in others, display the properties of valence band holes. This allows the realization of structures with novel types of potential barriers, for instance being realized by a change of photon mass, leading to new types of photon confinement and coupling. Beside numerical simulation, an analytic expression for the cavity dispersion has been derived, which provides considerable insight. The full control over the dispersion characteristics in different directions may be exploited for various applications, e.g., the control of the optical mode and the enhancement of the modulation bandwidth of vertical cavity lasers. It has been shown that the adiabatic heterostructure is advantageous compared to abrupt heterostructure for minimizing the cavity scattering loss. Furthermore, a new laser structure based on an active HG reflector is designed and simulated, which seems advantageous to the HCG-based lasers, due to its more feasible fabrication process and better thermal properties. Finally, a novel system of two coupled cavity is proposed and based on that for the first time, the phenomena of parity-time symmetry breaking in vertical cavities is shown. We believe that the vertical cavity platform, with novel types of reflectors such as HCG and HG, is promising for fundamental physics study, as well as device applications with novel functionalities.

References

[1] J. Gerard, B. Sermage, B. Gayral, B. Legrand, E. Costard, and V. Thierry-Mieg, "Enhanced spontaneous emission by quantum boxes in a monolithic optical microcavity", *Physical Review Letters*, vol. 81, no. 5, pp. 1110–1113, 1998 (cit. on p. 83).

[2] K. J. Vahala, "Optical microcavities", *Nature*, vol. 424, no. 6950, pp. 839–846, 2003 (cit. on p. 83).

[3] H. Deng, G. Weihs, C. Santori, J. Bloch, and Y. Yamamoto, "Condensation of semiconductor microcavity exciton polaritons", *Science*, vol. 298, no. 5591, pp. 199–202, 2002 (cit. on p. 83).

[4] S. Christopoulos, G. B. H. Von Hogersthal, a. J. D. Grundy, P. G. Lagoudakis, a. V. Kavokin, J. J. Baumberg, G. Christmann, R. Butte, E. Feltin, J. F. Carlin, and N. Grandjean, "Room-temperature polariton lasing in semiconductor microcavities", *Physical Review Letters*, vol. 98, no. 12, pp. 1–4, 2007 (cit. on p. 83).

[5] P. Moser, J. A. Lott, P. Wolf, G. Larisch, A. Payusov, N. N. Ledentsov, and D. Bimberg, "Energy-efficient oxide-confined 850-nm VCSELs for long-distance multimode fiber optical interconnects", *IEEE Journal of Selected Topics in Quantum Electronics*, vol. 19, no. 2, p. 7 900 406, 2013 (cit. on p. 83).

[6] P. Westbergh, J. Gustavsson, A. Haglund, M. Skold, A. Joel, and A. Larsson, "High-speed, low-current-density 850 nm VCSELs", *IEEE Journal of Selected Topics in Quantum Electronics*, vol. 15, no. 3, pp. 694–703, 2009 (cit. on p. 83).

[7] H. Dalir and F. Koyama, "29GHz directly modulated 980 nm vertical-cavity surface emitting lasers with bow-tie shape transverse coupled cavity", *Applied Physics Letters*, vol. 103, no. 9, p. 091 109, 2013 (cit. on p. 83).

[8] M. Pelton, C. Santori, J. Vuckovic, B. Zhang, G. S. Solomon, J. Plant, and Y. Yamamoto, "Efficient source of single photons: a single quantum dot in a micropost microcavity", *Physical Review Letters*, vol. 89, no. 23, p. 233 602, 2002 (cit. on p. 83).

[9] I.-S. Chung and J. Mork, "Silicon-photonics light source realized by III–V/Si-grating-mirror laser", *Applied Physics Letters*, vol. 97, no. 15, p. 151 113, 2010 (cit. on pp. 83, 84, 103–105).

[10] S. Boutami, B. Ben Bakir, J.-L. Leclercq, X. Letartre, P. Rojo-Romeo, M. Garrigues, P. Viktorovitch, I. Sagnes, L. Legratiet, and M. Strassner, "Highly selective and compact tunable MOEMS photonic crystal Fabry-Perot filter", *Optics Express*, vol. 14, no. 8, pp. 3129–3137, 2006 (cit. on p. 84).

[11] M. C. Huang, Y. Zhou, and C. J. Chang-Hasnain, "A surface-emitting laser incorporating a high-index-contrast subwavelength grating", *Nature Photonics*, vol. 1, no. 5, pp. 297–297, 2007 (cit. on p. 84).

[12] S. Boutami, B. Benbakir, J.-L. Leclercq, and P. Viktorovitch, "Compact and polarization controlled 1.55 um vertical-cavity surface-emitting laser using single-layer photonic crystal mirror", *Applied Physics Letters*, vol. 91, no. 7, p. 071 105, 2007 (cit. on p. 84).

[13] I.-S. Chung, J. Mork, P. Gilet, and A. Chelnokov, "Subwavelength grating-mirror VCSEL with a thin oxide gap", *IEEE Photonics Technology Letters*, vol. 20, no. 2, pp. 105–107, 2008 (cit. on p. 84).

[14] P. Viktorovitch, B. Ben Bakir, S. Boutami, J.-L. Leclercq, X. Letartre, P. Rojo-Romeo, C. Seassal, M. Zussy, L. di Cioccio, and J.-M. Fedeli, "3D harnessing of light with 2.5D photonic crystals", *Laser and Photonics Reviews*, vol. 4, no. 3, pp. 401–413, 2010 (cit. on pp. 84, 88).

[15] V. Karagodsky, F. G. Sedgwick, and C. J. Chang-Hasnain, "Theoretical analysis of subwavelength high contrast grating reflectors", *Optics Express*, vol. 18, no. 16, pp. 16 973–16 988, 2010 (cit. on p. 84).

[16] I.-S. Chung, V. Iakovlev, A. Sirbu, A. Mereuta, A. Caliman, E. Kapon, and J. Mork, "Broadband MEMS-tunable high-index-contrast subwavelength grating long-wavelength VCSEL", *IEEE Journal of Quantum Electronics*, vol. 46, no. 9, pp. 1245–1253, 2010 (cit. on p. 84).

[17] Z. Wang, B. Zhang, and H. Deng, "Dispersion engineering for vertical microcavities using subwavelength gratings", *Physical Review Letters*, vol. 114, no. 7, p. 073 601, 2015 (cit. on pp. 84, 90, 91).

[18] A. Taghizadeh, J. Mork, and I.-S. Chung, "Vertical-cavity in-plane heterostructures: physics and applications", *Applied Physics Letters*, vol. 107, no. 18, p. 181 107, 2015 (cit. on pp. 84, 88, 89, 92–94).

[19] A. Taghizadeh, J. Mork, and I.-S. Chung, "Effect of in-plane mirror dispersion on vertical cavities based on high-contrast grating mirrors", in *CLEO: 2015*, San Jose: OSA, 2015, SW1F.4 (cit. on pp. 84, 94).

[20] E. M. Purcell, "Spontaneous emission probabilities at radio frequencies", *Physical Review*, vol. 69, p. 681, 1946 (cit. on p. 84).

[21] B. Zhang, S. Brodbeck, Z. Wang, M. Kamp, C. Schneider, S. Hofling, and H. Deng, "Coupling polariton quantum boxes in sub-wavelength grating microcavities", *Applied Physics Letters*, vol. 106, no. 5, p. 051 104, 2015 (cit. on p. 84).

[22] P. Lalanne and J. Hugonin, "Bloch-wave engineering for high-Q, small-V microcavities", *IEEE Journal of Quantum Electronics*, vol. 39, no. 11, pp. 1430–1438, 2003 (cit. on p. 87).

[23] L. H. Frandsen, A. V. Lavrinenko, J. Fage-Pedersen, and P. I. Borel, "Photonic crystal waveguides with semi-slow light and tailored dispersion properties", *Optics Express*, vol. 14, no. 20, pp. 9444–9450, 2006 (cit. on p. 88).

[24] T. F. Krauss, "Slow light in photonic crystal waveguides", *Journal of Physics D: Applied Physics*, vol. 40, no. 9, pp. 2666–2670, 2007 (cit. on p. 88).

[25] A. Figotin and I. Vitebskiy, "Slow light in photonic crystals", *Waves in Random and Complex Media*, vol. 16, no. 3, pp. 293–382, 2008 (cit. on p. 88).

[26] A. Liu, W. Hofmann, and D. Bimberg, "Two dimensional analysis of finite size high-contrast gratings for applications in VCSELs", *Optics Express*, vol. 22, no. 10, pp. 11 804–11 811, 2014 (cit. on p. 89).

[27] L. Carletti, R. Malureanu, J. Mork, and I.-S. Chung, "High-index-contrast grating reflector with beam steering ability for the transmitted beam", *Optics Express*, vol. 19, no. 23, pp. 23 567–23 572, 2011 (cit. on p. 90).

[28] I.-S. Chung, "Study on differences between high contrast grating reflectors for TM and TE polarizations and their impact on VCSEL designs", *Optics Express*, vol. 5, no. 13, pp. 1245–1253, 2015 (cit. on p. 90).

[29] A. Tibaldi, P. Debernardi, and R. Orta, "High-contrast gratings performance issues in tunable VCSELs", *IEEE Journal of Quantum Electronics*, vol. 51, no. 12, pp. 1–7, 2015 (cit. on p. 91).

[30] J. M. Dallesasse, N. Holonyak, A. R. Sugg, T. A. Richard, and N. El-Zein, "Hydrolyzation oxidation of AlGaAs-AlAs-GaAs quantum well heterostructures and superlattices", *Applied Physics Letters*, vol. 57, no. 26, pp. 2844–2846, 1990 (cit. on p. 92).

[31] P. Mackowiak, R. Sarzala, M. Wasiak, and W. Nakwaski, "Design guidelines for fundamental-mode-operated cascade nitride VCSELs", *IEEE Photonics Technology Letters*, vol. 15, no. 4, pp. 495–497, 2003 (cit. on p. 92).

[32] Y. Wu, G. Li, Wupen Yuen, C. Caneau, and C. Chang-Hasnain, "High-yield processing and single-mode operation of passive antiguide region vertical-cavity lasers", *IEEE Journal of Selected Topics in Quantum Electronics*, vol. 3, no. 2, pp. 429–434, 1997 (cit. on p. 92).

[33] H. Martinsson, J. Vukusic, and M. Grabberr, "Transverse mode selection in large-area oxide-confined vertical-cavity surface-emitting lasers using a shallow surface relief", *IEEE Photonics Technology Letters*, vol. 11, no. 12, pp. 1536–1538, 1999 (cit. on p. 92).

[34] E. Soderberg, J. S. Gustavsson, P. Modh, A. Larsson, Z. Zhang, J. Berggren, and M. Hammar, "Suppression of higher order transverse and oxide modes in 1.3 um InGaAs VCSELs by an inverted surface relief", *IEEE Photonics Technology Letters*, vol. 19, no. 5, pp. 327–329, 2007 (cit. on p. 92).

[35] D.-S. Song, S.-H. Kim, H.-G. Park, C.-K. Kim, and Y.-H. Lee, "Single-fundamental-mode photonic-crystal vertical-cavity surface-emitting lasers", *Applied Physics Letters*, vol. 80, no. 21, pp. 3901–3903, 2002 (cit. on p. 92).

[36] C. Sciancalepore, B. B. Bakir, X. Letartre, J.-m. Fedeli, N. Olivier, D. Bordel, C. Seassal, P. Rojo-romeo, P. Regreny, and P. Viktorovitch, "Quasi-3D light confinement in double photonic crystal reflectors VCSELs for CMOS-compatible integration", *Journal of Lightwave Technology*, vol. 29, no. 13, pp. 2015–2024, 2011 (cit. on pp. 92, 100).

[37] G. R. Hadley, "Effective index model for vertical-cavity surface-emitting lasers", *Optics Letters*, vol. 20, no. 13, pp. 1483–1485, 1995 (cit. on p. 92).

[38] M. Charbonneau-Lefort, E. Istrate, M. Allard, J. Poon, and E. H. Sargent, "Photonic crystal heterostructures: waveguiding phenomena and methods of solution in an envelope function picture", *Physical Review B*, vol. 65, no. 12, p. 125 318, 2002 (cit. on pp. 93, 97).

[39] E. Istrate and E. H. Sargent, "Photonic crystal heterostructures and interfaces", *Reviews of Modern Physics*, vol. 78, no. 2, pp. 455–481, 2006 (cit. on p. 93).

[40] G. C. Park, W. Xue, A. Taghizadeh, E. Semenova, K. Yvind, J. Mork, and I.-S. Chung, "Hybrid vertical-cavity laser with lateral emission into a silicon waveguide", *Laser & Photonics Reviews*, vol. 9, no. 3, pp. L11–L15, 2015 (cit. on pp. 93–95, 102, 104).

[41] O. Graydon, "Lasers: bandwidth boost", *Nature Photonics*, vol. 9, no. 2, pp. 75–75, 2015 (cit. on p. 95).

[42] S. Mieda, S. Shiratori, N. Yokota, W. Kobayashi, and H. Yasaka, "Ultrahigh-speed operation of laser diode by cross-gain modulation using external cavity", *Applied Physics Express*, vol. 8, no. 2, p. 022 701, 2015 (cit. on p. 95).

[43] G. C. Park, W. Xue, E. Semenova, K. Yvind, J. Mork, and I. Chung, "III-V/SOI vertical cavity laser with in-plane output into a Si waveguide", in *Optical Fiber Communication Conference*, vol. 1, Washington, D.C.: OSA, 2015, W2A.17 (cit. on p. 102).

[44] J. Ferrara, W. Yang, L. Zhu, P. Qiao, and C. J. Chang-Hasnain, "Heterogeneously integrated long-wavelength VCSEL using silicon high contrast grating on an SOI substrate", *Optics Express*, vol. 23, no. 3, pp. 2512–2523, 2015 (cit. on p. 104).

[45] T. D. Happ, M. Kamp, A. Forchel, J.-L. Gentner, and L. Goldstein, "Two-dimensional photonic crystal coupled-defect laser diode", *Applied Physics Letters*, vol. 82, no. 1, pp. 4–6, 2003 (cit. on p. 105).

[46] M. Bayindir and E. Ozbay, "Heavy photons at coupled-cavity waveguide band edges in a three-dimensional photonic crystal", *Physical Review B*, vol. 62, no. 4, R2247–R2250, 2000 (cit. on p. 105).

[47] S. Hughes, "Coupled-cavity QED using planar photonic crystals", *Physical Review Letters*, vol. 98, no. 8, p. 083 603, 2007 (cit. on p. 105).

[48] B. Peng, S. K. Ozdemir, F. Lei, F. Monifi, M. Gianfreda, G. L. Long, S. Fan, F. Nori, C. M. Bender, and L. Yang, "Parity–time-symmetric whispering-gallery microcavities", *Nature Physics*, vol. 10, no. 5, pp. 394–398, 2014 (cit. on pp. 105, 107).

[49] B. Peng, S. K. Ozdemir, S. Rotter, H. Yilmaz, M. Liertzer, F. Monifi, C. M. Bender, F. Nori, and L. Yang, "Loss-induced suppression and revival of lasing", *Science*, vol. 346, no. 6207, pp. 328–332, 2014 (cit. on pp. 105, 107).

[50] R. P. Stanley, R. Houdre, U. Oesterle, M. Ilegems, and C. Weisbuch, "Coupled semiconductor microcavities", *Applied Physics Letters*, vol. 65, no. 16, pp. 2093–2095, 1994 (cit. on p. 105).

[51] H. Wenzel, U. Bandelow, H.-J. Wunsche, and J. Rehberg, "Mechanisms of fast self pulsations in two-section DFB lasers", *IEEE Journal of Quantum Electronics*, vol. 32, no. 1, pp. 69–78, 1996 (cit. on p. 106).

[52] M. Liertzer, L. Ge, A. Cerjan, A. D. Stone, H. E. Tureci, and S. Rotter, "Pump-induced exceptional points in lasers", *Physical Review Letters*, vol. 108, no. 17, p. 173 901, 2012 (cit. on p. 106).

[53] H. Hodaei, M.-A. Miri, M. Heinrich, D. N. Christodoulides, and M. Khajavikhan, "Parity-time-symmetric microring lasers", *Science*, vol. 346, no. 6212, pp. 975–978, 2014 (cit. on p. 106).

[54] C. M. Bender, M. Gianfreda, S. K. Ozdemir, B. Peng, and L. Yang, "Twofold transition in PT-symmetric coupled oscillators", *Physical Review A*, vol. 88, no. 6, p. 062 111, 2013 (cit. on p. 107).

[55] H. Ramezani, H.-K. Li, Y. Wang, and X. Zhang, "Unidirectional spectral singularities", *Physical Review Letters*, vol. 113, no. 26, p. 263 905, 2014 (cit. on p. 107).

[56] M. Brandstetter, M. Liertzer, C. Deutsch, P. Klang, J. Schoberl, H. E. Tureci, G. Strasser, K. Unterrainer, and S. Rotter, "Reversing the pump dependence of a laser at an exceptional point", *Nature communications*, vol. 5, no. May, p. 4034, 2014 (cit. on p. 107).

[57] H. Benisty, C. Yan, A. Degiron, and A. Lupu, "Healing near-PT-symmetric structures to restore their characteristic singularities: analysis and examples", *Journal of Lightwave Technology*, vol. 30, no. 16, pp. 2675–2683, 2012 (cit. on p. 107).

Mathematics is the most exact science, and its conclusions are capable of absolute proof. But this is so only because mathematics does not attempt to draw absolute conclusions. All mathematical truths are relative, conditional.

— Charles Proteus Steinmetz

5 Conclusion and Outlook

Contents

5.1 Summary

The main goal of this work was to understand the physics of novel subwavelength gratings, as well as vertical cavity lasers incorporating them. This understanding guides us to design vertical cavity lasers with either performances beyond the conventional vertical-cavity surface-emitting lasers (VCSELs) with distributed Brag reflectors (DBRs) such as very small modal volume, high optical confinement factor or very long photon life-time, or new functionalities such as in-plane light emission into a silicon waveguide with very high out-coupling efficiency. Particularly, this capability of in-plane light emission is very attractive for integrated light sources in future optical interconnect applications.

For modeling optical properties of vertical cavity lasers, an optical software tool based on the Fourier modal method (FMM), which solves fully-vectorial Maxwell's equations in three-dimensional (3D) space, has been implemented. Several different techniques for computing the resonance frequency and quality-factor (Q-factor) of a cavity mode have been compared, and their pros and cons have been discussed. Particularly, the quasi-normal mode approach with real frequency is considerably

more efficient numerically compared to other methods, due to its capability of determining the resonance frequency and Q-factor of several transverse modes at once. Furthermore, it is shown that the uncertainty in the Q-factor is several orders of magnitude larger than the uncertainty in the resonance frequency. On top of that, a method to simplify 3D simulations to lower dimensional simulations is suggested, which enables us to perform fast simulations for designing heterostructure before doing a thorough 3D simulation.

We have suggested a novel grating structure, referred to as hybrid grating (HG), which consists of a sub-wavelength grating layer and an unpatterned high-refractive-index cap layer. It has been shown numerically and experimentally that the HG reflector can provide a near-unity reflectivity in a broad wavelength range, which surpasses that of the well-known high-index-contrast grating (HCG). The cap layer introduces more guided-mode resonances (GMRs) without loss of peak reflectivity, which leads to this broader high-reflectivity bandwidth [1]. Furthermore, the reflection process is shown to originate mainly from the propagating modes in the structure. A Monte Carlo analysis illustrates that the HG high reflectivity is prone to the common fabrication errors, which is also validated by the experiments on the fabricated structure [2]. On top of that, it is shown that the HG can be employed as an ultrahigh Q-factor resonator [3]. The physics study of the resonances show that two propagating modes in the grating layer are contributed simultaneously in the resonance process and the cancellation of the 0^{th} harmonic component of these two modes at the interfaces to surrounding layers leads to high-Q resonances. These types of resonances of an HG structure differ from those of grating filters, highlighting that HG resonators may achieve Q-factors that are several orders of magnitude higher than conventional GMR filters. From application point of view, the structures based on the HG can be advantageous compared to the ones using conventional HCG.

The HG can be employed as a broadband reflector in a vertical cavity laser, since it can provide high-reflectivity value, which is relatively insensitive to the fabrication imperfections. If an active material is included as part of the cap layer, a novel vertical cavity laser structure can be formed with a more feasible fabrication process and better heat dissipation compared to the HCG-based ones. Moreover, an standalone HG can be used as a resonator and a very compact laser structure is possible by incorporating a gain material in the cap layer which appears promising, featuring a smaller series resistance, less surface recombination loss, and a better heat dissipation capability than the HCG resonator-based laser structures. Even though, for the typical fabrication errors and finite extension of 10 to 15 μm, the

Q-factor of a HG resonator drops from an ultrahigh value to a moderate value, it is still sufficient for laser applications.

Finally, the cavity dispersion is shown to be a very important characteristics of the vertical cavities with HCG or HG reflectors [4]. An analytic expression is derived which indicates that the dispersion has contributions from both mirrors through their reflectivity phase response as well as nominal cavity through its thickness [5]. The HCG and HG reflectors can be designed to be the dominant contributor to the dispersion, which is not the case for the conventional DBRs. Therefore, the dispersion curvatures of the HCG/HG-based vertical cavities can be engineered to achieve different values in different directions, simply by changing the grating parameters. Since the dispersion curvature can be interpreted as a photon effective mass, depending on the curvature sign the photons behave analogous to the conduction band electrons or valence band holes in a solid. The design freedom, obtained by engineering the photon effective mass, enables exotic configurations of heterostructure that may be of interest for various applications such as a photonic well with conduction band like well and a valence band like barrier. Engineering the cavity dispersion can be used for enhancing the Purcell factor or making a polariton-based laser due to increasing the density of states or equivalently the photon effective mass [6]. Furthermore, in Si-integrated photonics, a laser source that can output light into a Si waveguide is essential [7], and it is shown that in HGG-based vertical cavity laser the light can be coupled to an in-plane output waveguide [8]. The design rules for achieving a high out-coupling efficiency into the in-plane waveguide are discussed and the in-plane out-coupling efficiency as high as 68% is achieved in design. At the end, a system of two laterally coupled vertical cavities has been proposed and investigated, which exhibits the spontaneous breaking of parity-time (PT) symmetry [5]. Since this coupled cavity system can be realized as an electrically pumped device, it can result in device applications for PT-symmetry breaking phenomenon.

5.2 Future Works

In this section, we list several possible extensions and outlooks of this work, and we believe this list can be extended.

- For accurate simulation of a laser diode, all optical, electrical and thermal phenomena should be modeled [9]. In this dissertation, the FMM has been implemented for modeling the optical phenomena. However, modeling electrical and thermal effects and the interaction of all three phenomena

is highly required. Therefore, *efficient and accurate implementation and integration of the electrical and thermal simulators with the optical simulator is seen as the next step for developing a complete laser simulator.*

- The FMM is an accurate and physically-attractive approach for simulating nanophotonics devices, and particularly it is advantageous compared to finite-difference time-domain and finite element methods, for simulating periodic structures such as the ones include the HCG or HG. In addition, the concepts of adaptive spatial resolution (ASR) [10] and perfectly matched layer (PML) [11] improve the performance of this method considerably, and also broaden its applications. Although, we have implemented these two techniques, *a systematic study on the performance improvement caused by both the ASR and PML techniques is missed in the literature and seems necessary.*

- The FMM has some limitations, which restricts its applications for simulating optical phenomena in large 3D devices. For instance, although the convergence of the calculation results can be tested for 2D problems, it is practically impossible to check the convergence in 3D cases due to the enormous time required. Furthermore, the matrices involved in the FMM are not sparse, which requires huge amount of memory to store them. *Thus, for 3D problems any attempt for simplifying the modeling is extremely useful and well-appreciated.* The proposed method for HCG/HG-based cavities by employing lower dimensional structures for designing and optimizing the in-plane heterostructure, is an example of such a simplified approach. In addition, cavity dispersion concept with the well-known envelope approximation technique is a fast approximate and also physically-intuitive method for modeling the complex 3D vertical cavity heterostructures.

- All the numerical studies in this thesis are performed on the 1D grating structures. *However, similar studies can be conducted on the 2D gratings.* For instance, the concept of cavity dispersion can be applied to vertical cavities with 2D grating reflectors. We believe that for 2D gratings, the possibility for designing anisotropic dispersion in different directions is increased and new functionalities can be expected due to this possibility. Furthermore, our concentration was only on vertical cavities, which consist of a HCG/HG reflector with a conventional DBR, i.e. DBR-HCG or DBR-HG structures. However, vertical cavities in which both reflectors are formed by HCG or HG or a combination of them are also attractive such as HCG-HCG [12], HG-HG, and HCG-HG structures. *Theoretical investigation of vertical cavity structures with double grating reflectors is a formal extension of this work.*

- From experimental point of view, only a few vertical cavity devices were fabricated, mainly for demonstrating the in-plane light emission capability. However, many of the interesting phenomena introduced in this thesis have not been observed experimentally yet. Therefore, *fabrication and measurement of the proposed devices is essential for validating the theory provided here, such as illustrating parity-time symmetry breaking or boosting laser speed by photon-photon resonances.*

- For Si-integrated light source applications, the HCG/HG-based vertical cavity lasers seem promising. In our group, we have demonstrated a proof-of-concept optically pumped HCG-based laser with in-plane emission to a silicon waveguide recently [8], [13], and an electrically-pumped HG-based laser with in-plane light emission is planned to be fabricated soon, which has a more feasible fabrication process compared to the HCG-based one. Even though, we have shown the possibility of in-plane emission in this structure, *there are still rooms for understanding the mechanism of in-plane coupling and also engineering the out-coupling efficiency for the maximum achievable value.*

References

[1] A. Taghizadeh, G. C. Park, J. Mork, and I.-S. Chung, "Hybrid grating reflector with high reflectivity and broad bandwidth", *Optics Express*, vol. 22, no. 18, pp. 21 175–21 184, 2014 (cit. on p. 114).

[2] G. C. Park, A. Taghizadeh, and I.-S. Chung, "Hybrid grating reflectors: origin of ultrabroad stopband", *Submitted to Applied Physics Letters*, 2015 (cit. on p. 114).

[3] A. Taghizadeh, J. Mork, and I.-S. Chung, "Ultracompact resonator with high quality-factor based on a hybrid grating structure", *Optics Express*, vol. 23, no. 11, pp. 14 913–14 921, 2015 (cit. on p. 114).

[4] A. Taghizadeh, J. Mork, and I.-S. Chung, "Effect of in-plane mirror dispersion on vertical cavities based on high-contrast grating mirrors", in *CLEO: 2015*, San Jose: OSA, 2015, SW1F.4 (cit. on p. 115).

[5] A. Taghizadeh, J. Mork, and I.-S. Chung, "Vertical-cavity in-plane heterostructures: physics and applications", *Applied Physics Letters*, vol. 107, no. 18, p. 181 107, 2015 (cit. on p. 115).

[6] Z. Wang, B. Zhang, and H. Deng, "Dispersion engineering for vertical microcavities using subwavelength gratings", *Physical Review Letters*, vol. 114, no. 7, p. 073 601, 2015 (cit. on p. 115).

[7] I.-S. Chung and J. Mork, "Silicon-photonics light source realized by III–V/Si-grating-mirror laser", *Applied Physics Letters*, vol. 97, no. 15, p. 151 113, 2010 (cit. on p. 115).

[8] G. C. Park, W. Xue, A. Taghizadeh, E. Semenova, K. Yvind, J. Mork, and I.-S. Chung, "Hybrid vertical-cavity laser with lateral emission into a silicon waveguide", *Laser & Photonics Reviews*, vol. 9, no. 3, pp. L11–L15, 2015 (cit. on pp. 115, 117).

[9] A. Mutig, *High Speed VCSELs for Optical Interconnects*. Berlin, Heidelberg: Springer, 2011 (cit. on p. 115).

[10] G. Granet, "Reformulation of the lamellar grating problem through the concept of adaptive spatial resolution", *Journal of the Optical Society of America A*, vol. 16, no. 10, pp. 2510–2516, 1999 (cit. on p. 116).

[11] J. P. Hugonin and P. Lalanne, "Perfectly matched layers as nonlinear coordinate transforms: a generalized formalization", *Journal of the Optical Society of America A*, vol. 22, no. 9, pp. 1844–1849, 2005 (cit. on p. 116).

[12] C. Sciancalepore, B. B. Bakir, X. Letartre, J. Harduin, N. Olivier, C. Seassal, J.-M. Fedeli, and P. Viktorovitch, "CMOS-compatible ultra-compact 1.55-um emitting VCSELs using double photonic crystal mirrors", *IEEE Photonics Technology Letters*, vol. 24, no. 6, pp. 455–457, 2012 (cit. on p. 116).

[13] G. C. Park, W. Xue, E. Semenova, K. Yvind, J. Mork, and I. Chung, "III-V/SOI vertical cavity laser with in-plane output into a Si waveguide", in *Optical Fiber Communication Conference*, vol. 1, Washington, D.C.: OSA, 2015, W2A.17 (cit. on p. 117).

Appendices

The heart of animals is the foundation of their life, the sovereign of everything within them, the sun of their microcosm, that upon which all growth depends, from which all power proceeds.

— William Harvey

A Homogeneous Layer Eigenmodes

For a constant permittivity ϵ_r, it is easy to show that $\mathcal{E}_i = \epsilon_r \mathcal{M}_i$, $i = \bar{x}, \bar{y}, \bar{z}$. Therefore, $\mathbf{P}$ and $\mathbf{Q}$ in Eqs. (2.18) will simplify considerably as:

$$\mathbf{P} = \frac{1}{\epsilon_r}\mathbf{Q} = \begin{pmatrix} \mathbf{F}_{\bar{x}}\mathbf{K}_{\bar{x}}\mathcal{M}_{\bar{z}}^{-1}\mathbf{F}_{\bar{y}}\mathbf{K}_{\bar{y}} & \epsilon_r\mathcal{M}_y - \mathbf{F}_{\bar{x}}\mathbf{K}_{\bar{x}}\mathcal{M}_{\bar{z}}^{-1}\mathbf{F}_{\bar{x}}\mathbf{K}_{\bar{x}} \\ \mathbf{F}_{\bar{y}}\mathbf{K}_{\bar{y}}\mathcal{M}_{\bar{z}}^{-1}\mathbf{F}_{\bar{y}}\mathbf{K}_{\bar{y}} - \epsilon_r\mathcal{M}_x & -\mathbf{F}_{\bar{y}}\mathbf{K}_{\bar{y}}\mathcal{M}_{\bar{z}}^{-1}\mathbf{F}_{\bar{x}}\mathbf{K}_{\bar{x}} \end{pmatrix} \tag{A.1a}$$

After some algebra, the eigenvalue matrix $\mathbf{\Omega} = \mathbf{PQ}$ becomes:

$$\mathbf{\Omega} = \begin{pmatrix} \mathbf{\Omega}_{11} & \mathbf{\Omega}_{12} \\ \mathbf{\Omega}_{21} & \mathbf{\Omega}_{22} \end{pmatrix} = \mathbf{Y} - \epsilon_r\mathbf{I}, \tag{A.2a}$$

$$\mathbf{Y}_{11} = \mathbf{F}_{\bar{x}}\mathbf{K}_{\bar{x}}\mathcal{M}_{\bar{z}}^{-1}\mathbf{F}_{\bar{x}}\mathbf{K}_{\bar{x}}\mathcal{M}_{\bar{x}} + \mathcal{M}_{\bar{y}}\mathbf{F}_{\bar{y}}\mathbf{K}_{\bar{y}}\mathcal{M}_{\bar{z}}^{-1}\mathbf{F}_{\bar{y}}\mathbf{K}_{\bar{y}}, \tag{A.2b}$$

$$\mathbf{Y}_{22} = \mathcal{M}_{\bar{x}}\mathbf{F}_{\bar{x}}\mathbf{K}_{\bar{x}}\mathcal{M}_{\bar{z}}^{-1}\mathbf{F}_{\bar{x}}\mathbf{K}_{\bar{x}} + \mathbf{F}_{\bar{y}}\mathbf{K}_{\bar{y}}\mathcal{M}_{\bar{z}}^{-1}\mathbf{F}_{\bar{y}}\mathbf{K}_{\bar{y}}\mathcal{M}_{\bar{y}}, \tag{A.2c}$$

$$\mathbf{Y}_{12} = \mathbf{Y}_{21} = \mathbf{O}, \tag{A.2d}$$

where $\mathbf{Y}$ is an auxiliary matrix. For free-space, $\epsilon_r = 1$, the eigenvalue problem is $(\mathbf{Y} - \mathbf{I})\mathbf{W}_0 = \mathbf{\Gamma}_0^2\mathbf{W}_0$. We can easily show that $\mathbf{W}_0$ also diagonalizes the matrix $\mathbf{Y} - \epsilon_r\mathbf{I}$:

$$(\mathbf{Y} - \epsilon_r\mathbf{I})\mathbf{W}_0 = (\mathbf{Y} - \mathbf{I})\mathbf{W}_0 + (1 - \epsilon_r)\mathbf{W}_0 = \left[\mathbf{\Gamma}_0^2 + (1 - \epsilon_r)\right]\mathbf{W}_0 \tag{A.3}$$

which shows an eigenvalue problem with eigenvalue of $\gamma_0^2 + (1 - \epsilon_r)$. Therefore, if the eigenvalue problem is solved for free-space, Eq. (A.3) can be employed for determining the eigenmodes of all other homogeneous layers.

Everything should be made as simple as possible, but no simpler.

— Albert Einstein

B

Redheffer Star Product Variants

There are other variants of Redheffer star product, which are more efficient numerically in the cases where only some of the S-matrices are required. The following equations just need one matrix inversion compared to Eqs. 2.27, but at the same time require one additional matrix multiplication:

$$\mathbf{S}_{11}^{(AB)} = \mathbf{S}_{11}^{(A)} + \mathbf{S}_{12}^{(A)}\left[\mathbf{I} - \mathbf{S}_{11}^{(B)}\mathbf{S}_{22}^{(A)}\right]^{-1}\mathbf{S}_{11}^{(B)}\mathbf{S}_{21}^{(A)}, \tag{B.1a}$$

$$\mathbf{S}_{12}^{(AB)} = \mathbf{S}_{12}^{(A)}\left[\mathbf{I} - \mathbf{S}_{11}^{(B)}\mathbf{S}_{22}^{(A)}\right]^{-1}\mathbf{S}_{12}^{(B)}, \tag{B.1b}$$

$$\mathbf{S}_{21}^{(AB)} = \mathbf{S}_{21}^{(B)}\mathbf{S}_{21}^{(A)} + \mathbf{S}_{21}^{(B)}\mathbf{S}_{22}^{(A)}\left[\mathbf{I} - \mathbf{S}_{11}^{(B)}\mathbf{S}_{22}^{(A)}\right]^{-1}\mathbf{S}_{11}^{(B)}\mathbf{S}_{21}^{(A)}, \tag{B.1c}$$

$$\mathbf{S}_{22}^{(AB)} = \mathbf{S}_{22}^{(B)} + \mathbf{S}_{21}^{(B)}\mathbf{S}_{22}^{(A)}\left[\mathbf{I} - \mathbf{S}_{11}^{(B)}\mathbf{S}_{22}^{(A)}\right]^{-1}\mathbf{S}_{12}^{(B)}. \tag{B.1d}$$

If only $\mathbf{S}_{22}$ is required (to update it, $\mathbf{S}_{12}$ should also be calculated), these expressions are more efficient numerically, since they require one matrix inversion and six distinct matrix multiplications compare to the Eqs. (2.27), which require two matrix inversions and six distinct matrix multiplications. Similarly, the following expressions are more efficient numerically when only $\mathbf{S}_{11}$ is needed:

$$\mathbf{S}_{11}^{(AB)} = \mathbf{S}_{11}^{(A)} + \mathbf{S}_{12}^{(A)}\mathbf{S}_{11}^{(B)}\left[\mathbf{I} - \mathbf{S}_{22}^{(A)}\mathbf{S}_{11}^{(B)}\right]^{-1}\mathbf{S}_{21}^{(A)}, \tag{B.2a}$$

$$\mathbf{S}_{12}^{(AB)} = \mathbf{S}_{12}^{(A)}\mathbf{S}_{12}^{(B)} + \mathbf{S}_{12}^{(A)}\mathbf{S}_{11}^{(B)}\left[\mathbf{I} - \mathbf{S}_{22}^{(A)}\mathbf{S}_{11}^{(B)}\right]^{-1}\mathbf{S}_{22}^{(A)}\mathbf{S}_{12}^{(B)}, \tag{B.2b}$$

$$\mathbf{S}_{21}^{(AB)} = \mathbf{S}_{21}^{(B)}\left[\mathbf{I} - \mathbf{S}_{22}^{(A)}\mathbf{S}_{11}^{(B)}\right]^{-1}\mathbf{S}_{21}^{(A)}, \tag{B.2c}$$

$$\mathbf{S}_{22}^{(AB)} = \mathbf{S}_{22}^{(B)} + \mathbf{S}_{21}^{(B)}\left[\mathbf{I} - \mathbf{S}_{22}^{(A)}\mathbf{S}_{11}^{(B)}\right]^{-1}\mathbf{S}_{22}^{(A)}\mathbf{S}_{12}^{(B)}. \tag{B.2d}$$

It is going to be necessary that everything that happens in a finite volume of space and time would have to be analyzable with a finite number of logical operations. The present theory of physics is not that way, apparently.

— Richard Phillips Feynman

C

Simulation Parameters

Contents

In this appendix, the structural dimensions and refractive-indices for some of the simulated structures in the thesis are reported. If not stated otherwise, a 0.5μm-thick perfectly matched layer (PML) is employed in the x-direction boundaries for two-dimensional (2D) and three-dimensional (3D) simulations, and similar one in the y-direction boundaries for 2.5D and 3D simulations. Also, for vertical cavity in-plane (VCI) heterostructures, the grating bar width is varied while its period is kept constant. The number of Fourier terms is chosen according to the discussion in chapter 2.

No.	Layer	Refractive index	Thickness	Comment
1	Superstrate	n_{sup}=1	$t_{sup} = \infty$	Infinite half space
2, 3	DBR-h DBR-l	n_h=3.48 n_l=1.48	t_h=111.4 nm t_l=261.8 nm	4.5-pairs DBR
4	Cavity	n_c=1.0	t_c=704.4 nm	Nominal cavity
5	Grating	n_h=3.48, n_l=1.0	t_g=430 nm	Λ_g=640 nm, W_g=396.8 nm, N_g=14
6	Substrate	n_{sub}=1.48	$t_{sub} = \infty$	Infinite half space

Table C.1: Structure dimensions and refractive-indices related to Fig. 2.9.

C.1 Chapter 2

C.1.1 Figure 2.9

Table C.1 is related to Fig. 2.9. The simulated structure is a 2D HCG-based vertical cavity with 0.5λ-long air cavity. The HCG is designed to be highly reflective for a TM-polarized light at 1550 nm wavelength and it is terminated simply by stopping the periodic modulation without any specific transverse confinement scheme.

C.1.2 Table 2.3

The simulated structure is a 2D HCG-based vertical cavity with an extra active region made of InP above the cavity, and related to the Table 2.3. There is a gain region at the peak of field profile, where an imaginary value is introduced in the refractive-index of that section. The HCG is designed to be highly reflective for a TM-polarized light at 1550 nm wavelength and it is terminated simply by stopping the periodic modulation without any specific transverse confinement scheme.

C.2 Chapter 4

C.2.1 Figure 4.9

Tables C.3 and C.4 are related to Figs. 4.9(a) and 4.9(b), respectively. The simulated structure is a 2D HCG-based vertical cavity with 0.5λ-long air cavity. The HCG is designed to be highly reflective for a TM-polarized light at 1550 nm wavelength. A VCI heterostructure (a photonic well) is formed by changing the grating bar width while keeping the grating period constant.

No.	Layer	Refractive index	Thickness	Comment
1	Superstrate	n_{sup}=1	$t_{sup} = \infty$	Infinite half space
2, 3	DBR-h DBR-l	n_h=3.48 n_l=1.48	t_h=111.4 nm t_l=261.8 nm	4 pairs DBR
4	Active	n_{a1}=3.1661	t_{a1}=191.7 nm	Top contact
5	Active	n_{a2}=3.1661 3.1661+jn_i	t_{a2}=30.0 nm	Gain region 12 μm in the middle
6	Active	n_{a3}=3.1661	t_{a3}=384.1 nm	Bottom contact
7	Cavity	n_c=1.0	t_c=725.1 nm	Nominal cavity
8	Grating	n_h=3.48, n_l=1.0	t_g=430 nm	Λ_g=640 nm, W_g=371.2 nm, N_g=14
9	Substrate	n_{sub}=1.48	$t_{sub} = \infty$	Infinite half space

Table C.2: Structure dimensions and refractive-indices related to Table 2.3.

No.	Layer	Refractive index	Thickness	Comment
1	Superstrate	n_{sup}=1	$t_{sup} = \infty$	Infinite half space
2, 3	DBR-h DBR-l	n_h=3.48 n_l=1.48	t_h=111.4 nm t_l=261.8 nm	6.5 pairs DBR
4	Cavity	n_c=1.0	t_c=725.1 nm	Nominal cavity
5	Grating	n_h=3.48, n_l=1.0	t_g=430 nm	Barrier: Λ_g=640 nm, W_g=361.9 nm, N_g=6 Well: Λ_g=640 nm, W_g=371.2 nm, N_g=16
6	Substrate	n_{sub}=1.48	$t_{sub} = \infty$	Infinite half space

Table C.3: Structure dimensions and refractive-indices related to Fig. 4.9(a). The photon effective mass in x-direction is calculated to be $1/m_x$=0.212c^2.

C.2.2 Figure 4.10

The simulated structure is a HCG-based vertical cavity with 0.5λ-long air cavity. Tables C.5 is related to Fig. 4.10(a), and it is based on 2D simulation. To vary the photon effective mass, the design wavelength λ_d varies from 1450 nm to 1580 nm, while the grating parameters in the well are kept constant. In this wavelength range, the reflectivity amplitude of the HCG mirror is above 99.88%. By changing the wavelength, the central design wavelength of the DBR (consequently its layer thicknesses) are varied to have the same reflectivity amplitude from top mirror

No.	Layer	Refractive index	Thickness	Comment
1	Superstrate	n_{sup}=1	$t_{sup} = \infty$	Infinite half space
2, 3	DBR-h DBR-l	n_h=3.48 n_l=1.48	t_h=111.4 nm t_l=261.8 nm	6.5 pairs DBR
4	Cavity	n_c=1.0	t_c=692.1 nm	Nominal cavity
5	Grating	n_h=3.48, n_l=1.0	t_g=420 nm	Barrier: Λ_g=640 nm, W_g=435.2 nm, N_g=6 Well: Λ_g=640 nm, W_g=459.1 nm, N_g=16
6	Substrate	n_{sub}=1.48	$t_{sub} = \infty$	Infinite half space

Table C.4: Structure dimensions and refractive-indices related to Fig. 4.9(b). The photon effective mass in x-direction is calculated to be $1/m_x$=-0.402c^2.

No.	Layer	Refractive index	Thickness	Comment
1	Superstrate	n_{sup}=1	$t_{sup} = \infty$	Infinite half space
2, 3	DBR-h DBR-l	n_h=3.48 n_l=1.48	$t_h = \lambda_d/4n_h$ $t_l = \lambda_d/4n_l$	6.5 pairs DBR
4	Cavity	n_c=1.0	t_c from Eq. (4.1)	Nominal cavity
5	Grating	n_h=3.48, n_l=1.0	t_g=430 nm	Barrier(+): Λ_g=640 nm, W_g=361.9 nm, N_g=6 Barrier(−): Λ_g=640 nm, W_g=389.8 nm, N_g=6 Well: Λ_g=640 nm, W_g=371.2 nm, N_g=16
6	Substrate	n_{sub}=1.48	$t_{sub} = \infty$	Infinite half space

Table C.5: Structure dimensions and refractive-indices related to Fig. 4.10(a). For plotting the graph the design wavelength is changed from 1450 nm to 1580 nm range in the high reflection bandwidth of the HCG. Barrier(±) shows the grating parameters in barrier section for positive/negative effective mass, respectively.

across the graph. Due to the HCG mirror phase change and also design wavelength, the nominal cavity thickness should be modified using Eq. (4.1). For grating parameters in the barrier region, W_g is increased or decreased by 5% depending on the sign of photon effective mass to form a relatively large barrier.

Figure 4.10(b) shows 3D simulation results for a HCG-based vertical cavity structure. All layer thicknesses and refractive-indices are shown in Table C.6. All

layers, except grating layer, are assumed to be homogeneous layers, i.e. they are extended in x- and y-directions to the end of simulation domain. The grating bar widths in x- and y-directions are changed in the barrier region as shown schematically in Fig. 4.8(b). The L_y is 6 μm.

No.	Layer	Refractive index	Thickness	Comment
1	Superstrate	n_{sup}=1	$t_{sup} = \infty$	Infinite half space
2, 3	DBR-h DBR-l	n_h=3.48 n_l=1.48	t_h=111.4 nm t_l=261.8 nm	6.5 pairs DBR
4	Cavity	n_c=1.0	t_c=709.3 nm	Nominal cavity
5	Grating	n_h=3.48 n_l=1.0	t_g=430 nm	Barrier: Λ_g=640 nm, W_g=374.8 nm, N_g=6 Well: Λ_g=640 nm, W_g=390.4 nm, N_g=12
6	Substrate	n_{sub}=1.48	$t_{sub} = \infty$	Infinite half space

Table C.6: Structure dimensions and refractive-indices related to Fig. 2(d). The photon effective mass in x- and y-directions are calculated to be $1/m_x$=0.08c^2 and $1/m_y$=1.0c^2, receptively.

C.2.3 Figure 4.11

Table C.7 is related to Fig. 4.11. The simulated structure is a 2D HCG-based vertical cavity with 0.5λ-long air cavity. The HCG is designed to be highly reflective for a TM-polarized light at 1550 nm wavelength. A photonic well with different left and right barrier is formed by changing the grating bar width while keeping the grating period constant.

C.2.4 Figure 4.12

The structure dimensions and refractive-indices are the same as those in tables C.3 and C.4, respectively. The only difference is that the number of grating periods are N_g=14 and N_g=8, in the well and barrier regions, respectively. To vary $\Delta\omega$, the grating bar width W_g in the barrier region is changed compared to the well section, from 371.2 nm to 352.6 nm for Fig. 4.12(a) and from 459.1 nm to 491.2 nm for Fig. 4.12(b).

No.	Layer	Refractive index	Thickness	Comment
1	Superstrate	n_{sup}=1	$t_{sup} = \infty$	Infinite half space
2, 3	DBR-h DBR-l	n_h=3.48 n_l=1.48	t_h=111.4 nm t_l=261.8 nm	6 pairs DBR
4	Cavity	n_c=1.0	t_c=725.1 nm	Cavity thickness in left barrier is t_c=698 nm
5	Grating	n_g=3.48	t_g=430 nm	Barrier(left): Λ_g=640 nm, W_g=345.6 nm, N_g=8 Barrier(right): Λ_g=650 nm, W_g=429 nm, N_g=8 Well: Λ_g=640 nm, W_g=371.2 nm, N_g=12
6	Substrate	n_{sub}=1.48	$t_{sub} = \infty$	Infinite half space

Table C.7: Structure dimensions and refractive-indices related to Fig. 4.11.

C.2.5 Figure 4.15

Table C.8 is related to Fig. 4.15. The simulated structure is a 2D HG-based VCI heterostructure with 0.5λ-long air cavity. The HCG is designed to be highly reflective for a TM-polarized light at 1550 nm wavelength. For Fig. 4.15(a), the well size is kept constant at 8 grating periods ($N_{g,well}$=8) and the barrier length is varied from 2 to 16 periods ($N_{g,barrier}$=2-14) for three different barrier height; blue graph $W_{g,barrier}$=367.5 nm, red graph $W_{g,barrier}$=363.8 nm, and green graph $W_{g,barrier}$=360.1 nm. For Fig. 4.15(b), the barrier length is kept fixed at 8 grating periods ($N_{g,barrier}$=8), and the well length is varied from from 4 to 16 periods ($N_{g,barrier}$=4-16) for three different barrier type; blue graph is adiabatic-type barrier $W_{g,barrier}$=371.2-363.8 nm, red graph is abrupt-type barrier $W_{g,barrier}$=367.5 nm, and green graph is adiabatic-type barrier $W_{g,barrier}$=363.8 nm.

C.2.6 Figure 4.16

Table C.9 is related to Fig. 4.16. The simulated structure is a 2D HG-based vertical cavity which is designed for an electrically-pumped laser. The HG is designed to be highly reflective for a TM-polarized light at 1554.2 nm wavelength, since the gain peak occurs at this wavelength at laser working temperature. A 0.5λ-long SiO_2 cavity and a DBR stack made of amorphous Si and SiO_2 is used. It is assumed that the cap layer is extended for 3 μm beyond the grating region.

No.	Layer	Refractive index	Thickness	Comment
1	Superstrate	n_{sup}=1	$t_{sup} = \infty$	Infinite half space
2, 3	DBR-h DBR-l	n_h=3.48 n_l=1.48	t_h=111.4 nm t_l=261.8 nm	6.5 pairs DBR
4	Cavity	n_c=1.0	t_c=725.1 nm	Nominal cavity
5	Grating	n_h=3.48, n_l=1.0	t_g=430 nm	Barrier: Λ_g=640 nm, W_g=c.f. text, N_g=c.f. text Well: Λ_g=640 nm, W_g=371.2 nm, N_g=c.f. text
6	Substrate	n_{sub}=1.48	$t_{sub} = \infty$	Infinite half space

Table C.8: Structure dimensions and refractive-indices related to Fig. 4.15.

No.	Layer	Refractive index	Thickness	Comment
1	Superstrate	n_{sup}=1	$t_{sup} = \infty$	Infinite half space
2, 3	DBR-h DBR-l	n_h=2.923 n_l=1.48	t_h=132.9 nm t_l=262.5 nm	4.5 pairs DBR
4	Cavity	n_c=1.48	t_c=559.7 nm	Nominal cavity
5	Top contact	n_{tc}=3.1661-j1.3e-4	t_{tc}=260 nm	N-doped 1.5e18
6	Wells and barriers	n_{nc}=3.1661	t_{wb}=105.5 nm	Undoped, 7 6.5nm-QWs with 7.5nm-barriers
7	Cladding	n_{clad}=3.35-j3.7e-5	t_{clad}=43 nm	P-doped 1.0e18
8	TJ (P++)	n_{pTJ}=3.53-j7.4e-4	t_{pTJ}=20 nm	P-doped 2.0e18
9	TJ (N++)	n_{nTJ}=3.53-j1.7e-3	t_{nTJ}=15 nm	N-doped 2.0e18
10	Bottom contact	n_{bc}=3.1661-j1.3e-4	t_{bc}=380 nm	N-doped 1.5e18
11	Grating	n_h=3.48, n_l=1.0	t_g=500 nm	Barrier: Λ_g=845 nm, W_g=354.9-390.4 nm, N_g=8 Well: Λ_g=845 nm, W_g=390.4 nm, N_g=8
12	Substrate	n_{sub}=1.48	$t_{sub} = \infty$	Infinite half space

Table C.9: Structure dimensions and refractive-indices related to Fig. 4.16.

No.	Layer	Refractive index	Thickness	Comment
1	Superstrate	n_{sup}=1.48	$t_{sup} = \infty$	Infinite half space
2	Grating	n_h=3.48, n_l=1.0	t_g=510 nm	Λ_g=750 nm, W_g=495 nm, N_g=18
3	Substrate	n_{sub}=1.48	$t_{sub} = \infty$	Infinite half space

Table C.10: Structure dimensions and refractive-indices related to Fig. 4.18.

No.	Layer	Refractive index	Thickness	Comment
1	Superstrate	n_{sup}=1	$t_{sup} = \infty$	Infinite half space
2, 3	DBR-h DBR-l	n_h=3.48 n_l=1.48	t_h=111.4 nm t_l=261.8 nm	6 pairs DBR
4	Active	n_c=3.1661	t_c=734.3 nm	III-V active region
5	Cavity	n_c=1.48	t_c=465.6 nm	Nominal cavity
6	Grating	n_h=3.48, n_l=1.0	t_g=430 nm	Left barrier: Λ_g=750 nm, W_g=470.3-495 nm, N_g=14 Well: Λ_g=750 nm, W_g=495 nm, N_g=16
7	Substrate	n_{sub}=1.48	$t_{sub} = \infty$	Infinite half space

Table C.11: Structure dimensions and refractive-indices related to Fig. 4.19.

C.2.7 Figure 4.18

Table C.10 is related to Fig. 4.18. The simulated structure is a 2D HCG illuminated by a TM-polarized Gaussian beam with beam waist of 7 μm at 1550 nm wavelength. There is no in-plane heterostructure for the grating layer and it is simply terminated by a silicon waveguide. For Fig. 4.18(a) the beam center is at x=0, while for Fig. 4.18(b) the beam is moved 1.5 μm toward right and its center is at x=1.5 μm.

C.2.8 Figure 4.19

Table C.11 is related to Fig. 4.19. The simulated structure is a 2D HCG-based vertical cavity with 0.5λ-long SiO_2 cavity. The HCG is designed to be highly reflective for a TM-polarized light at 1550 nm wavelength. An in-plane heterostructure is formed at the left side by changing the grating bar width gradually from 470.3 to 495 nm while keeping the grating period constant.

C.2.9 Figure 4.20

Table C.12 is related to Fig. 4.20. In HCG-based vertical cavity structure, an additional active layer made of InP is introduced below the DBR structure in order to add gain or loss to the cavities. The total InP thickness is $t_a = \lambda_d/2n_a$ and it is assumed to have a core region where the gain or loss is introduced and two passive cladding layers. The core region is placed at the maximum of the field profile to be more effective which is approximately in the middle of the InP layer. In the case of Fig. 4.20(c), there is no gain or loss in the structure, i.e. $n_{g,l}$=0. Furthermore, W_c is varied to change coupling strength between two cavities through the distance between them. In the case of Fig. 4.20(d), the distance between two cavities is kept constant at W_c=1.28 μm (so do their coupling strength), and an equal gain and loss $n_{g,l}$ is introduced in each cavity.

No.	Layer	Refractive index	Thickness	Comment
1	Superstrate	n_{sup}=1	$t_{sup} = \infty$	Infinite half space
2, 3	DBR-h DBR-l	n_h=3.48 n_l=1.48	t_h=111.4 nm t_l=261.8 nm	6 pairs DBR
4	Cladding-t Gain-Loss Cladding-b	n_{cl}=3.166 n_a=3.166 $\pm i n_{g,l}$ n_{cl}=3.166	t_{cl}=97.4 nm t_a=50 nm t_{cl}=97.4 nm	Left cavity with gain (+ sign), right cavity with loss (– sign)
5	Cavity	n_c=1.0	t_c=725.1 nm	Nominal cavity
6	Grating	n_h=3.48, n_l=3.48	t_g=430 nm	Barriers: Λ_g=640 nm, W_g=363.8 nm, N_g=8 for Left/Right, $N_g = W_c/L_g$ for Middle Wells: Λ_g=640 nm, W_g=371.2 nm, N_g=8
7	Substrate	n_{sub}=1.48	$t_{sub} = \infty$	Infinite half space

Table C.12: Structure dimensions and refractive-indices related to Fig. 4.20. For Fig. 4.20(c), $n_{g,l}$=0, while the W_c is changed. However, in the case of Fig. 4.20(d), W_c is kept constant at 1.28 μm and $n_{g,l}$ is varied in both cavities.